Microfabricated Fluorescence-Activated Cell Sorters (μFACS) for Screening Bacterial Cells

Thesis by

Anne Yen-Chen Fu

In Partial Fulfillment of the Requirements

for the Degree of

Doctor of Philosophy

California Institute of Technology

Pasadena, California

2002

(Submitted May 13, 2002)

Acknowledgements

Through the course of my study at Caltech, I have gained much more than what I had originally anticipated. In and out of laboratory settings, many things have taken on a deeper meaning. Friendship, collaboration, team work, persistence, maturity, and appreciation of others' expertise are all parts of daily routine. During these days, there were especially a few people who made their marks in the progress and accomplishment of this thesis.

Firstly, I thank and worship God who is always in my spirit to carry me through my toughest times with the bountiful supply of the Spirit of Jesus Christ. He's the real living Savior in all the situations.

My two advisors, Dr. Stephen R. Quake and Dr. Frances H. Arnold, have taught me the necessary skills to carry out independent research projects. Over the years, Steve taught me many things I didn't know before, such as computer programming, optics, electronics, and of course, the chemistry of my favorite material, PDMS. Frances conveyed to me the ideas of evolution in the laboratories and the use of high throughput screening. I truly appreciate their patient training and forbearance to allow me to make mistakes and learn. It's an honor and a privilege to embrace the knowledge of two top professionals in different fields into my own.

I also thank many of my colleagues, especially, Hou-pu Chou and Charles Spence. Hou-pu tried to teach me everything he knows about microfabrication and PDMS devices. Words just cannot describe my appreciation for his friendship, time and assistance. Charles initiated me into the world of building fancy electronic boxes and machining interesting gadgets. Marc Unger inspired me to do interesting chemistry on PDMS and also enlightened me on the theories of microfluidic mechanics. Emil Kartalov has helped me many times in carrying heavy objects, machining and other strenuous tasks. Ali Ghaffari has taught me how to operate many different machines in all the labs and also shared many of his own life experiences with me.

Guillaume Lessard and Jason T. Yang have assisted me countless times on rescuing or reconfiguring my computer. Shuwei Li, Markus Enzelberger, Yohei Yokobayashi, Todd Thorsen, Aramia Asmar and Shuli Eyal have tutored me numerous times on biochemistry, molecular biology, PDMS and data analysis. Connie Rodriguez has assisted me many, many times to deal with purchasing and other administrative matters in a timely fashion. My colleagues at Vanderbilt, Franz Baudenbacher and Luis Fong, have opened up an interesting world of supergreen biomagnetism for me. Last but not the least, W. French Anderson has inspired me to use modern science and technology for the sake of helping mankind.

My two loving sisters, Joannie and Daisy, have really stood by me during my times of confusion and frustration. We had many deep talks about our future, relationships and just had fun. My closest friends, Esther Luckhardt, Nicole Yang, Felicia Chang, Catherine Chen, Joanne S. Lii, Becky Stewart, Elenore Niu, Grace Tahir, Cynthia Shih and Agnes Juang, all have shown me their truest friendship, sincere support and caring concerns during my pursuit of this degree. James and Rebecca Hsiao supplied me with much spiritual help and edified me in many ways. My dog, Oddie, has always accompanied me during my late-night studies and is always very happy to greet me no matter how late I come home from lab.

Best of all, I've met someone who has come to love and appreciate not only my work, but my entire person. As we begin a new chapter in our lives together, I thank Jim for his patience, understanding, thoughtfulness and for being the perfect one for me through these years and the many more years to come.

Most importantly, I dedicate this doctorate degree to my parents, Pat Pi-Hsia and John Yung-Chi Fu. Due to their persistent struggles in this foreign country, I have gained a new and better future. Their unconditional love and constant support throughout my life are immeasurable. I am forever grateful to them.

Abstract

In this thesis, I have developed elastomeric microfabricated cell sorting devices using a micromachining technology, "soft lithography". Inexpensive elastomeric microfabricated devices were designed to replace flow chambers in conventional fluorescence-activatived cell sorters (FACS). Sorting of cells and other particles was accomplished *via* different means of flow control. My early work of cell sorting on these devices was accomplished using electrokinetic flow. However, in order to alleviate problems associated with electrokinetic flow, the microfabricated cell sorter was integrated with microvalves and micropumps for pneumatic actuation control. The integrated cell sorter has better capabilities of fine-tuning the flow control, manipulating single cells and is less harmful to the cells than electrokinetic flow. Substantial enrichments of beads and cells were accomplished on these devices. Novel sorting algorithms, which can only be implemented in microfabricated devices, were also demonstrated. Compared with conventional FACS, these microfabricated devices allow for more sensitive optical detection for bacterial cells and DNA, innovative sorting schemes and are disposable to eliminate any cross-contamination from previous runs. Ultimately, these elastomeric microfluidic flow cells provide an inexpensive, robust and effective way to perform cell sorting and can be used as stand-alone devices or as a part of an integrated system for diagnostics and/or cytometric measurements.

Presently, the microfabricated cell sorter is enjoying new applications in various fields for high throughput screening, including directed evolution, digital genetic circuits, microbiology and cell biology of gene expression and regulation. In addition, this sorter is not limited only to the detection of optical signals. I have attached the sorter to a high resolution magnetometer, a superconducting quantum interference device (SQUID) microscope, to obtain cytometric data of the magnetic field strengths of magnetotactic bacteria as they flowed through the device.

This thesis lays down the foundation for future work in cell sorting and single

cell analysis. Time-course measurements of a single cell for kinetic studies can be implemented using novel sorting schemes. Sample dispensing and any downstream analysis, such as cell lysis and/or polymerase chain reaction, can be carried out immediately after the cells have been sorted. The sorter could also be incorporated with other technologies to measure cellular magnetic or electrical properties. We anticipate that an integrated lab-on-chip, where cell sorting is one of the steps of a complete analysis system, is not far off.

Thesis Advisor: Stephen R. Quake
Title: Associate Professor of Applied Physics

Thesis Advisor: Frances H. Arnold
Title: Dickinson Professor of Chemical Engineering and Biochemistry

Contents

List of Figures

List of Tables

Chapter 1
Introduction

1.1 Objective

Flow cytometry is a technology that is needed for analyzing and sorting cells just as gel electrophoresis is required to characterize, purify or quantify DNA in every biological laboratory. Until recently, flow cytometry has mainly been used to study DNA contents and surface antigens for characterization of eukaryotic cells[1, 2]. Now, this technology is beginning to have a role in modern biomedical research, such as ligand binding and enzyme kinetics, drug screening, DNA sequencing[3] and protein engineering[4, 5, 6]. However, although conventional fluorescence-activated cell sorters (FACS) provide impressively efficient sorting, they are costly, mechanically complex and require trained personnel for operation and maintenance[7]. This greatly limits the use of cell sorting in various biological research. Thus, inexpensive devices that can rapidly sort live cells, particles and even single molecules would enjoy wide applications and accelerate the progress of clinical medicine, basic biological and material research.

The goal of my thesis is to develop an elastomeric microfabricated cell sorter which allows for high sensitivity, no cross-contamination, and lower cost than any conventional FACS. The course of this development depends heavily on two key technologies that have advanced rapidly within the past decade: microfluidics[8, 9, 10] and soft lithography[11, 12]. Sorting in the microfabricated cell sorter is accomplished *via* different means of microfluidic control. This confers several advantages over the conventional sorting of aerosol droplets: 1) novel algorithms of sorting and/or cell manipulation can be accomplished, 2) dispensation of reagents and biochemical reactions can occur immediately before or after the sorting event, 3) completely enclosed

fluidic devices allow for studies of biohazardous/infectious cells or particles in a safer environment and 4) integration of other technologies can be implemented into the cell sorter. In addition, due to the easy fabrication process and inexpensive materials used in soft lithography, this elastomeric microfabricated cell sorter is affordable to every research laboratory and can be disposable just as a gel in gel-electrophoresis, which eliminates any cross-contamination from previous runs. The planar configuration of the microfabricated cell sorter also allows for more sensitive optical detection and easier mechanical setup.

This introduction briefly describes the two underlying principles of flow cytometry and soft lithography that have shaped my thesis work. An outline of my thesis work is also presented.

1.2 Flow Cytometry

Historically, characterization of morphological features in cellular pathology and physiology often involved using light absorbing dyes and fluorescent probes[1, 2]. Classical techniques, such as fluorimetry, microscopy and absorbance, yield only qualitative data of cells being examined but are unable to quantitate objectively at the single cell level. Moreover, later developments in cell biology require precise quantitation of specific dye molecules or probes for identifying different cell types. Hence, there was a need for methods that can rapidly produce sensitive and quantitative measurements on a single cell level. Since then, for the past seventy years, cell sorting has become an art for a group of scientists who called themselves "flow-ers" in reference to the technology, flow cytometry.

The word "cytometry" refers to the measurement of physical or chemical characteristics of cells or biological particles. The physical and/or chemical characteristics measured, mainly fluorescence and light scatter, can be intrinsic (light scatter and electrical conductivity) or extrinsic (DNA/RNA contents, protein content, and probes)[2]. Flow cytometry thus refers to the process of measuring and analyzing these characteristics as cells or particles pass through a beam of light, one at a time,

in a jet stream[13].

The basic components of a flow cytometer can be divided into several parts: light sources, optical systems, flow chambers and sorting devices, photodetectors and electronics (See Figure 1.1). Light sources are used to illuminate the cell or particle samples. Optical systems direct the light path for illumination and collection of light scattered or emitted by the sample. Flow chambers maintain a stream of cells in a single file at a constant flow velocity to pass through the interrogation point where the excitation beam and the stream intersect. Sorting devices break up the jet of cells into charged droplets and deflect their pathway through a pair of high voltage plates. Photodetectors are placed at angular positions relative to the beam axis to detect emitted/scattered photons. Electronics then will capture and process the signals collected by photodetectors. In a sample run, as each cell passes through the point of interrogation, photodetectors collect its fluorescence and light scattering through optics. These photodetectors convert light signals into electrical signals and the computer analyzes and stores the data. Presently, many of the flow cytometers have an additional feature of using electrical and/or mechanical means to sort and collect cells into desired test tubes or locations on agar plates. Each component must be carefully chosen to have the best results for different specific applications.

In order to achieve high uniformity in illumination and detection, the flow chambers of modern flow cytometers are designed to have a nozzle and are based on the principle of hydrodynamic focusing[14]. When the sample-carrying medium exits the nozzle, a central flow stream of tens of microns in diameter is obtained by means of the sheath pulling from the surrounding buffer flowing at a higher speed. If sorting is desired, an ink-jet head is built in and charged droplets are formed and shoot out when biased under a high voltage. Electrostatic deflection is then used to achieve high sorting rates[15, 16]. However, this mechanism is delicate and many failures of the instrument can result from problems in the flow chamber. For example, clogging of the orifice and particle adsorption and contamination in the tubing can cause turbulent flow in the central jet stream, inducing variation in illumination and detection. Sample carryover can occur during consecutive runs when remnants of previous sam-

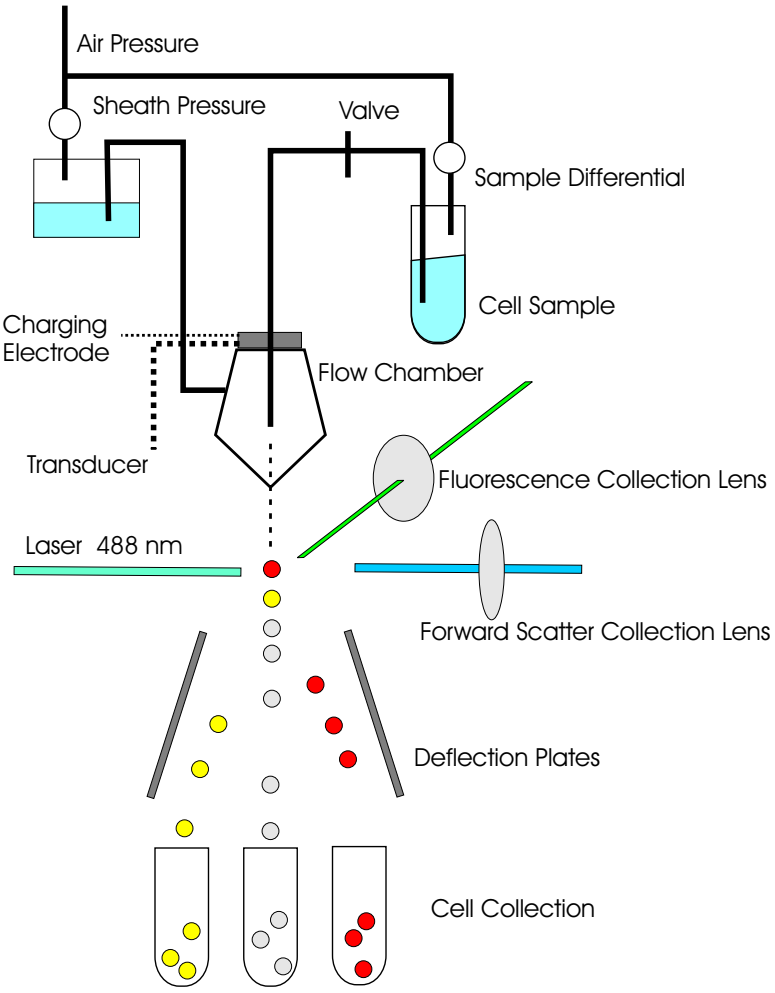

Figure 1.1: A schematic of a modern conventional FACS.

ples backflush into the new sample stream, and sterilizing the system between runs is time-consuming and results in machine downtime. Furthermore, cells or particles passing the orifice of the ink-jet head may perturb droplet formation: larger objects can change the droplet size, nonspherical cells tend to align with the long axis parallel to the flow axis, and deformable cells may elongate in the direction of the flow[2]. Such perturbation in droplet formation can introduce variation in the time from the analysis to the actual sorting event. Finally, a number of technical problems make it difficult to generate identically charged droplets, in turn increasing the deflection error.

Thus beginning in the 1990's, several micromachining methods[17, 18, 8, 19] have been sought to replace the conventional flow chambers in FACS with microfluidic

devices that can potentially provide more accurate sorting and flexible design.

1.3 Soft Lithography

As new artists in the field of flow cytometry, my colleagues and I have incorporated a novel micromachining technology, soft lithography, into the art of cell sorting. Soft lithography is a newly developed technique which uses the process of rapid prototyping and replica molding to fabricate inexpensive elastomeric microfluidic devices[11]. In other words, soft lithography offers a way to substitute conventional silicon microfluidic devices with other materials, such as plastics and polymers. The elastomeric properties of plastics and polymers allow for an easy fabrication process and cleaning for reuse or disposal. A variety of biological assays can also be carried out due to chemical compatibilities of different plastic materials with different solvents. Moreover, fabrication of multilayer devices using soft lithography allows for simple integration of different functions on a chip in spatial arrangements instead of an one-dimensional large-sized chip. Several techniques are currently being developed using soft lithography, such as patterning of biomaterials[19] and nonbiomaterials, cell-based biosensors, optical detectors, reverse micelle formation[20] and oligonucleotide synthesis.

Using soft lithography, many inexpensive, flexible and microfabricated devices can be designed to replace flow chambers in conventional flow cytometers. More accurate sorting of cells can be accomplished since the sorting region is at or immediately after the interrogation point. On-chip chemical processing of cells has been accomplished and can be observed at any spot on the chip as the interrogation point. This method can eliminate any dead time that occurs in the conventional flow cytometric kinetic studies and achieve a much better time resolution. Furthermore, linear arrays of channels on a single chip, the multiplex system, may be simultaneously detected by an array of photomultiplier tubes (PMT) for multiple analysis of different channels. Multiplexing in these microsystems increases the throughput rate and allows for sychronous measurements that cannot be done using a conventional FACS (although linear flow velocities of these chips may not attain the high linear

flow velocity of a conventional FACS, 10 m/sec). Furthermore, other sophisticated biological assays can also be implemented on-chip due to the simplicity and flexibility of sample handling and massive parallelization, such as cell lysis[21], polymerase chain reaction (PCR)[22], optical tweezer/cell trapping[23], and even transformation of cells by electroporation[24] or optoporation[25]. In terms of optical light collection efficiency, these microchips allow for a minimal volume of cell suspension, approximately 100 femtoliters, at the interrogation point. The minimal volume of optical interrogation greatly reduces the amount of background light scatter from the suspending medium and sheath flow, and from the materials of the flow chamber. Due to the planar configuration of these microchannels, higher numerical aperture (N.A.) oil immersion objectives can be used to collect more fluorescence instead of the conventional N.A. = 0.6 dry lens used in both fluidic and aerosol flow chambers. One additional feature for these soft-lithographed microchips is that most of them are disposable due to their inexpensive material. These properties relieved many of the concerns for sterilizing and permanent adsorption of particles unto the flow chambers.

In this thesis research, I have constructed microfabricated cell sorting devices using soft lithography. Sorting of cells and other particles on these microfluidic devices was accomplished through different means of flow control. My earlier work of cell sorting was concentrated on using electrokinetic flow[26]. Later work primarily focused on the design and fabrication of a monolithic microfluidic cell sorter integrated with microvalves and micropumps[27]. Each means of flow control has its own advantages and disadvantages. But ultimately, these new devices serve as an alternate route towards the development of a robust, inexpensive and non-biohazardous flow cytometer.

The microfabricated cell sorter is presently enjoying a wide variety of applications. I have demonstrated the ability of the microfabricated cell sorter to perform high throughput screening in the field of directed evolution using green fluorescent protein variants expressed in *E. coli* cells. I have also integrated the cell sorter onto a superconducting quantum interference device (SQUID) microscope for the detection of magnetotactic bacteria. Furthermore, the sorter is now being used to characterize

the static behaviors and stochastic noise of digital genetic circuits expressed in *E. coli* cells[28]. Working with an interdisciplinary group of experts from various fields in Dr. Quake and Dr. Arnold's labs, my progress in developing a microfluidic cell sorter and its applications is outlined below.

1.4 Outline of Thesis

Each chapter of this thesis describes a different project that I have been working on relating to the microfluidic cell sorter. Chapters 2 and 3 present detailed accounts on the developments of the cell sorter using both electrokinetic flow and integrated microvalves and micropumps. The remaining chapters discuss the applications of the microfabricated cell sorters in various fields. Chapter 4 presents the cell sorter as an inexpensive, robust, powerful and effective tool to perform high throughput screening in the field of directed evolution. Chapter 5 describes the analysis and characterization of a digital genetic inverter in the field of DNA and cellular computation. Chapter 6 discusses the possibility in sorting cells according to their magnetic properties using a microfluidic cell sorter and a magnetometer in the field of biomagnetism.

1.4.1 An Elastomeric Microfabricated Electrokinetic Sorter

I have constructed the first generation of a microfabricated fluorescence-activated cell sorting (μFACS) elastomeric device and demonstrated its effectiveness for sorting micron-sized latex beads and bacterial cells *via* electrokinetic flow. For the past two decades, rapid development of micromaching has led to the beginning of a new era in technology, Bio-MEMS. Using microfluidic networks, analysis of biomaterials can be done in a faster time scale with less sample and reagents required. Other groups have demonstrated that cells, particles and reagents can be manipulated in microfluidic devices by pressure, dielectrophoresis and electroosmosis. I have been able to sort and recover viable cells after they have passed through the device. Innovative sorting schemes were also implemented onto the chip which open up new avenues for studying cells which cannot be accomplished on a conventional flow cytometer.

1.4.2 A Microfabricated Cell Sorter Integrated with Microvalves and Micropumps

The second generation of the microfabricated sorter was integrated with microvalves and micropumps for pressure-driven sorting schemes. Fabricating by multilayer soft lithography, the cell sorter was incorporated with various microfluidic functionalities, such as on-off valves, switching valves, dampers for fluidic perturbations and peristaltic pumps on chip. This new sorter has better capabilities for fine-tuning the flow, trapping cells, and controlling the dispensing of samples. It also allows sorting to be done in almost any aqueous suspending medium, unlike its predecessor. This improved sorter presents a gentler method of sorting cells, which increases the recovery and viability of sorted cells.

1.4.3 High Throughput Screening of GFP Variants Using μFACS

The success of directed evolution to explore protein space and create new proteins depends on two factors: 1) the ability to generate genetic diversity and 2) the ability to rapidly screen for the desired mutants. Unlike the conventional technology of screening in microtiter plates, μFACS serves as an inexpensive, robust and powerful tool to perform high throughput screening. As an example, variants of green fluorescent protein were expressed in *E. coli* and flowed through μFACS to screen for mutants with red-shifted emission maxima. Results of our sorting are presented in this chapter and the performance of μFACS as a high throughput screening tool for directed evolution are also discussed.

1.4.4 Digital Genetic Circuits

Using simple bacterial genetic elements, such as promoters, repressors and operator regions, networks of *de novo* genetic circuits can be designed to implement the digital logic abstraction and thus are able to perform computational functions *in vivo*. In this

chapter, I describe the analysis and characterization of a simple genetic inverter using μFACS. The variations due to stochastic gene expression and systematic fluctuations, and how these are related to the static behavior of the inverter are also discussed.

1.4.5 Flow Cytometry of Magnetotactic Bacteria Using a Microfluidic Cell Sorter and a SQUID Microscope

Many future potential applications of μFACS lie in its unique capability of integration into other technologies. Working together with the Living State Physics group at Vanderbilt University, I have attached the μFACS onto a superconducting quantum interference device (SQUID) microscope. Both natural and cultured magnetotactic bacteria were flowed through the sorter to be characterized by the SQUID microscope. Experimental procedures and data are presented in this chapter.

Chapter 2

A Microfabricated Electrokinetic Cell Sorter

Within the past decade, high throughput analysis has become an indispensable part of genetic and biotechnology research. In genetic research, studies of genomics and proteomics use large-scale global cDNA hybridizations and/or protein bindings to understand total cellular gene expression[29, 30, 31]. Moreover, the human genome and other genome sequences are being deciphered rapidly to study these networks of gene expression[32, 33]. In biotechnology, protein engineering, namely directed evolution, generates genetic diversity by creating a huge library of random mutants in search for new enzymes and evolutionary pathways[34, 35]. These studies of gene expression and gene evolution often need to analyze up to 10^4–10^6 different species in order to acquire substantial information concerning the genetic pathways. Thus new and improved high throughput screening technologies have to be implemented in parallel. Conventional FACS, laser scanning image analysis and silicon microfluidics were all developed to perform high throughput data acquisition in these studies.

The oldest technology, flow cytometry, analyzes cells in a single profile as they pass through a point of detection in a jet stream. Sorting occurs after the point of detection where the cells are deflected into desired locations in test tubes or microtiter plates. Although conventional FACS machines have demonstrated impressive performance in detection and sorting of cells, however, as mentioned in Chapter 1, they are costly, mechanically complex, and require trained personnel for operation and maintenance. They also have major problems of low sensitivity for bacterial cells and DNA, cross-contamination between runs and are mechanically inflexible to work with different cell types and sizes. Hence, to this date, most work in flow cytometry is primarily

focused on mammalian cells.

High throughput image analyses of DNA[29, 30, 31], protein[36, 37, 38] and cell microarrays[39, 40] using laser scanning fluorescence microscopy or an ultra-sensitive CCD camera allow up to 10^6 samples to be detected in a short period of time. Multiple images can be traced at different times to follow the sequence of an event. Micropipettes or laser tweezers can be used to manipulate a single cell or molecule for further analysis or recovery. Yet, recovery of a population of cells or particles from the arrays is difficult. If further analysis needs to be done, the identities of the individual spots on the arrays must be known *a priori*.

Many silicon microfluidic devices were also developed to perform high throughput analysis. Electrokinetic forces can be used within microchannels to separate ionic species, such as DNAs and peptides[9, 41]. These DNAs and peptides are stained with fluorescent dyes either before or after separation and are identified as they pass through the detection region. Multiplexing these capillaries allows arrays of samples to be analyzed simultaneously and increases the throughput rate. Large-scale DNA or protein sequencing can be done in this way. This kind of passive separation, however, depends on the inherent differences in the electrophoretic mobility of samples being interrogated. More recently, separation of cells through a microfabricated lattice[42] or dielectrophoresis[23, 43, 44] was also done using the differences in their inherent morphology and anatomy. Detection of these species occurs only after separation.

Microfabricated silicon devices also created valveless switches as pressure-switching[45] and dielectrophoresis[46] to perform active sorting. Active sorting of cells and particles involves first detection and then separation. A predetermined set of properties determines the fate of the cells upon detection instead of their inherent properties. Yet the delicate and tedious fabrication process along with the complicated electronic and buffer requirements in dielectrophoresis have inhibited the silicon microfluidic technologies from gaining popularity among biochemists and biologists.

My colleagues and I have exploited soft lithography in our first endeavor to develop a microfabricated fluorescence-activated cell sorter (μFACS) for high throughput screening of bacterial cells. Active sorting occurs *via* electrokinetic flow when the

fluorescence of the cell passes a preset threshold. Sorted cells can be recovered at the output wells of the sorter, thus the identities of the cells do not have to be known *a priori*. Soft lithography offers an easy way to fabricate inexpensive elastomeric microfluidic devices with plastics and polymers instead of silicon. Unlike conventional FACS, this μFACS is easy to operate, highly sensitive for bacteria and DNA, and can be disposable. The flexibility in the design of the flow cell also allows different cell types and sizes to be analyzed. This μFACS is intended to be used in high throughput screening of directed evolution and other biological applications.

This chapter presents my progress in developing μFACS in three sections. Section 2.1 describes the cell sorter and its optical and electronic setups. Section 2.2 details a report of various trials of surface treatments and buffers. Section 2.3 presents the results of characterization and cell sorting on μFACS.

2.1 Fabrication and Design

2.1.1 Cell Sorter from Soft Lithography

Adopting from previous work in DNA sizing in our group[17], Charles Spence and I have constructed a microfluidic flow cell, an optical detection system and electronics to perform cell sorting. The microfabricated flow cell is a silicone elastomer chip with three channels joined at a T-shaped junction (See Figure 2.1). The dimensions of the channels are 100 μm wide at the wells and narrowing down to about 5–10 μm at the T-junction. Channel depth is 4 μm. The channels are sealed with a glass coverslip. A buffer solution is introduced at the input channel and fills the device by capillary action. The pressure is equalized by adding buffer to the two output ports and then adding a sample containing the cells to the input port. The fluid within the channels is manipulated *via* electrokinetic flow, which is controlled by three platinum electrodes at the input and output wells.

This disposable, soft-lithographed microfluidic chip is a silicone elastomer impression of an etched silicon wafer. The etched silicon wafer is fabricated as follows[47].

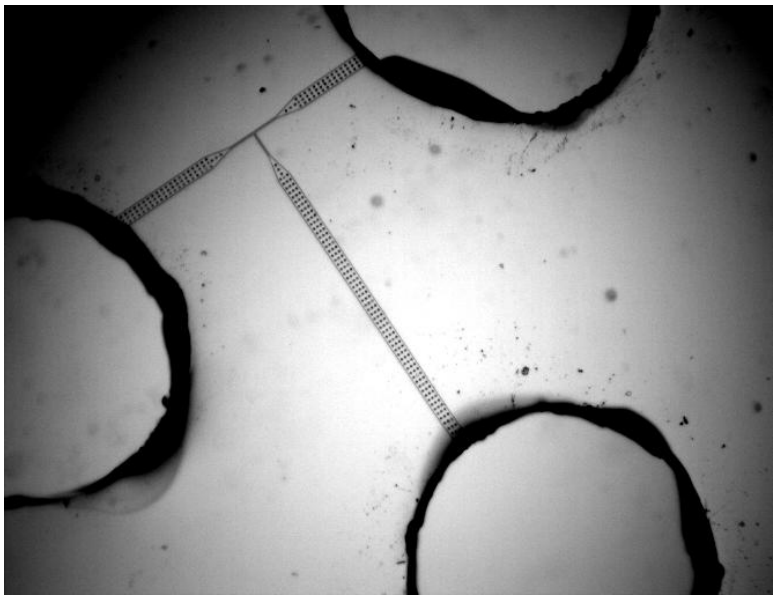

Figure 2.1: Optical micrograph of the μFACS device.

A $< 100 >$ lightly doped silicon wafer with an oxide layer of 200–300 nm thickness was used. After using standard contact photolithography techniques to pattern the photoresist (Shipley SJR 1813) onto the silicon wafer, a mixture of C_2F_6 and CHF_3 gases is used to etch the wafer by reactive ion etch (RIE). RIE etches away the photoresist and the oxide layer, exposing the silicon layer underneath. A wet etch using KOH anisotropically etches deeper into the silicon layer. The final product is an etched silicon wafer that becomes a mold for the silicone microfluidic chip, as shown in Figure 2.2. Using the principle of replica molding, the silicone elastomeric chip is made by pouring a mixture of a two-component curing system of a silicone polymer, polydimethylsiloxane (PDMS), with its curing agent onto the mold. In this case, I use General Electric RTV 615 A (silicone polymer) and B (curing agents) components in a typical ratio of 10:1. The chemistry of the silicone rubber is described in Chapter 3. After curing in the oven at 80° C, the elastomeric chip is peeled off from the mold and is sealed with a glass coverslip. The whole cell sorting device is mounted on an inverted microscope with optical detection and electronics schemes as described below.

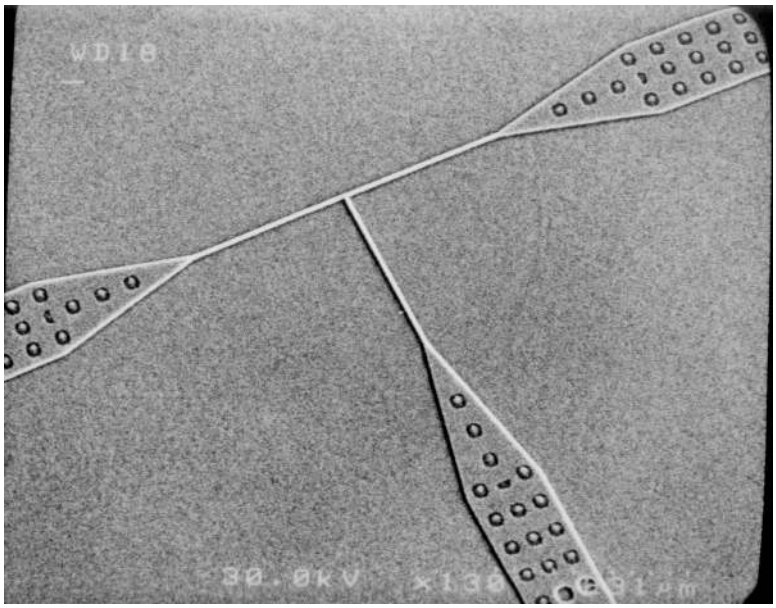

Figure 2.2: A SEM image of an etched silicon mold.

2.1.2 Optical Detection and Electronics Design

The cell sorting device is mounted on an inverted microscope (Zeiss Axiovert 35) with an oil immersion objective (Olympus Plan Apo 60X, 1.4 NA), as shown in Figure 2.3. Epi-fluorescent excitation was provided by an Argon ion laser (Coherent Innova 70) for cells and a 100 W mercury lamp for beads. Fluorescence was collected with the same objective and projected onto the cathode of a Hamamatsu H957-08 photomultiplier tube with custom current-to-voltage amplifier. Part of the light can be directed onto a CCD camera for imaging. The detection region is 5–10 μm below the T-junction and has a window of 15 x 5 μm dimension. The window is implemented with a Zeiss adjustable slit. Cells or particles can be directed to either side of the "T" channels depending upon the voltage potential settings. The voltages on the electrodes are provided by a pair of Apex PA42 HV op amps powered by Acopian power supplies. The third electrode is ground. The PMT signal is digitized by the PC, which also controls the high voltage settings via a National Instruments Lab PC1200 card. The details of the optical and electrical setup will be elaborated in the next two sections. It is straightforward to extend the system to include multiple color fluorescence and light scattering detection, as in conventional FACS machines.

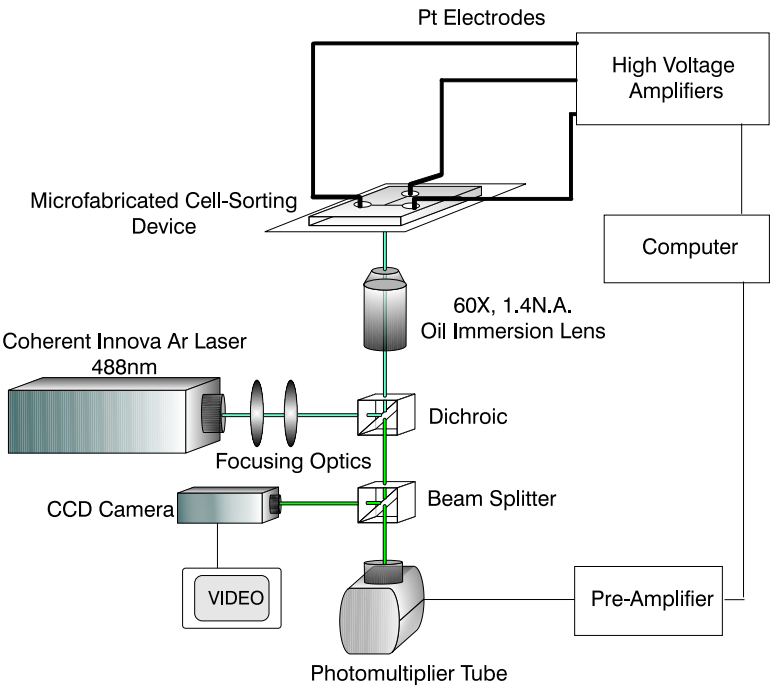

Figure 2.3: A schematic of the setup for μFACS.

Optical Setup

A schematic of the optical setup for excitation and detection of the microfabricated cell sorter is as follows. The laser beam was collimated to achieve uniform illumination of the samples. A 5 W Argon laser (Coherent Innova 70) was used as an excitation source. For cell sorting, the plasma tube current was set between 10–25 amps with an output power of 100–500 milliwatts at 488 nm. A half waveplate is placed in front of the laser to rotate the polarization of the beam at an angle of 20–60°. This beam is then split by a polarizing cube beam splitter into its p-plane and s-plane polarized components. By adjusting the angle of the half waveplate, the angle of polarization of the laser beam with respect to the optical axis will differ and thus varying the difference in the intensity of its p-plane and s-plane components. The p-polarized beam, about half the output of the laser, is expanded and collimated by a homemade "telescope". This beam expander is composed of two lenses in which the first lens has a focal length of 12 mm and the second lens has a focal length of 85 mm. The expanded beam is then directed by a pair of 2-inch steering mirrors into the back of an

inverted microscope (Zeiss Axiovert 35). Within the Zeiss microscope, the collimated beam is focused by a pair of lens into the back focal plane of the objective (Olympus Plan Apo 60X, 1.4 NA, oil immersion). The objective again collimates the beam to achieve uniform illumination of the sample.

The fluorescence detection scheme also utilizes the principle of collimating the emitted light. The fluorescence is collected by the objective at infinity focus. The image of the sample is then focused onto an adjustable slit at the sideport of the microscope. This adjustable slit controls the field of detection and the amount of light entering into the PMT. The fluorescence reaches to infinity focus again by a lens with a focal length of 75 mm. A 20/80 beamsplitter images 20% of the collected light into the CCD camera for observation and the rest is directed onto the PMTs. For just beads and cells sorting, only one PMT is used to observe the pulse height of each signal from the particles. For signal processing in Chapter 4, a pair of PMTs were actually used to compare ratios of pulse heights from two different wavelengths.

Electronics

A side-on photomultiplier tube (H957-08; Hamamatsu, Bridgewater, NJ) was used as the detector for cell sorting. A transimpedence amplifier (OPA128; Burr-Brown, Tucson, AZ) converts the photocurrent to voltage at a gain of 10^7 V/A. A 15 V DC power supply was built for both the detector and the current-to-voltage preamplifier. The signal was then filtered by an RC low-pass analog filter at 1.6 kHz and then digitized by a NI-Daq card (LAB-PC-1200; National Instruments, Austin, TX) on a personal computer. Running a sorting algorithm in C, the signals were analyzed and appropriate voltages were set on the PC1200 board analog outputs (+5 V to -5 V). These voltages were then amplified by a pair of APEX PA42 (30 V/V) to two platinum electrodes that were inserted one each into the collection and waste wells. The third electrode was ground at the input well. These voltages were set to manipulate the direction of the fluid flow inside the channels.

2.2 Principle of Electrokinetic Flow

When a potential difference is applied across a microfluidic channel, an electro-osmotic flow is induced. Beads, cells or other particles in the electrolytic solutions are being carried along with electro-osmotic flow. Manipulation of these particles can be accomplished by adjusting the potential difference between two platinum electrodes inserted at the ends of the microchannels. The switching of fluid flow at the T-junction of μFACS is almost as instantaneous as the switching of the potentials. Electro-osmotic flow is thus a good and easy way to manipulate particles and create valveless switches within any microfluidic device.

According to [48], electrokinetic phenomena arise from forces occurred at mobile electrified interfaces. For example, a potential difference is applied across a glass capillary filled with electrolytic solution. Instead of current flowing through the capillary, the electrolytic solution begins to move within the capillary, resulting in electro-osmotic flow. This simply means that a potential difference has the same effect as a pressure difference within the capillary. Thus the flow velocity, V, of electrolytes within a capillary depends on two components, a pressure gradient, ΔP, and an electric field, X.

$$V = a_1 \Delta P + a_2 X \tag{2.1}$$

So if there is no pressure gradient $\Delta P = 0$, there is still flow, $V = a_2 X$, resulting from the electric field, where a_2 is the electrophoretic mobility.

Vice versa, one can predict that a current, i, can also result from an electric field and a pressure difference within the capillary.

$$i = a_3 \Delta P + a_4 X \tag{2.2}$$

So in the absence of an electric field, $X = 0$, a streaming current occurs from the pressure gradient,

$$i = a_3 \Delta P \tag{2.3}$$

where a_3 = streaming current density. If Equation 2.3 is divided by the specific conductivity of the electrolytic solution, σ, then

$$\frac{i}{\sigma} = \frac{a_3 \Delta P}{\sigma} = X_i \tag{2.4}$$

where X_i is the electric field of the streaming potential resulting from the application of a pressure difference. Thus, as Equation 2.5 shows, one can predict that the flow velocity of fluid due to an applied electric field within the capillary is the same as the current resulting from a pressure difference.

$$\left(\frac{i}{\Delta P}\right)_{x=0} = a_3 = a_2 = \left(\frac{V}{X}\right)_{p=0} \tag{2.5}$$

From an atomistic view on electrokinetic phenomena, the electrolytic solution consists of many diffuse layers acting as planar electrodes. Each layer is a few angstroms thick and is at a distance, χ, from the wall of the capillary. If a potential difference is applied across the capillary, a layer of charge, q, at a distance χ from the wall of the capillary will experience an electric force qX, where X is the electric field. This force will cause the layer to move across the capillary. Yet, this motion will be opposed by the viscous force. Thus when the electrolytic solution reaches to a steady velocity, the electric force is exactly equal to the viscous force. The same phenomenon will occur if a pressure gradient occurs within the capillary.

In addition to electrokinetic phenomena, another motion occurs within the electrified capillary, called ion migration. Instead of seeing the electrolytic solution as layers of diffuse charges, individual ions within the solution will move in a specific way in the presence of an electric field. In the absence of any field, ions perform a random walk with equal probabilities in all directions. This is known as diffusion. Yet, in the presence of an electric field, these ions will migrate towards either the positive or negative electrode according to their individual charge. In the course of migrating toward the electrodes, these ions will experience collisions with other ions, shielding effects and viscous forces from the medium depending on their distances from the electrodes. Thus the migration is discontinuous in speed and directions. As these

ions move towards the electrodes, electrolysis occurs. Redox reactions inevitably will also occur at the interface of electrodes and electrolytic solutions. As a result, ions are being depleted constantly and thus the electro-osmotic mobility of the solution changes over time[48]

In a more complex system, such as the microfabricated cell sorter, all these electrokinetic phenomena occur simultaneously and interact with each other. Many experiments were carried out to search for the best conditions for sorting beads and cells. Erratic behaviors and clogging of the beads and cells were often observed due to ion depletion and other unfavorable conditions. Surface treatments of the elastomeric chip and glass coverslips to produce hydrophilicity are described in detail in the next section. Different buffer conditions for beads and cells and the fabrication of microelectrodes are also described.

2.2.1 Surface Chemistry

In microfabricated chips, where the dimensions of microchannels are comparable to the size of the particles flowing within them, surface chemistry becomes very important. Cells and proteins can nonspecifically adsorb onto any hydrophobic or hydrophilic surface, which may result in clogs or reduce throughput rates. Electrokinetic phenomena are highly dependent on the ionic strength of the fluid and the surface charge of the capillary. PDMS is inherently hydrophobic, consisting of a Si-O backbone with methyl and vinyl substituents. Its hydrophobicity prevents aqueous solutions, cells and other bioparticles from flowing smoothly inside these microchannels. Clogging of channels due to adsorption of cells was often observed. Thus several methods were developed to render the surfaces of the elastomeric chip and the glass coverslips more hydrophilic.

Working with Hou-pu Chou, three effective methods were developed to make the elastomeric devices more hydrophilic[47]. Coating the surface with polyurethane (Hydrogel RL#153-87, Tyndale; 3% w/v in 95% ethanol and diluted 10X in ethanol) and curing at 90° C for 60 minutes deposits a hydrophilic layer on the surface of

the microchannels. Yet, such a coating would seal up channels with depths of 2–3 μm. In addition, the polyurethane coating deteriorates after each use, reducing the channels' hydrophilicity and giving inconsisent flow results. A different method exploits the addition of a surfactant, MAKON 6 (Stephan Canada, Longford Mills, Canada; 0.2% v/v) into the mixture of General Electric RTV 615 components followed by curing in an oven as before. MAKON 6 effectively renders the surface of the elastomer hydrophilic, but unexpectedly, it also increases the background fluorescence of the device. Consequently, the third method is to chemically modify the surface of the elastomer by an acid treatment. Immersing the chip in dilute HCl (pH 2.7, 0.0074% in water) for 40 minutes at 60° C will break up the Si-O backbone of the elastomer, modifying the surface to become hydrophilic, consisting of Si-H and Si-OH substituents. This HCl treatment avoids clogging caused by excessive coating, has negligible fluorescence background and does not deteriorate with use. Hence it is the most effective method so far to hydrophilically treat the elastomeric surfaces.

In order to increase the hydrophilicity of the whole cell sorting device, methods were also sought to lessen the adsorption of beads/cells onto the glass coverslip. Coating the coverslips with various chemicals and treatments had not proven to be successful. Rainex, Bovine Serum Albumin (BSA), and successive multiple ionic polymer layer (SMIL)[49] did not reduce the amount of adsorption of particles onto glass and SMIL even caused cell death. However, cleaning dusts and etching metallic and organic residues off the glass coverslips renders the surface more hydrophilic by exposing its polar silanol surface. Two wash formulas seem to work best: a base wash called RCA and an acid wash for glass surfaces, called Chromerge. RCA treatment is a base wash which consists of 6 parts H_2O, 4 parts NH_4OH, 1 part H_2O_2. Glass coverslips were immersed in a stirred RCA solution at 60° C for 1 hour. Then the coverslips were rinsed and stored in high-purity water for later use. Chromerge (Manostat Corporation, New York, NY) is a chromic acid solution derived from chromium trioxide. Coverslips were immersed in a stirred Chromerge solution for one hour without any heat. Cell adsorption was minimized the most when Chromerge-washed coverslips were used, although hydrophilicity of both RCA-washed and chromerge-washed cov-

erslips were very comparable.

2.2.2 Buffers and Microelectrodes

A good buffer system is critical for the success of electro-osmotic sorting within the chip. There were two major problems encountered in the search for an ideal buffering system. One was ion depletion and the second was adsorption of cells and beads onto surfaces of glass and PDMS. Ion depletion results from migration of ions to the electrodes, exhausting the amount of ions remaining inside the solution. Erratic movements of beads and cells within the channels were often observed within 30 minutes in the presence of an electric field. Thus, two criteria were used to select the best buffer system: 1) the buffer has to have a run time up to two hours without experiencing heavy ion depletion, and 2) this buffer also minimizes the amount of cell adsorption and maximizes the viability of the cells within an electric field. Various buffers of different ionic strengths such as phosphate buffered saline (PBS), piperazine-N',N'-bis(2-ethane-sulfonic acid) (PIPES), N-2-hydroxyethylpiperazine-N'-2-ethane sulfonic acid (HEPES) and distilled water were examined. Each buffer was also tested with different salts of various concentrations ($CaCl_2$, $MgCl_2$, NaCl and KCl). In dealing with adsorption, neutral surfactants, such as Triton X-100, Tween 20, MAKON 6, positively charged surfactant, cetyltrimethyl ammonium bromide, and negatively charged surfactants, bovine serum albumin (BSA) and sodium dodecyl sulfate (SDS), were investigated at various concentrations in the buffers to alleviate adsorption. Two buffer systems were discovered which were optimal for these two conditions, one for the carboxylate-modified (CML) beads and the other for *E. coli* cells. For beads, extra reservior wells have to be incorporated in addition to the input and the collection wells in order to prevent ion depletion. Although these two buffer systems may not be the absolute best systems for sorting these particles, they are sufficient for carrying out the experiments within a few hours of run time.

I have also tried to microfabricate electrode pads onto the surface of glass coverslips to prevent electrolysis at the electrode/buffer interface. Metals, such as Au,

Ni, Au/Ni, and Pt/Ni, were all evaporated on the surface of the coverslip in a specific pattern using photolithography. Two microelectrodes, placed at either side of the T-junction, were about 200–400 μm apart and about 50–100 nm thick. The cell sorting device was adhered to the surface of the coverslip containing microelectrodes. Yet, at an electric field of 6 V/cm, electrolysis (detected as bubbles from the microelectrodes) and metal plating occurred within the channels. In addition, except for Pt/Ni electrodes, all of the other metals did not adhere well to glass. They can be easily peeled off as the chip detaches from the glass surface. In the end, platinum wires were used as electrodes instead for the electrokinetic sorting experiment.

2.3 Results

2.3.1 Performance of Microfabricated Cell Sorter

The performance of any flow cytometer depends on three factors: sensitivity, resolution and measuring rate. Sensitivity, in terms of fluorescence detection, is defined as the minimum number of dye molecules per cell that can be resolved. Several elements such as cell exposure time, excitation intensity, sensitivity of the detectors, photobleaching, light collection efficiency, optical filtration, noise and the overlap of the excitation and absorption spectrum of the dye as well as its fluorescence quantum yield, can decrease the sensitivity of the flow cytometer. Resolution, expressed as coefficient of variation, is mainly limited by three considerations: 1) the stability of the excitation light, 2) the width and stability of the sample flow, and 3) the intensity of the signal and background noise, which contribute to fluctuations in detection. The measuring rate for flow cytometers is the number of cells per given time passing through the analysis point without any coincidences. In this case, I want to measure the fastest time the sorter can respond upon the detection of a desired cell. Thus, three parameters were measured to verify the performance of the microfabricated cell sorter: the coefficient of variance in measurements, the sensitivity of the detection system and the response time in a sorting event.

The coefficient of variance (CV, defined as the standard deviation of the peak divided by the mean for an uniform population of particles) is routinely used as a measure of the system's precision in fluorescence detection. The CV for this micro-fabricated cell sorter system ranges from 2% to 5%, measured with LinearFlow Green Flow Cytometry Intensity Calibration Beads (Molecular Probes, Eugene, OR). This discrepancy may depend upon several factors, such as the relative intensity of different calibration beads and the bias settings on the PMT. Specifically, the depth of the channel also affects the CV of the system. A higher CV is obtained when a deeper channel is used due to a greater variation in the position of the beads. Interestingly, different methods of modifying the elastomer to be more hydrophilic also influence the CV. Polyurethane coating of the elastomer yields the best CVs, but the CVs deteriorate with each subsequence use. Although HCl treated channels produce CVs that are 0.5–1% higher than those of the polyurethane coating, their CVs remain consistent with each usage. The MAKON 6 channels give the highest CVs among the three different hydrophilic treatments, about 1–2% higher than the CVs obtained from the HCl treated channels. Regardless, these CVs are already comparable to those obtained from a conventional FACS.

The sensitivity of this system is about 200 dye molecules at 100 events/sec, of YO-YO 1 (quantum yield = 0.52), a DNA intercalating fluorescent dye. This is at least twice as sensitive as the most sensitive flow cytometers commerically available, which can detect about 1000 fluorescein molecules (quantum yield = 0.9) at 1000 events/sec. In addition, an advantage of μFACS is the small detection volume, which in this case is approximately 100 femtoliters, which greatly reduces background fluorescence in the suspension.

The response time of μFACS consists of two parts: 1) time from a signal on the PMT to the actual change in voltage settings of the Pt electrodes and 2) the time from the switching of the voltage settings to actual change of fluid flow at the T-junction. Measurements were taken using wild-type GFP HB101 cells flowing through the detection window to observe the response times of the cells inside the channels and the hardware. The time from a signal on the PMT to the actual change

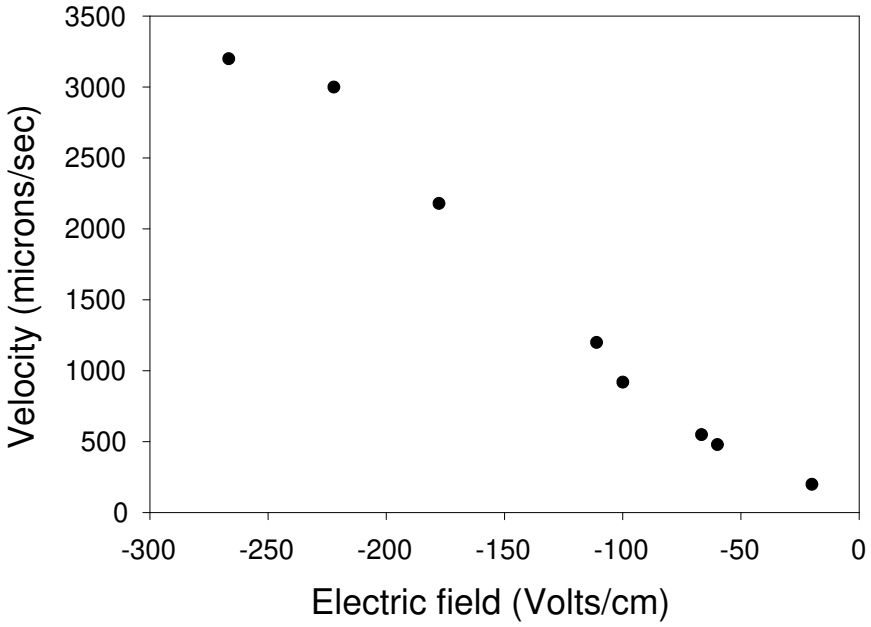

Figure 2.4: A graph of the linear flow velocities of cells in response to the applied electric field strengths inside μFACS. These data were taken on the same device but on two separate days. The width of the detection volume was 12 μm.

in the voltage settings was determined to be between 1.25–1.50 msec, and the actual switching in fluids occurs in less than one millisecond. The whole response time of the device was less than 3 msec for sorting particles electro-osmotically.

The linear flow velocities of GFP expressing *E. coli* cells in μFACS in response to the applied electric field strengths were measured and plotted in Figure 2.4. A PMT was used to observed the fluorescence from each cell as it passed through the interrogation region. The signal pulses from the cells were recorded by an oscilloscope. The widths of the pulses were calculated as the time the cells took to travel through the interrogation point. The linear flow velocities of the cells were derived and plotted against the applied electric field strengths. As Figure 2.4 shows, cell velocities escalate with increasing electric field strengths. However, at above a certain electric field strength (greater than the absolute value of -600 V/cm), these cells began to lose

viability as indicated by their loss of fluorescence inside the microchannels and at the wells. Thus the fastest velocity that could be attained by *E. coli* cells inside μFACS is $\sim$3–5 mm/sec. Cell viability would be greatly compromised if higher electric field strength is applied.

2.3.2 Sorting Schemes

Different algorithms for sorting in the microfluidic device can be implemented by the computer. The standard "forward" sorting algorithm consists of running the cells from the input channel to the waste channel until a cell's fluorescence is above a preset threshold, at which point the voltages are temporarily changed to divert the cell to the collection channel. With electrokinetic flow, switching is virtually instantaneous and throughput is limited by the highest voltage that can be applied to the sorter (which also affects the run time through ion depletion effects). In contrast, a pressure-switched scheme does not require high voltages and is more robust for longer runs. However, mechanical compliance in the system is likely to cause the fluid switching speed to become rate-limiting with the "forward" sorting program. Since the fluid is at low Reynolds number and is completely reversible, when trying to separate rare cells one can implement a sorting algorithm that is not limited by the intrinsic switching speed of the device. The cells flow at the highest possible static (non-switching) speed from the input to the waste. When an interesting cell is detected, the flow is stopped. By the time the flow stops, the cell will be past the junction and part way down the waste channel. The system is then run backwards at a slow (switchable) speed from waste to input, and the cell is switched to the collection channel when it passes through the detection region. At that point, the cell is saved and the device can be run at high speed in the forward direction again. This "reverse" sorting method is not possible with standard FACS machines and should be particularly useful for identifying rare cells or making multiple time course measurements of a single cell. Higher throughput rates could be achieved with this algorithm. I first demonstrated reverse sorting with beads using electrokinetic flow and later with cells in the second

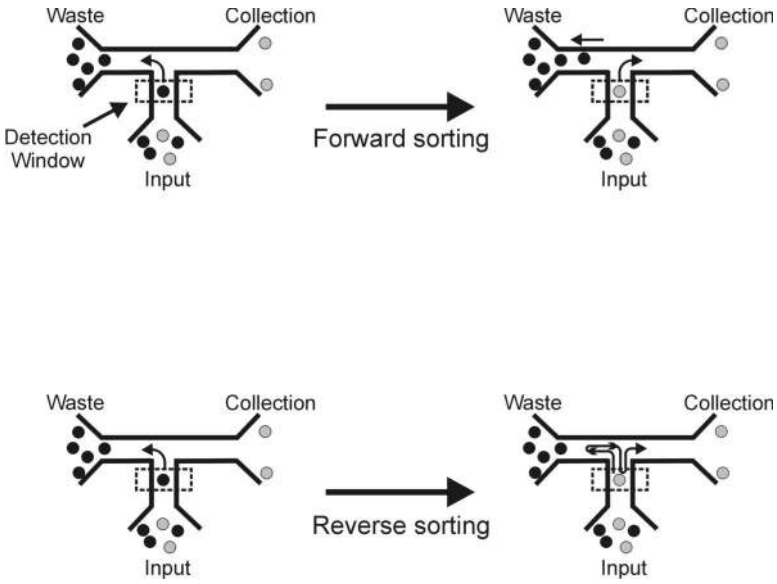

Figure 2.5: A schematic of forward and reverse Sorting.

generation cell sorter which was with integrated valves and pumps. (See Figure 2.5.)

2.3.3 Decision Making and Sorting Algorithms

Methods of sorting in microfluidic devices are essentially different from the conventional aerosol droplet sorters. In any sorting logic, the detection of each cell first determines whether or not the criteria are met; when these criteria are met, a logic signal is generated to trigger sorting. For conventional aerosol droplet sorters, the detection of the cell usually occurs in a jet stream and the sorting occurs after the stream has been broken up into droplets that contain zero to two cells. Depending on the distance between the interrogation point and the breakoff point, the time lag between these two points may be tens to hundreds of microseconds. For μFACS, detection occurs $\sim$5 μm before the T-junction and sorting is immediately performed in continuous flow. This may allow for more accurate and synchronous sorting (within ten microseconds time frame) which can be critical for time-course measurements or any downstream analysis. In addition, with reverse sorting algorithm, the detection of the cell actually occurs two to three times more during sorting before the cell is finally shuttled into the collection channel.

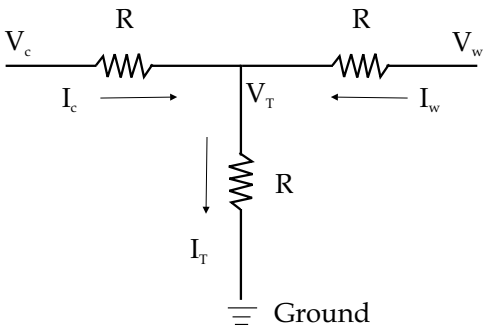

Figure 2.6: T-channel wire diagram. The arms of the T channel can be considered as three wires with identical resistance since they have the same dimensions.

For the electrokinetic cell sorter, both forward and reverse sorting algorithms were written in C++[1]. One electrode at the input was at ground and voltage potentials were applied to the other two electrodes at the collection and waste wells. As Figure 2.6 shows, the arms of the T channel can be considered as three wires with identical resistance (since they have the same dimensions). So the currents from the collection and the waste wells combine at the T-junction and go into the input well.

$$I_c R = V_c - V_T \ ; \ I_w R = V_w - V_T \ ; \ I_T R = V_T \tag{2.6}$$

$$I_c + I_w = I_T \tag{2.7}$$

$$(V_c - V_T) + (V_w - V_T) = V_T \quad since \quad I_c R + I_w R = I_T R \tag{2.8}$$

$$V_c + V_w = 3V_T \tag{2.9}$$

If the collection channel is set to be "floating", then $V_w = V_T$. Ideally, there should not be any current flowing into the "floating" collection channel and hence no electrokinetic flow. This also means that $V_c = 2V_w$.

Forward Sorting

For forward sorting, the voltage potentials are initially set as $V_c = 2V_w$. So all the electrokinetic flow goes into the waste channel, that is, $I_c = 0$. When a cell's

[1]Written by Anne Y. Fu

	V_w	V_c	Time delay (msec)
Beads			
	10	22	150
	30	60	150
	40	80	150
	50	110	150
E. coli cells			
	-50	-110	150

Table 2.1: Voltage settings (in volts) for V_w and V_c for electrokinetic forward and reverse sorting of beads and cells. Notice that the voltage potentials are positive for beads and negative for cells.

fluorescence reaches above a set threshold voltage, these two voltage potentials switch, that is, $V_w = 2V_c$. The cell is directed into the collection channel for a certain period of time before the voltage potentials switch back.

Reverse Sorting

Similarly, the reverse sorting algorithm is such that the default voltage setting is $V_c = 2V_w$. When the sorting signal triggers, the cell is slowly reverted back into the detection region again at a tenth of the original flow rate, that is, $-\frac{1}{10}V_c = -\frac{1}{10}2V_w$. After the second detection, the cell is slowly directed into the collection channel, $\frac{1}{10}V_w = \frac{1}{10}2V_c$, before switching back to the default potentials. Table 2.1 lists some of the voltage potentials used for various runs of sorting for both forward and reverse sorting of beads and cells.

Unfortunately, due to evaporation and uneven pressure buildup in the two output wells, the voltage potentials have to be readjusted from time to time in order to maintain accurate sorting for both forward and reverse sorting.

2.3.4 Sorting with Beads and Bacterial Cells

The use of μFACS for forward and reverse sorting with electrokinetic flow was demonstrated with fluorescent beads of different emission wavelengths in different ratios and

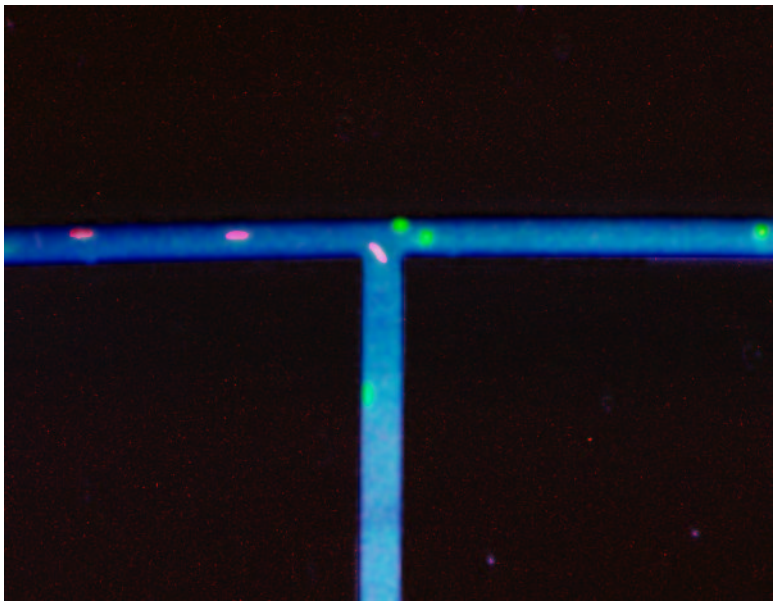

Figure 2.7: A snapshot of a sorting event. A red bead is being sorted into the collection channel. The green beads in the waste channel are stagnant due to a voltage change which directs the electrokinetic flow into the collection channel.

up to 33,000 beads per hour throughput. Extra reservoir wells were incorporated on the outer side of the three wells in order to avoid ion depletion, and platinum electrodes (with the ground electrode in the input well) were inserted into the reservoir wells. The collection wells were filled with buffer and a mixture of red and blue fluorescent beads was injected into the input well in 10–30 μl aliquots. The optical filter in front of the PMT passed only red fluorescence, allowing selective sorting of red beads. Sorting can be performed for as long as three hours with occasional readjustment of the voltage settings. The coefficient of variation in bead intensity was measured to be 1–3% depending on the depth of the channel and the surface treatment of the elastomer.

Sorting of Beads

Table 2.2 shows that a single pass through the μFACS produced a highly enriched sample of red beads. Whereas the initial concentration of red beads was 7.4%, the collection well held 84% red beads, while the waste well had less than 1%. Similar results were obtained when running in reversible sorting mode when the initial

	Input Well		Collection Well		Waste Well	
	Blue	Red	Blue	Red	Blue	Red
Forward Bead Sorting	0.925	0.074	0.160	0.840	0.998	0.002
Reverse Bead Sorting	0.988	0.012	0.043	0.957	0.999	0.001
Forward *E. coli* Cell Sorting	0.992	0.008	0.693	0.307	0.992	0.008

Table 2.2: Results of beads and *E. coli* cell sorting.

concentration of red beads was lowered to 1% (Table 2.2). Run times varied from 10 minutes up to 3 hours. With both forward and reverse sorting, enrichments of 80x-97x were obtained in single runs, where the enrichment is defined by the increase in the fractional concentration of red beads.

Preparation of beads is as follows. Red and blue fluorescent beads (1 μm diameter, Interfacial Dynamics Corporation, Portland, OR) were suspended in PBS (137 mM NaCl, 2.7 mM KCl, 4.3 mM $Na_2HPO_4{\cdot}7H_2O$, 1.4 mM KH_2PO_4) with 10% BSA (1mg/mL) and 0.5% Tween 20 in 10:1 blue:red ratio and overall concentration of 1.5%. Fluorescence of the beads was excited by a 100 W mercury lamp with 488DF20 optical filter. A 630DF30 optical filter (Chroma Technology Corp., Brattleboro, VT) was used to select the red fluorescent emission. The μFACS device had 3 x 4 μm channels. A 100:1 blue:red ratio was used for reverse sorting.

Sorting of *E. coli* cells

I have also demonstrated that the device can sort living *E. coli* cells, and that the cells are viable after sorting. Different ratios of wild-type to GFP-expressing *E. coli* cells were introduced into the input well (volume ranges from 10–30 μl of sample); the collection wells were filled with 10–30 μl of buffer with 10^{-5} M sodium dodecyl sulfate (SDS). After inserting the three platinum electrodes into the wells (with the ground electrode in the input well), the voltages were set for forward sorting. After sorting for 2 hours, cells were collected with a pipette and streaked onto LB plates (or other antibiotic-containing plates) and incubated overnight at 37° C for colony counting. I achieved enrichments of 30x with yields of 20%, where the yield is defined

by the number of colonies on the plate divided by the number of positive fluorescence events detected in the device. The sorted cells show relatively constant viability in electric fields up to 100 V/cm, corresponding to velocities of 1–3 mm/sec.

Preparation of *E. coli* cells for sorting is as follows. The *E. coli* cells (HB101) expressing GFP were grown at 30° C for 12 hours in LB liquid medium containing ampicillin (1 colony was inoculated into 3 mL medium containing 50 μg/mL of ampicillin). Wild-type *E. coli* HB101 cells were incubated for 12 hours in LB-only medium. After incubation, HB101 and GFP-expressing HB101 *E. coli* cells were resuspended into PBS (ionic strength = 0.021) three times and stored at 4° C for sorting. Immediately before sorting, the cells were resuspended again into phosphate buffer (4.3 mM $Na_2HPO_4{\cdot}7H_2O$, 1.4 mM KH_2PO_4) containing 10^{-5} M SDS and diluted to a concentration of 10^9 cells/mL. The cells were filtered through a 5 μm syringe filter (Millipore Bioscience Inc., Bedford, MA) for elimination of any elongated cells. A μFACS device with 10 x 4 μm channels was used. Fluorescence was excited by the 488 nm line of an Argon ion laser (6 mW into the objective), Coherent Innova 70 (Laser Innovations), and the emitted fluorescence was filtered with a 535DF20 filter.

2.4 Conclusion

I have demonstrated a disposable microfabricated fluorescence-activated cell sorter using soft lithography for sorting various biological entities. Compared with a conventional FACS machine, this sorter provides higher sensitivity for bacterial cells, no cross-contamination, and lower cost. We have used these chips to obtain substantial enrichment of micron-sized fluorescent bead populations of differing colors. Furthermore, I have separated *E. coli* cells expressing GFP from a background of nonfluorescent *E. coli* cells and shown that the bacteria are viable after extraction form the sorting device. These sorters can function as stand-alone devices or as components of an integrated microanalytical chip.

Chapter 3
A Microfabricated Cell Sorter Integrated with Microvalves and Micropumps

Since the introduction of the first microfabricated electrokinetic analytical device in 1991[9], much work has been focused on using electrokinetic forces to separate ionic species, such as peptides and DNA fragments, through capillary electrophoresis[50, 51, 52, 41, 17]. Gradually, it has become apparent that the true potential of microfabricated devices lies in the ability to integrate a complete analysis system "on chip". Such a complete analysis system in a microfabricated device will need to perform more than just separation and detection. This lab-on-chip will have to integrate functionalities such as sample handling, mixing, incubation, sorting, transportation, recovery and automation for reproducibility. Thus, other means of controlling fluid flow within the microfabricated devices have been studied. Dielectrophoresis[44, 46] and pressure-switching[45] have been used to create valveless switches for separation of particles and cells within microchannels. Spatially fixed temperature zones allow for incubation at various regions of the microchannels[22]. Multiple ports and plugs can dispense different reagents for dilution and enzymatic reactions[21, 53]. Advances in developing an integrated analysis system have led to an emergence of chips that can perform enzymatic assays[54, 55], immunoassays[50, 56], polymerase chain reaction[22] and cell sorting[46, 26].

I have previously described in Chapter 2 my efforts in developing a microfabricated elastomeric cell sorter[26]. Using electrokinetic flow, I have demonstrated sample dispensing, interrogation, automation, sorting and recovery. Cell sorting has become an indispensable part in the studies of cellular metabolism at the single cell level[57, 58]. For future applications, these single-cell analyses will demand immediate treatment of cells either before or after sorting with minimal time variation and sample loss.

Thus there is a need for a microfabricated cell sorter that can integrate more functionalities. Electrokinetic flow and/or direct pressure application alone will not be able to meet these demands.

Multilayer soft lithography is a new micromachining technique that exploits the elasticity and the surface chemistry of silicone elastomers in order to create monolithic microvalves within microfabricated devices[59]. This technique is based on rapid prototyping and replica molding methods of soft lithography. A monolithic chip can be made of multiple layers of elastomeric channels, having each layer individually cast from a microfabricated mold. In a typical two-layer system, the bottom layer consists of the fluidic line where the sample will be introduced and interrogated. The top layer has the control line where the valves will be pneumatically actuated. When pressurized air or nitrogen is introduced into the control line, the thin membrane between the two lines is deflected downward and seals off the fluidic line. A valve is created in this way. The simplicity and flexibility in multilayer soft lithography allows for integration of many different operations on the same chip. Unger *et al.* have fabricated switching valves and peristaltic pumps for sample dispensing and switching[59], and Chou *et al.* have made rotary pumps for mixing and incubation[60, 61].

Using multilayer soft lithography, I have developed a microfabricated elastomeric cell sorter integrated with microvalves and micropumps [62]. My initial efforts in sorting cells *via* electrokinetic flow demonstrated that I can sort and recover bacterial cells in microfabricated devices in an automated fashion. But the electrokinetic sorter is unsuitable for high throughput screening and other biological applications because of its low recovery rate, buffer incompatibilities and frequent change of voltage settings due to ion depletion, pressure imbalance and evaporation. The current cell sorter with microvalves and micropumps is a step closer to the realization of an integrated lab-on-chip. It has incorporated switching valves, dampers and peristaltic pumps for sorting, sample dispensing, flushing, recovery and absorption of any fluidic perturbation (See Figure 3.5). Other microfluidic functions can be easily integrated for kinetic studies or treatment before and/or after sorting events. The active areas of these microvalves and micropumps are much smaller than those made by Unger *et al.* and Chou *et*

al. in order to accommodate the size of a single bacterial cell. The active volume of one valve on this integrated sorter can be as small as 1 picoliter. The cell sorter also reduces concerns for buffer compatibility, automation and viability of cells. I have further exploited different algorithms of interrogation within this sorter, such as reversible sorting and cell trapping. I have also greatly improved the sorting accuracy and recovery efficiency using this integrated sorter relative to previous work. Finally, I have demonstrated the ability of this sorter to integrate various microfluidic functionalities into one chip to perform a complicated task in an automated fashion.

This chapter presents my progress in developing an integrated cell sorter in five sections. Section 3.1 summarizes my efforts in fabricating an integrated microfabricated cell sorter using multilayer soft lithography. Section 3.2 describes the flow velocities of the cell sorters and a new interrogation scheme called cell trapping. Section 3.3 presents the software programs used for data acquisition and analysis. Section 3.4 introduces the sorting logistics used for reverse sorting algorithm. Section 3.5 discusses the properties of the integrated cell sorter and its sorting results.

3.1 Fabrication and Design

3.1.1 Multilayer Soft Lithography

Fabrication and design of the integrated pneumatic-driven cell sorter adopted features from the electrokinetic sorter and novel engineering using multilayer soft lithography. This integrated cell sorter has the shape of a "T" for sorting as in the electrokinetic sorter, but with valves and pumps incorporated. As shown in the schematic layout of Figure 3.5, the sorter has two layers. The top layer has the control lines for valves and pumps and the bottom layer has the fluidic lines. The fluidic layer has channels of 30 μm in width which narrows down to 20 μm, and eventually tapers down to 6 μm at the T-junction. Supports are lined up along both sides of the channels for visualization and alignment purposes. Fluidic holes are incorporated at the ends of the "T" for injection of cell samples and buffers. Collection wells of 1 millimeter in diameter at the

arms of the "T" are used for recovery. The control layer has distinct functionalities at different regions of the "T" for controlling fluid flow within the fluidic lines. Three valves, acting as a peristaltic pump, have a valve active area that is 80 μm long and 30 μm wide. These valves are 100 μm apart. Three dampers of similar dimensions are placed immediately following the peristaltic pumps to absorb any energy from fluidic perturbations introduced by pumping. Three pairs of switching valves are placed at the arms of the "T", having the dimensions of 20, 30 and 50 μm wide. These valves have a valve active area of 20 x 20 μm, 30 x 30 μm and 50 x 30 μm, respectively.

The process of multilayer soft lithography is divided into two parts: fabrication of silicon molds and fabrication of elastomeric chips. Since each layer is individually cast from a microfabricated mold, fabrication methods of molds for different layers of the device are presented. Fabrication details of a multilayer elastomeric chip from silicon molds and the chemistry of silicone rubber are also discussed.

Silicon Molds

In multilayer soft lithography, each layer is cast individually from a different microfabricated mold. There are two ways to fabricate molds from silicon wafers for soft lithography. One is to etch into the silicon as previously mentioned in Chapter 2, and another is to pattern a thin layer of photoresist onto the silicon wafer. Although an etched mold is permanent and chemically resistant, the rapid prototyping process of patterning photoresist onto silicon wafers allows molds to be made within a few hours. In addition, different photoresists have different light sensitivity, surface chemistry and viscosity. Combinations of these parameters allow the rapid prototyping process to be versatile for making a variety of different dimensions and shapes of the channels. Thus a good choice of photoresist is critical for the success of fabricating a mold of desired dimensions.

The cross-sectional shape of the channels is also a critical factor for the ideal performance of the valves. According to Unger *et al.* , only flow channels with a round cross section are able to close completely as shown in Figure 3.1[47, 59]. However, after obtaining a desired thickness from patterning photoresist on the mold, flow channels

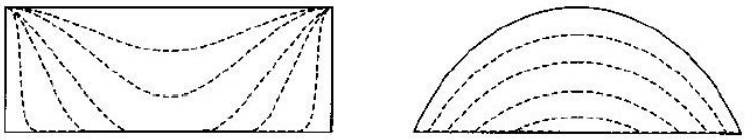

Figure 3.1: Cross sections of a trapezoidal-shaped and a round-shaped flow channels. Profiles of the channels when they are under actuation pressure. A flow channel with a round-shape cross section is able to completely seal off the channel under pressure. A channel with a trapezoidal-shape cross section will have leakage from the sides.[47, 59]

are usually of a rectangular or a trapezoidal shape due to UV light diffusion and the photolithography process. These flow channels fail to have complete closing of the valves. When under pressure introduced from above, a round-shaped flow channel is able to seal off a section of the channel by flattening completely from the center to the sides of the cross section whereas a trapezoidal-shaped flow channel fails to seal completely from the sides. Thus a further chemical modification of the photoresist after photolithography is needed. If the photoresist (an amorphous polymer) is heated above its glass transition temperature and with sufficient time, it will reflow to the edges and become rounded. This reflow process is used to tailor off any sidewall angles on the photoresist to completely round the flow channels.

My initial goal is to fabricate a mold of approximately 3–6 μm thickness for the fluidic channel, similar to the dimensions of a bacterial cell (1 x 2 μm). As summarized in Table 3.1, three different positive photoresists were investigated for fabricating the fluidic channel of the bacterial cell sorter. Shipley SJR 1813, SJR 1818, SJR 5740 can all be spin-coated to have a thickness in the range of 2 to 10 μm. All three photoresists were carefully examined to see which gives the best results.

SJR 1813 is the least viscous photoresist of the three mentioned above. It normally achieves a thickness of 2 μm, spin-coating at 2000RPM (Set 1). This photoresist was used to pattern the wafers for the RIE process of the electroosmotic sorter. However, in order to achieve a thickness of 4 μm, SJR 1813 had to be spin-coated twice at 2000 RPM (Set 2). The height of the channels developed is about 3.5 μm. This process is relatively easy but it requires a precise timing of exposure and development during photolithography. The two-layer processing of the photoresist

may lead to different layers requiring different times of exposure and development. This would cause problems in developing well-defined and fine features such as 5 μm wide channels at the T-junction. Imperfect timing in exposure and development can cause the T-junction to become distorted. Slow-heating SJR 1813 at low temperatures for 40 minutes will completely round the flow channels. However, these results were inconsistent due to variations resulting from the two-layer photoresist spin-coating process.

SJR 1818 is the second viscous photoresist in this group. It has a thickness of 3 μm when spin-coated at 2000 RPM (Set 3). This photoresist seems to be the most ideal one since it obtains the right height with the least amount of effort. However, the reflow process of the photoresist from heating reduces the channel height to 2–2.5 μm at the T-junction, which increases the possibility of clogging up the flow channel.

SJR 5740 is a relatively thick photoresist originally used by Unger *et al.* to fabricate their molds. Most of my work on the cell sorter was also done using SJR 5740. It obtains a thickness of 10 μm when spin-coated at 2000 RPM (Set 4). Higher spin-rate is needed to decrease the thickness to 4–6 microns. When SJR 5740 is spin-coated at 8000 RPM, fine features such as the 5 μm width channels are easily overdeveloped (Set 5). The adhesion of SJR 5740 to a silicon wafer is also reduced. The T-junction of the cell sorter becomes distorted or disappears from the mold after developing. But when SJR 5740 is spin-coated at 5000 RPM and 6000 RPM, a thickness of 6.5 μm (Set 6) and 6 μm (Set 7) can be obtained respectively.

Yet, the 6 μm high T-junction suffers greatly from the reflow process which results in an uneven redistribution of SJR 5740. Aggregation of photoresist appears at the tip of the T-junction and at the 20 μm width channel region. This greatly decreases the height of the 5 μm width channel region. Hence clogging of cells and beads was observed when using these flow channels. Baking on a hot plate of 180° C for 30 minutes can easily round a 10 μm deep channel (Set 4). However for shallower channels of 4–6 μm deep, the reflow process has to occur at a much slower rate and a lower temperature of 80° C to prevent uneven distribution of the photoresist (Sets 2–3, 6–8).

Set	Photoresist	Spin-rate (RPM)	Baking Time (90° C)	Channel Height (μm)	Reflow Process
1	SJR 1813	2000	30 min	2	n/a
2	SJR 1813	2000×2	20 min×2	3.5	80° C, 40 min
3	SJR 1818	2000	30 min	3	90° C, 30 min
4	SJR 5740	2000	1 hr	10	180° C, 30 min
5	SJR 5740	5000	1 hr	6.5	n/a
6	SJR 5740	6000	1 hr	6	80° C, 15 min
7	SJR 5740	8000	1 hr	4	n/a
8	SJR 5740	6000, O_2 plasma	1 hour	4	80° C, 15 min

Table 3.1: Characterization of different photoresists. SJR 1813, 1818 were developed in CD-30 and SJR 5740 were developed in 20% Microposit Developer 2401.

The aspect ratio of height over width of the flow channel is also an important issue for the success of the integrated sorter. Too high of an aspect ratio will encounter problems in complete closing of valves in terms of geometry and pressure. A 6 μm deep and 30 μm wide flow channel would require a high actuation pressure of greater than 150-160 kPa to completely close. Usually, the thin valve membrane ruptures first before the valves can be closed completely. To reduce the high aspect ratio of the flow channel, oxygen plasma was used in Set 8 to isotropically etch the photoresist patterned on the silicon wafer. This etch has a rate of 0.03 μm per minute for SJR 5740. Now the height of the photoresist can be reduced with dry etch instead of using a higher spin rate. Exposure to oxygen plasma for 1 hour etches away about 1.8 μm of SJR 5740 spin-coated at 6000RPM. This will result in a flow channel of 4 μm depth (Set 8). The etching also rounded the flow channel slightly due to the heat released from the etching. Further heating at low temperature is needed to completely round the flow channel.

The final fabrication procedure of my molds for the bacterial cell sorter is as follows. The control layer and the fluidic layer were cast from two different molds. The depth of the fluidic channel was 3.5–5 μm whereas the depth of the control channels was 10–12 μm. All silicon wafers were incubated with hexamethyldisilazane (HMDS) vapor for 2 minutes before photolithography. For the control channel, the silicon wafer was spin-coated with photoresist (Shipley SJR 5740) at 2000 RPM (ramping time: 15 secs, spin time: 60 secs). The wafer was then softbaked in the oven at 90° C

$$Si + CH_3Cl \xrightarrow{Cu} \begin{array}{lll} Me_3SiCl & bp & 58^\circ\,\mathrm{C} \\ Me_2SiCl_2 & bp & 70^\circ\,\mathrm{C} \\ MeSiCl_3 & bp & 68^\circ\,\mathrm{C} \end{array} \tag{3.1}$$

$$2Me_2SiCl_2 + 4H_20 \longrightarrow 2Me_2Si(OH)_2 + 4HCl \tag{3.2}$$

$$\underset{linear\ siloxane}{HO[(CH_3)_2SiO]_mH} \xrightarrow{KOH} Cyclic\ Dimethyl\ Tetramer \tag{3.3}$$

$$Cyclic\ Dimethyl\ Tetramer + Chain\ Stopper \xrightarrow{KOH} -(Me_2SiO_2)_n- \ PDMS \tag{3.4}$$

Table 3.2: Polydimethylsiloxane manufacturing process[63]. Silica (sand) is first reduced to elemental silicon metal. This metal is then grounded and reacts with methylchloride in the presence of a copper catalyst (equation 3.1). One of the products of this reaction, dimethylchlorosilanes, is hydrolyzed to form silanols which then condenses to form cyclic silanes and other low molecular weights silanes (equation 3.2). These low molecular weight silanes are reacted with KOH to form dimethyl tetramers, a cyclic silane (equation 3.3). These tetramers are then linearized to become PDMS by the addition of a strong base and a monofunction silane (equation 3.4).

for 60 minutes. A chrome glass mask was used for photolithography. The wafer was exposed and developed in 20% Microposit Developer 2401 for 1.5 minute.

For the fluidic channel, the silicon wafer was spin-coated with SJR 5740 at 6000 RPM (ramping time: 15 secs, spin time: 60 secs). Then the wafer was softbaked in an oven at 90° C for 60 minutes. The photolithograpy process was the same as above. After photolithography, the wafer was placed in an oxygen plasma for 45 minutes to 1 hour in order to etch a height of 3.5–5 μm of the photoresist. Then the wafer was baked on a hot plate at 80° C for 20 minutes.

Elastomers

Silicone elastomers retains much of the same chemistry as the natural organic polymers. Yet, its unique silicon-oxygen linkage provides much greater stability to high

temperature and chemical resistance. The commercial preparation of silicone elastomers is shown in Table 3.2[63]. First, silica (sand) is reduced to elemental silicon metal. The elemental silicon metal is then grounded and reacts with methylchloride in the presence of a copper catalyst at 300° C. The products of this reaction are mono-, di-, and trimethylchlorosilanes (equation 3.1). These silanes can be purified using fractional distillation. After distillation, the dimethylchlorosilanes[1] are hydrolyzed to form silanols which then condenses to form cyclic silanes and other low molecular weight silanes (equation 3.2). These low molecular weight silanes are reacted with a base (KOH) to form dimethyl tetramers, a cyclic silane (equation 3.3). These tetramers are then linearized to become polydimethylsiloxane (PDMS) by an addition of a strong base and a monofunctional silane (equation 3.4). The monofunctional silane acts as a chain stopper and determines the viscosity of the linearized polymer.

Different organic side chains can be substituted in place of methyl on the silicon-oxygen backbone of PDMS. These substitutions serve to optimize a certain property of the elastomer as required by a specific application. The inclusion of vinyl groups at various concentrations greatly increases the cross-linking efficiency of the polymer and yields elastomers with lower compression set. The substitution of phenyl groups allows the polymer to be more flexible at low temperatures down to -93° C. The inclusion of trifluoropropyl groups yields elastomers with higher resistance to many harsh chemical environments. An elastomer can be made by mixing different concentrations of these four functional groups, methyl, vinyl, phenyl and trifluoropropyl, in order to meet the demand of different applications.[63]

In addition, a commercial silicone rubber is compounded with three main ingredients: fillers, processing aids and curing agents. A fine, high-surface filler, such as fumed or precipitated silica, acts as a reenforcement to the weakly structured silicon polymer. These fillers react through hydrogen bonding with the silicon-oxygen backbone, yielding elastomers with lower compression set. However as the uncured

[1]Dimethylchlorosilanes are used to form linear chains of silicone polymers whereas trimethylchlorosilanes are used to form three-dimensional cross-linking network for rigid, nonelastomeric molding.

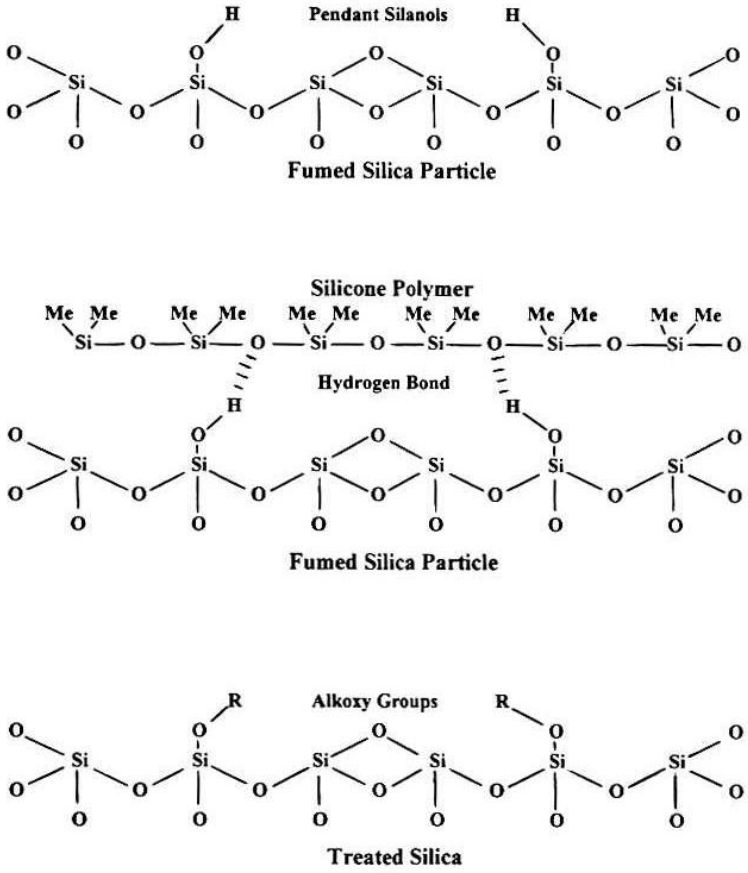

Figure 3.2: Commercial compounding of silicone rubber. Fillers and processing aids are the compounding ingredients for silicone rubber. Fillers strengthen the backbone of the silicone polymer through hydrogen bonding. Processing aids modifies the chemical moieties on the fillers to prevent excessive cracking of the polymer[63].

compound stores with time, this interaction increases and the compound will harden and crack instead of forming a smooth surface. Processing aids, on the other hand, act as a softener to modify the interaction between silicone polymer and its filler. These aids chemically modify the hydroxyl groups on the filler to reduce the hydrogen bonding interaction. This will increase the processability and shelf life of the silicone compound. These aids can be added either during the compounding process or as a pretreatment to the silica fillers (see Figure 3.2).

Curing agents are added for the vulcanization of silicon rubber. Traditionally, curing agents are organic peroxides which can decompose to free radicals and react with the methyl and vinyl groups of silicone polymer. The vinyl groups have a

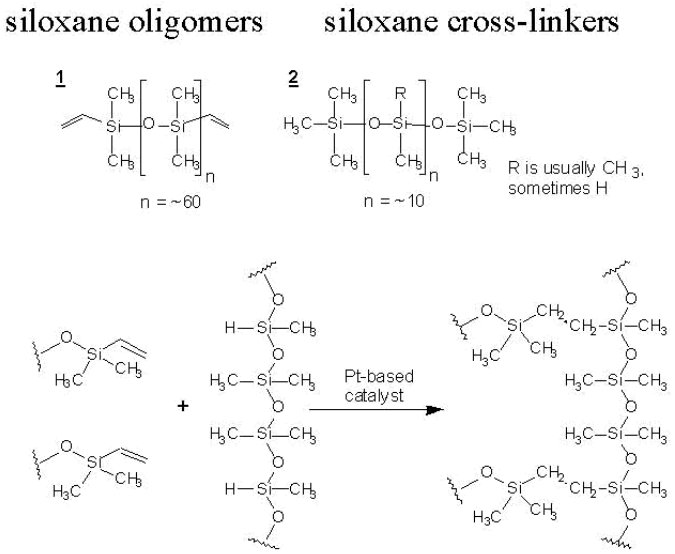

Figure 3.3: Room temperature vulcanization: cross-linking reaction of PDMS and its curing agent[64]. In the presence of a platinum catalyst, an addition reaction occurs in which a silicone hydride (SiH) is cross-linked to the vinyl group of the silicone polymer. This reaction occurs without any by-product and proceeds actively at room temperature.

much higher reaction rate and thus have a much higher number of cross-links. The number of cross-links within the polymer determines the final physical profiling of the resulting silicone rubber. An alternative to vulcanization is called an addition cure. An addition cure utilizes a silicone hydride (SiH) as a cross-linking agent to the methylvinyl polymer. In the presence of a platinum catalyst, an addition reaction occurs in which the hydride is cross-linked to the vinyl group of the silicone polymer. This addition reaction occurs without any by-products, such as water, and proceeds quite actively at room temperature (see Figure 3.3). Thus this type of silicone rubber is known as "room temperature vulcanization" or RTV.

A complete silicone rubber is typically compounded with the three ingredients mentioned above. Other additives, such as silicone fluids and metal oxides, can be added to enhance certain properties of the silicone rubber, such as self lubricant or oil resistance. These additives are listed in Table 3.3.

Beginning in the 1990's, soft lithography has been slowly gaining recognition in

Additives	Primary Function
Reinforcing filler	Physical and Rheological properties
Extender Filler	Cost Reduction and Oil Resistance
Process Aid	Processability and Shelf Life Stability
Organic Peroxide	Cross-linking Agent
Metallic Oxide	Oil and Reversion Resistance
Platinum Complex	Addition Cure Catalyst and/or Flame Retardant
Iron Oxide, Titania	High Temperature Heat Stability
Coupling Agent	Lower Compression Set and Increase Modulus
Phenyl Silicone Fluid	Self-Bleed or Self-Lubrication
Teflon Powder	Increase Green Strength

Table 3.3: Additives of a commercial silicone rubber[63]. These ingredients can be added to enhance certain properties of the silicone rubber.

fabricating silicone elastomer microfluidic devices for biological and chemical analysis. Many issues concerning the surface chemistry and the elastic properties of the silicon elastomers have been encountered. Especially, in multilayer soft lithography, the composition of PDMS in each layer is different. The fluidic layer has an excess of one component, such as the curing agent, whereas the control layer has an excess of the other component, the silicone polymers. This is to enhance the surface bonding between the two layers to form a monolithic chip (Figure 3.4). Table 3.4 summarizes the results of the thicknesses of the fluidic layers at different spin-rate and PDMS composition. A thickness of 10–12 μm for the fluidic layer of 3–5 μm depth of the integrated cell sorter works best for the pneumatic actuation of the switch valves. Several conditions listed in Table 3.4 can be used for fabricating the fluidic layer. The control layer is not as critical in terms of thickness and PDMS composition. A variety of conditions for the control layer may apply.

I have developed two protocols for making the integrated cell sorter. One protocol is to fabricate the cell sorter out of GE RTV 615 and the other protocol is for Dow Corning Sylgard 184. Both GE RTV and Dow Corning Sylgard use the addition cure method for room temperature vulcanization. The difference between them is the proprietary compounding ingredients of the silicone rubber. GE RTV 615 generally takes

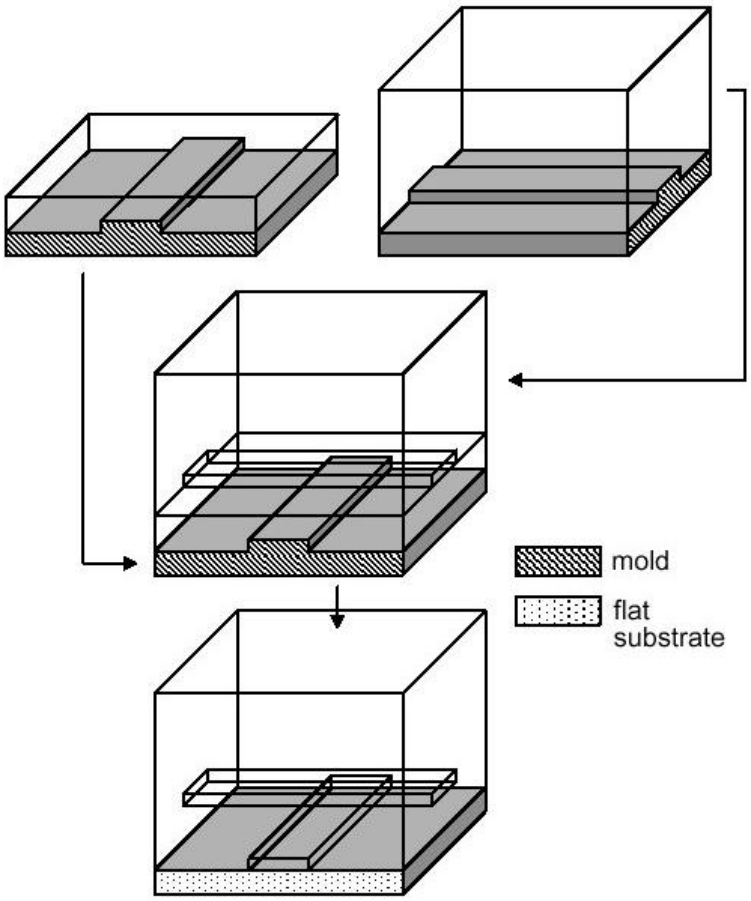

Figure 3.4: Multilayer soft lithography fabrication. Multilayer soft lithography fabrication creates a monolithic chip of multilayers of channels, having each layer individually cast from a microfabricated mold. When both layers are half-cured, the top layer is peeled off from the mold and bonded to the bottom layer. After the bonded layers are fully cured, a monolithic chip is created.

longer to cure and has higher tensile strength. Thus it is easier for us to control the timing and the elasticity of the silicone rubber. I also add a silicone fluid, GE SF-96, to lubricate the elastomer. This lubricant interferes with the cross-linking reaction during vulcanization, decreasing the viscosity of the silicone polymer. Dow Corning Sylgard 184 takes a shorter time for curing and tends to be more resilient than GE RTV 615. Each has its own advantages in terms of fabricating a two-layer system.

GE RTV

For the fluidic layer, General Electric RTV 615 A and B components were mixed in

	A:B Components	Spin Rate (rpm)	Thickness of Layer (μm)
GE RTV 615			
	30:1	2000	40
	30:1	6000	partially cured
	30:1	7000	did not cure
	30:1	8000	did not cure, 8.5
	20:1	7000	12
	20:1	8000	8–10
GE RTV 615	with 30% SF-96 (v/v)		
	20:1	1000	28
	20:1	2000	15
	20:1	3000	8–10
	20:1	5000	5–5.5
	20:1	7000	4–5
SYLGARD 184			
	20:1	4400	12–15
	20:1	5000	8–10
	20:1	6000	6–8

Table 3.4: Fabrication of fluidic layer and its dimensions. Results were obtained using an optical microscope with gridlines from a calibration ruler.

the ratio of 20:1 in a Keyence Hybrid Mixer. This mixture was then spin-coated at 8000 RPM onto the wafer in order to obtain a layer of 10–12 μm thickness. The same thickness can be achieved by adding a diluent, General Electric SF-96, into the mixture (30% v/v) and spin-coating at 3000 RPM. This layer was incubated in the oven at 80° C for 30 minutes. For the control layer, RTV 615 A and B components were mixed in a ratio of 3:1 and spin-coated at 2000 RPM. After incubating at 80° C for 20 minutes, an additional mixture of 10:1 was poured onto the control layer to a thickness of 2 mm. The control layer was then incubated in the 80° C oven for one hour. After incubation, the control layer was peeled off from the mold. A 20 gauge Luer stub adaptor was used to drill out air holes for nitrogen injection. The control layer was properly aligned and bonded onto the fluidic layer. The bonded chip was incubated in the oven at 80° C for 2 hours. Fluidic holes were introduced after the incubation. The monolithic chip was sealed with a glass coverslip and incubated in

the oven at 80° C for 3 hours. This chip was then ready for sorting. A picture of this device is shown in Figure 3.5.

An integrated chip of three layers of channels with PDMS can be made by controlling the incubation time of each layer precisely. Fluidic layer was incubated for 12 minutes only and the control layer was incubated for 20 minutes at 80° C. After the two layers were aligned, the incubation time for bonding the two layers was reduced to 14–15 minutes. This bonded chip was then peeled off from the fluidic mold and aligned to a third silicon mold spin-coated with 5:1 mixture of any thickness. After two hours, the three-channel-layer device can be peeled off. This device can be used with or without sealing to a glass coverslip.

Unfortunately, based on the past years of experience with GE RTV 615, different batches of RTV have slightly different chemical properties. These slight variations ultimately affect my protocols. Thus modifications to the existing protocols have to be optimized for different batches of RTV.

Dow Corning Sylgard 184

A similar fabrication process uses Dow Corning Sylgard 184. Sylgard 184 A and B components were mixed at a ratio of 20:1 and spin-coated onto the fluidic mold at 5000 RPM. A mixture at the ratio 5:1 was then poured onto the control mold to a thickness of 2 mm. Both were incubated in the oven at 80° C for 25 minutes and then bonded together. The bonded chip was incubated in at 80° C for one hour.

Due to its fast curing time, I have never been able to make a completely stand-alone three-layer device from Sylgard 184. A completely enclosed device can be made by spin-coating a mixture of Sylgard 184 onto a glass coverslip and bonding the two-layer device onto the spin-coated coverslip. This chip cannot be peeled off from the coverslip, but it should be optically clear for fluorescence detection and still be completely enclosed in PDMS.

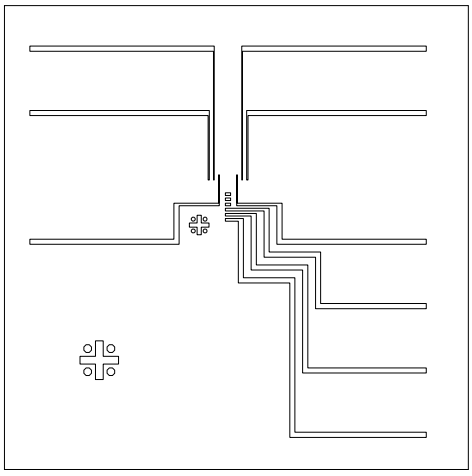

(A) Control Layer

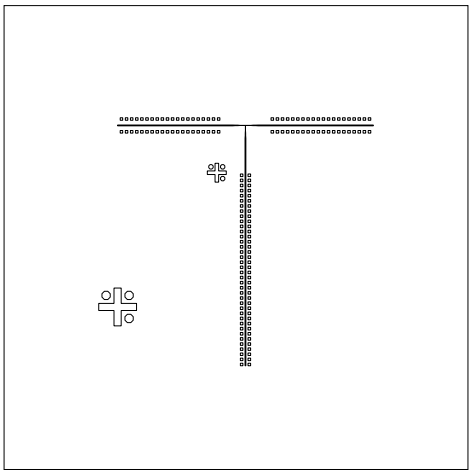

(B) Fluidic Layer

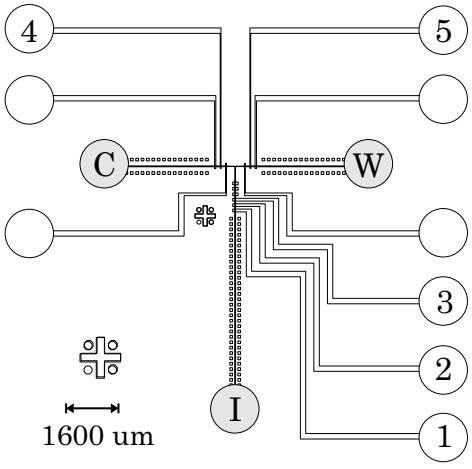

(C) A Microfabricated Cell Sorter

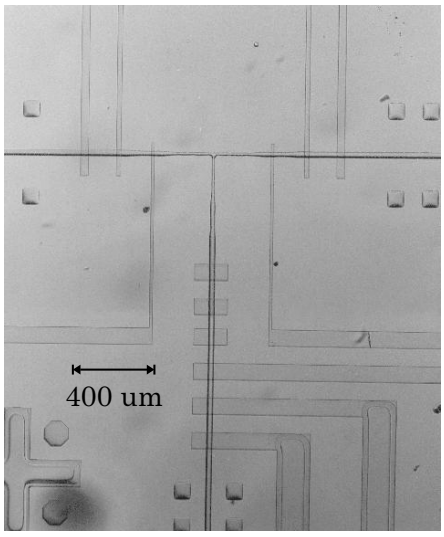

(D) A snapshot of an RTV device

Figure 3.5: A schematic of the integrated cell sorter. This sorter is made of two different layers of elastomeric channels bonded together. (A) The control layer contains lines where pressurized nitrogen and vacuum are introduced to actuate the closing and opening of the valves, respectively. (B) The fluidic layer contains lines where the sample is injected. (C) In this integrated cell sorter, valves 1, 2 and 3 act as a peristaltic pump and valves 4, 5 act as switch valves. Other two pairs of switch valves are not numbered. Holes, labeled as I, C and W, are the input, collection and waste wells respectively. Patterns of 00001 and 00010 actuated by the AT-DIO-32HS card closes valves 1 and 2 respectively, where 0 indicates "valve open" and 1 indicates "valve close". (D) A snapshot of an integrated cell sorter made from GE RTV 615.

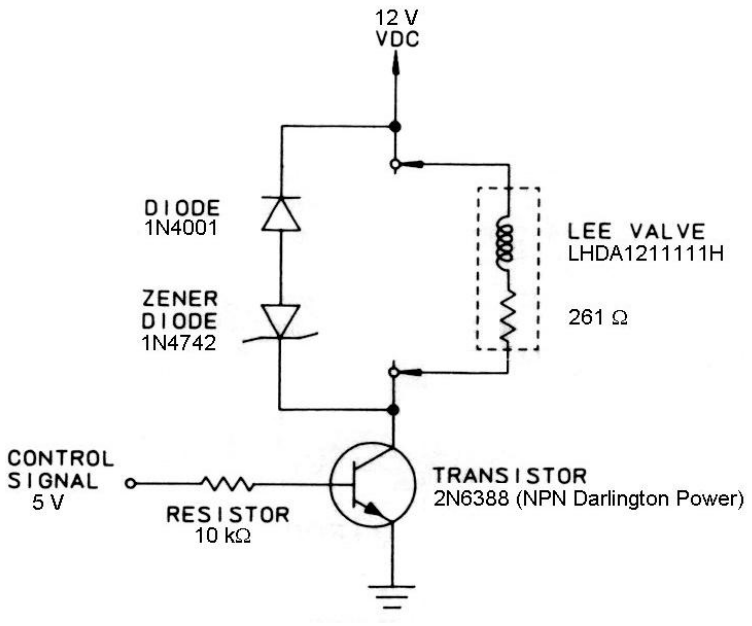

Figure 3.6: Zener-diode circuit diagram.

3.1.2 Pneumatic Control and Optical Setup

The pneumatic control setup was as previously described[47, 59]. Five control lines on the cell sorter were connected the common ports of five external miniature three-way pneumatic switch valves (LHDA1211111H; the Lee Company, West Brook, CT). The normally closed ports on these valves were connected to nitrogen pressure while the normally open ports were connected to vacuum. A National Instruments card (AT-DIO-32HS) digitally controlled the switching of the valves through a fast Zener-Diode circuit (Figure 3.6). Nitrogen pressure applied to the peristaltic pumps was 60 kPa and to the switch valves was 110 kPa.

The integrated cell sorter was mounted on an inverted microscope with an oil immersion objective (100X, 1.3 N.A.; Olympus America Inc., Melville, NY) as previously described in Chapter 2[26]. An Argon laser (Innova 70, Coherent Inc., Santa Clara, CA) was used as an excitation source. Fluorescence was collected by the objective and projected onto a PMT (Hammatsu R928, Hammatsu, Bridgewater, NJ) with custom current-to-voltage amplifier. A National Instrument card (Lab PC1200) digitized any signals from the PMT. A C++ Builder program was written to read signals

from Lab PC1200 and digitally control the pneumatic valves through AT-DIO-32HS to automate cell sorting and trapping as described in Section 3.4.

Alternatively, valve manifolds and breakout boards can be purchased from Fluidigm, Inc. (South San Francisco, CA), for easy setup and plug-and-play. The breakout boards can be connected directly to the NI AT-DIO-32HS card for computerized control. This Fluidigm setup was used for the magnetotactic bacteria studies.

3.2 Flow Velocity and Cell Trapping

Several parameters of the integrated sorter were characterized in preparation for sorting. These parameters are the optimum nitrogen pressure applied to the peristaltic pumps, the linear flow velocity of the cell sorter and the mean reverse time. The mean reverse time is an indirect measurement of the response time of the peristaltic pumps and the actual fluid flow.

The linear flow velocity of fluorescent beads was measured with increasing nitrogen pressure applied to the pneumatic valves. As Figure 3.7 shows, the flow velocity of the beads at 100 Hz pumping rate increases steadily with increasing nitrogen pressure and then falls drastically to zero at 100 kPa. This is due to the incomplete opening of the valves with too high of an actuation pressure. Thus high actuation pressure may adversely affect the peristaltic pump. Devices from different RTV batches were found to have slightly different optimum pressure. But in most devices, 60 kPa is the optimum pressure for peristaltic pumping. Vacuum pressure is constantly applied at the normally open ports for faster opening of the valves. In addition, the rigid polystyrene beads eventually get stuck on the valve membrane. These beads affect the performance of the peristaltic pumps and cause incomplete closing of the valves. GFP *E. coli* cells were used instead for the following measurements.

I then characterized the linear flow velocity of the cell sorter using peristaltic pumps at various pumping frequencies. *Escherichia coli* cells expressing enhanced green fluorescent protein (EGFP) were pumped through the sorter. A photomultiplier tube (PMT) was used to observe the fluorescence from each cell as it passed through

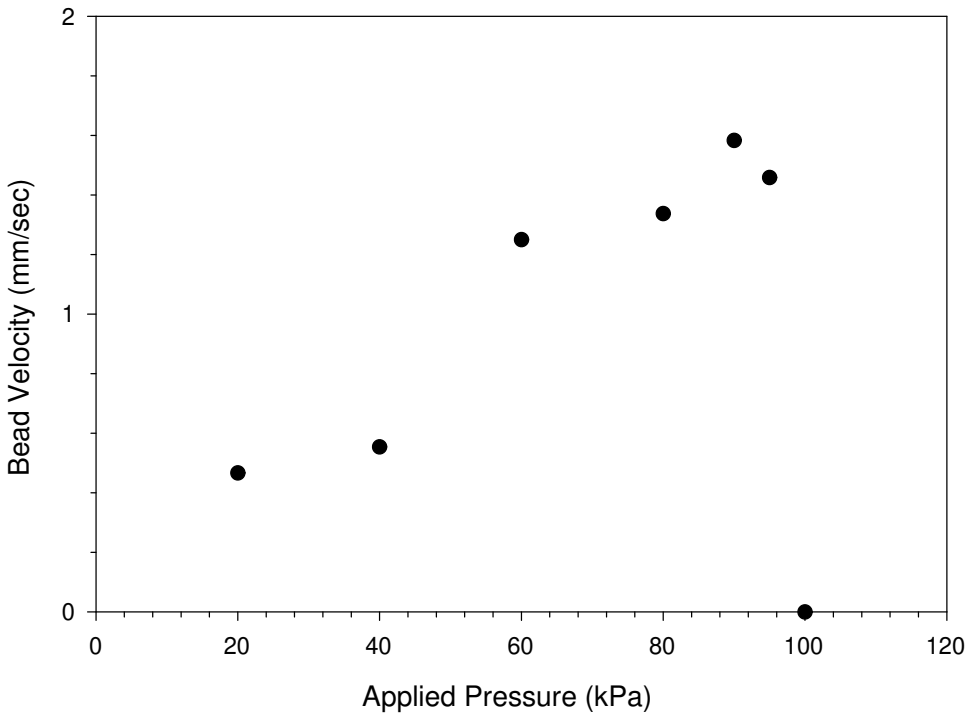

Figure 3.7: A plot of linear flow velocities versus applied pressure from the integrated cell sorter. The velocity of the beads increased as the pressure applied to the peristaltic pumping increased. Beads stopped flowing at 100 kPa due to the incomplete opening of the valves at such high pressure.

the detection region. The detection region was near the T-junction at the 6 μm width channel region. The dimensions of the detection region were 32 μm long along the fluidic channel and 20 μm wide. The width of the pulse from each cell detected by the PMT was the time it took for each cell to travel through a distance of 32 μm near the T junction. The widths of these pulses were averaged from about 150 cells. The velocity was calculated from dividing the length of the detection region by the average pulse width.

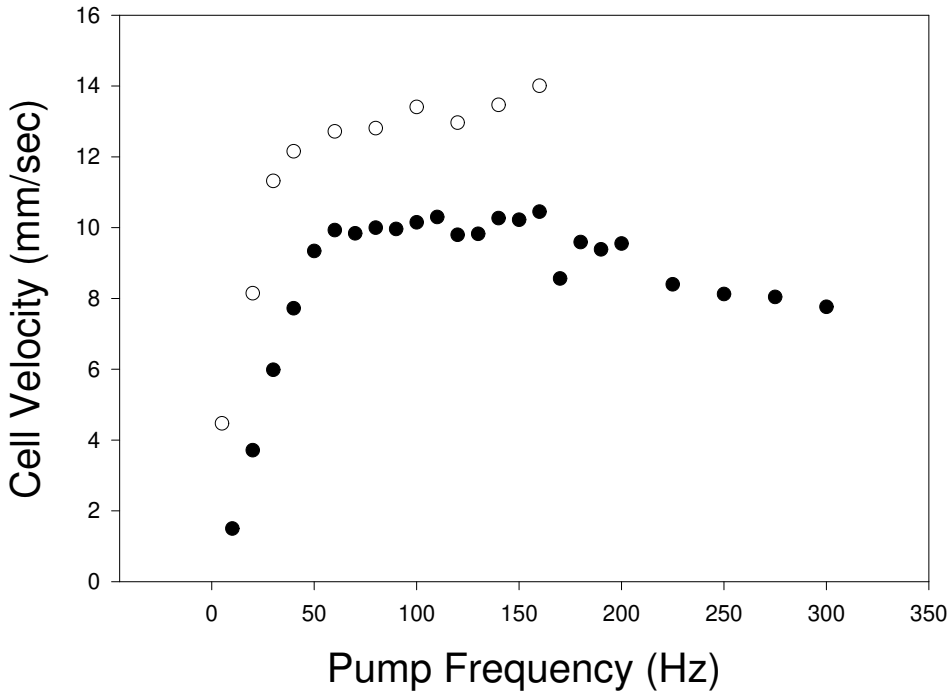

Figure 3.8: A linear flow velocity profile from the integrated cell sorter. The velocity of the cells increased as the frequency of peristaltic pumping increased, reaching to a maximum value at a certain frequency. (•) are the flow velocities recorded using an GE RTV 615 cell sorter with 30% SF-96 , whereas (○) are the flow velocities from a Sylgard 184 cell sorter. Nitrogen pressure applied to the peristaltic pumps was 60 kPa at each frequency. Each value of the flow velocities is the mean velocity of measurements taken from 150 cells. Some data points were taken on separate days from the same devices.

Cells through the cell sorters attained a maximum linear velocity at a pumping rate of 50 Hz (Figure 3.8). Above this frequency, I started to observe incomplete opening and closing of the valves with each pumping cycle. In two separate devices, one made of GE RTV 615 and another made of Dow Corning Sylgard 184, the values of maximum flow velocity are different. The RTV cell sorter has a maximum flow velocity of 10 mm/sec while the Sylgard cell sorter has a maximum of 14 mm/sec. From several measurements done on different cell sorters (unpublished data), I have observed different maximum flow velocities ranging from 6 mm/sec to 17.5 mm/sec. This suggests that I may be able to change the maximum flow velocities of the cell sorters by altering the properties of the elastomer. Adding diluents or mixing different ratios of A and B component of the fluidic layer should allow us to fine-tune the stiffness of the valve membrane, which will affect the minimum closing pressure and the maximum pumping frequency. Changing the dimensions of the fluidic channel will also allow us to tune the flow velocity since different volumes will be moved with each actuation.

I have also demonstrated a different method of interrogation: trapping a single cell within a region of detection. In Chapter 2, I introduced a novel sorting scheme using the electrokinetic sorter called reverse sorting. This reverse sorting of cells is designed to overcome the intrinsic switching speed of the device, which in turn will increase the throughput rate when sorting rare events. To further the concept of reverse sorting, I devised another algorithm of interrogation by trapping cells within the detection region. A computer algorithm is written so that each time the sorter detects a fluorescent cell, it will reverse the direction of peristaltic pumping. Eventually, the cell falls out of the trapping region and flows into the output wells. Figure 3.9 shows the raw data recorded by the oscilloscope on the pattern of cell trapping. At 10 Hz pumping frequency, a single cell was redirected into the detection region more than 10 times before it fell out of the trap. At a higher pumping frequency of 75 Hz, multiple cell trapping instances were recorded. I have also taken measurements of the mean reverse time for each pumping frequency. In Figure 3.10, the mean reverse time was taken to be the time the cell travelled away from the detection region between the

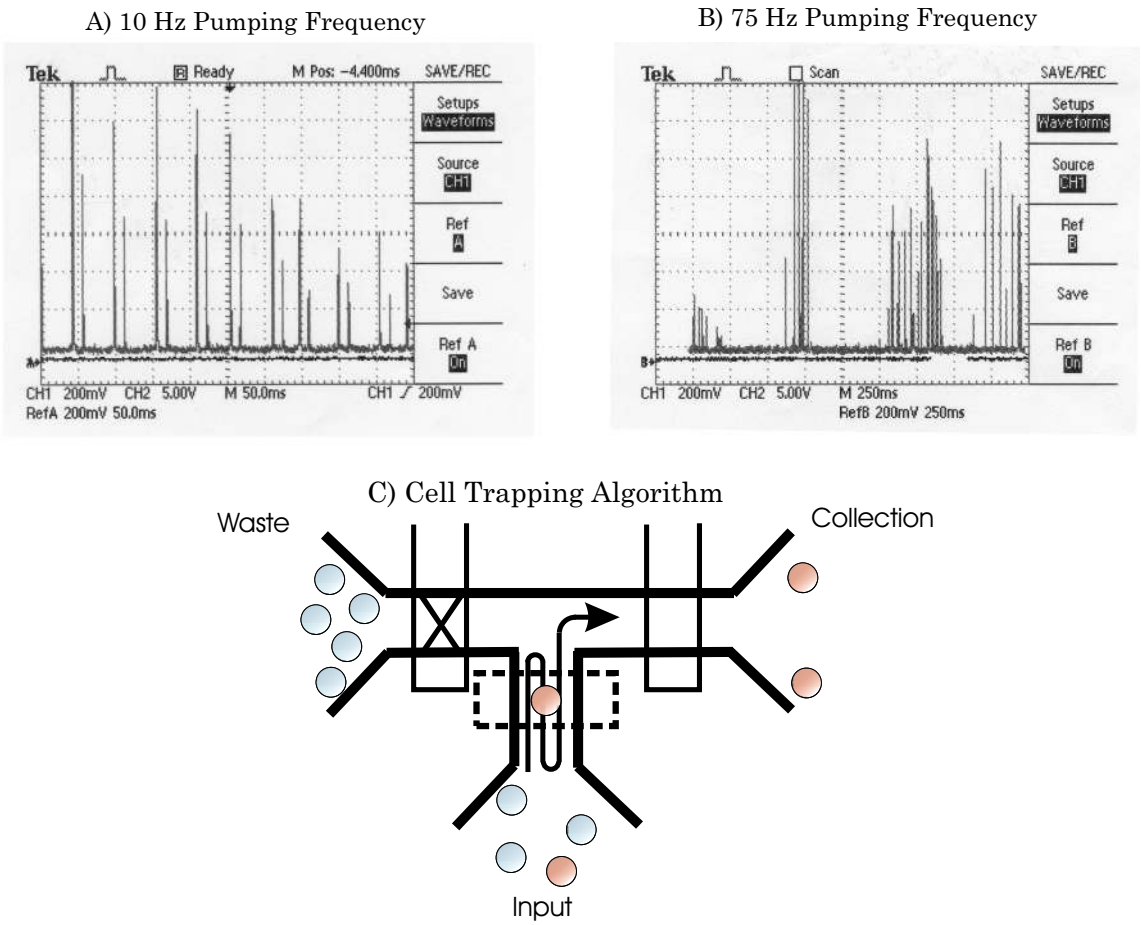

Figure 3.9: Cell trapping. A) Raw data recorded from oscilloscope. One cell was trapped within the region of detection by reversing its direction each time it was detected. The difference in the periodicity between each detection may be due to the variation in the distances the cell travelled away from the detection region before it reverted back. The frequency of the peristaltic pumps was at 10 Hz and the nitrogen pressure applied to the valves was at 60 kPa. B) Raw data recorded at 75 Hz pumping frequency. Multiple instances of cells trapping were recorded. C) A schematic of the cell trapping algorithm. A cell can be trapped within the detection region by reversing the flow at each detection. Cell trapping scheme is as follows. A series of 0 and 1 patterns were used to digitally control individual valves on the chip, where 0 and 1 indicate "valve open" and "valve close," respectively. Forward peristalsis was actuated by the pattern 001, 011, 010, 110, 100, 101, whereas reverse peristaltic was actuated by the pattern 101, 110, 110, 010, 011, 001. These two peristalsis patterns alternate each time a cell's fluorescence reaches above a preset threshold. Detection region is indicated by the dashed box.

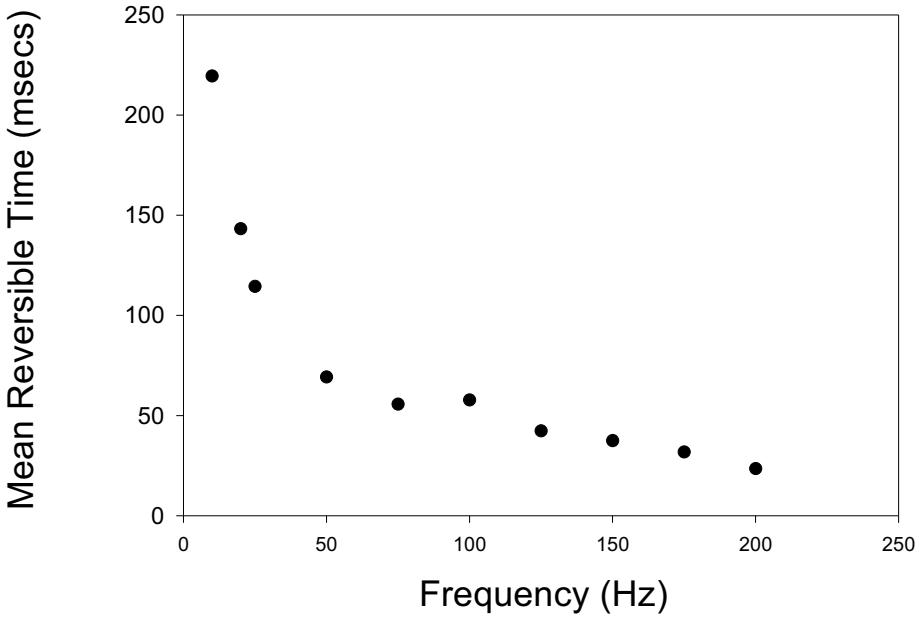

Figure 3.10: Mean reverse time as a function of the pumping frequency. This is the average time for the cells to flow back into the detection region after reversing the direction of the peristaltic pumping. The reverse time gradually decreases as the pumping frequency increases. I used these data as a reference in order to calculate the timing for the reverse sorting. The reverse peristaltic pumping pattern was the peristaltic pumping pattern in reverse exactly. Nitrogen pressure applied to the peristaltic pumps was at 60 kPa at each frequency.

first detection and the second detection when the flow direction is reversed. This was measured as the time between the first and the second pulses read by the PMT. The mean reverse time gradually decreases as the pumping frequency increases. This is consistent with the fact that incomplete opening and closing of the valves will occur with increasing pumping frequency.

This novel method of trapping cells and other bioparticles within a given region inside the sorter opens up new avenues to perform enzymatic kinetic studies on cells and beads. Multiple time course measurements of the same cell can be taken to follow the kinetics of an enzymatic reaction. Sample dispensing can be done before or after the first interrogation and with each successive detection. Cell sorting can still occur after a certain number of detections. Sorted cells can also be redirected back into the sorting region to be sorted again. This enables a new way to investigate kinetics on a single cell level that cannot be accomplished by commercially available conventional flow cytometers.

3.3 Pre-sorting Data Acquisition and Analysis

A pre-sorting data analysis is usually performed in order to determine the thresholds and parameters for the sorting logistics. In conventional FACS and μFACS, data acquisition is divided into two parts, the hardware and the software. The electronic hardware involving PMTs and their amplifiers was discussed in the Chapter 2. I now discuss how the data were analyzed using software that Hou-pu Chou[47] and I have written.

A LabView Program, LV40, was used to capture signals from the PMTs at 5000 Hz through a data acquisition board (Lab-PC-1200; National Instruments, Austin, TX). This program is able to capture and digitize data from as many as eight different PMTs into eight channels (Figure 3.11).

A C++ Builder program, Pulse Analysis[2], was used to determine the positions, heights and widths of the pulses from the data captured by LV40. Initial baseline

[2]written by Hou-pu Chou

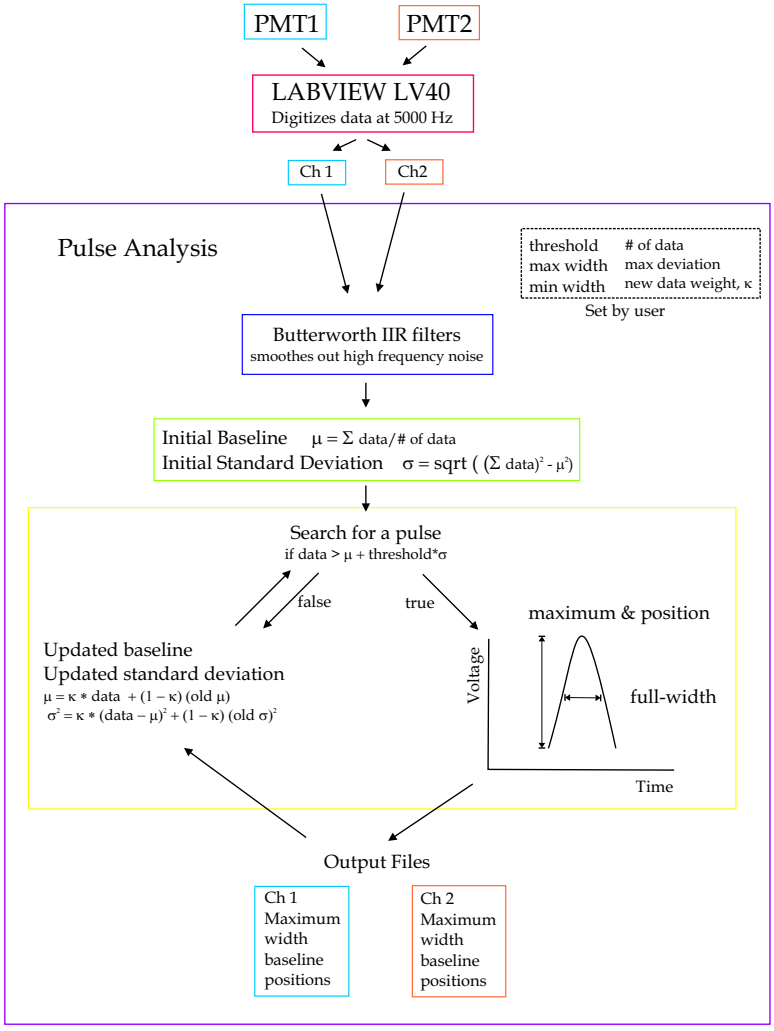

Figure 3.11: Data processing for pre-sorting analysis. See text for details.

μ and its standard deviation σ for each channel was determined by averaging the first 5000 points (preset) from the data. If a data point had a higher voltage signal than $(\mu + threshold * \sigma)$, the sum of the baseline μ and the product of a preset threshold and standard deviation, σ, of the baseline, it was counted as a part of a pulse. The maximum value of the pulse was found by iterative search through the data points. The height of the pulse was then determined by subtracting the maximum data value by μ. The width of the pulse (full width of half maximum) was calculated by subtracting the positions of the data points at the first half maximum and the second half maximum of the pulse. The position of this pulse was then determined at its maximum value (pulse height). In between pulses, μ and σ were

updated as a feedback mechanism due to the decline of the background fluorescence. Such decline may be attributed to photobleaching of channel materials and the other particles adsorbed onto its surface. The new data weight κ was preset to be 0.001. The new μ was calculated as $\mu = \kappa * data + (1 - \kappa) * old\ \mu$ and the new σ, $\sigma^2 = \kappa*(data-\mu)^2+(1-\kappa)(old\ \sigma)^2$. The maximum σ of the baseline should not exceed the value of threshold*σ. A digital Butterworth IIR (infinite impulse response) filter of various orders and frequencies was also designed into this program to smooth out any high frequency noise in the pulse data. But the filter was not used for any cell analysis. The program then output a file for each channel with the height, width, position and baseline of pulses. These output files were then imported into a worksheet program, such as Microsoft Excel or Sigma Plot, to plot histograms of these pulse data and perform statistical analysis.

Another program, Pulse Ratio Analysis[3], was written to further analyze the pulse data from Pulse Analysis. The purpose of this program is to compare the ratios of pulse heights from two or more PMTs. Two pulse data files from two channels were analyzed. The positions of the peaks from one file were first compared to the positions of the peaks from the other file. If the position of one peak lies within the full-width of half maximum of the other peak, or vice versa, these two peaks were counted as signals from the same cell observed simultaneously by the two PMTs and the ratio of their pulse heights was recorded.

The objective of these analyses is to set up sort gates to screen for target cells. In any cell sorting application, a sort gate, or a set of criteria, has to be set in order to capture the target cells. Typical sort gates may include: forward and side light scatter, viability stains and fluorescent stains for target cell functions of interest. For many conventional FACS, a gate can be set up in a twofold way. For example, a cell has to pass a certain forward scatter gating before it can be considered for the fluorescence gating. In Chapters 2 and 3, I used a simple voltage threshold as the criterion for sorting fluorescent from nonfluorescent cells. Although sorting according to ratios of the signals from two PMTs is not presented in this chapter, Chapter 4

[3]Written by Anne Y. Fu

discuss sorting of target cells using ratios of the signals from two PMTs.

3.4 Sorting Logistics for the Integrated Cell Sorter

For the integrated cell sorter, a C++ Builder program, Reversible Digital Pressure-Driven Sorter[4], automates the valves and pumps for reverse sorting. Signals from the PMTs are fed into a data acquisition card (Lab-PC-1200), and a digital I/O card (AT-DIO-32HS; National Instruments) is used for generating patterns of "on's" or "off's" signals for individual valves and pumps on the sorter. The criteria for sorting can be set in two ways: 1) a threshold is set for the fluorescence signals from only one of the PMTs or 2) the threshold is set for the ratios of the signals from both PMTs when one of their signals is above a set voltage. As shown in Figure 3.12, there are essentially five pattern generations: *default*, *first detection*, *second detection*, *third detection* and *end*. The first four patterns, *default*, *first detection* (reverse), *second detection* and *third detection* (both are for recovery), occur in a loop for sorting cells. The user sets up the digital patterns, their respective frequencies and the numbers of times for these patterns to be repeated. The program, upon entering these parameters, allocates memories in the computer as output data buffers for these pattern generations. When sorting starts, the program generates the *default* pattern while reading the signals from the PMTs. Once a desired cell is detected, the *default* pattern is cleared and the reverse pattern is generated. The recovery pattern actually has two pattern generations: *second detection* and *third detection*. When the cell is reversed back into the detection region, this triggers the generation of the *second detection* pattern to send the cell slowly into the collection channel, passing the detection region for the third time. At the third detection, the *third detection* pattern is generated and dictates the time delay of the fluid flow into the collection channel before the *default* pattern is regenerated. If there is no such detection, the *default* pattern is generated at the end of the *second detection* pattern. At the end of the run, an *end* pattern is generated to close all the valves and pumps for cell

[4]Written by Anne Y. Fu and Hou-Pu Chou

retrieval.

3.5 Sorting and Recovery

Sorting in this integrated cell sorter can be done in a variety of ways. Since each valve can be individually controlled in a coordinated and timely fashion, the pumping rate and the valve switching rate can be changed at any time in the course of a sorting event. As mentioned in Chapter 2, there can be both forward and reverse sorting within this microfluidic sorter. However, to overcome the limitation of the switching speed which is delayed by the intrinsic valve response time, a reverse sorting scheme was used to sort cells in this integrated pneumatic-driven sorter.

The reverse sorting algorithm for the valves and pumps is as follows. Three patterns are generated for a sorting event: default pattern, reverse pattern and recovery pattern. The default pattern pumps the cells into the waste channel at 100 Hz with 60 kPa valve pressure. Once a desired cell is detected, the reverse pumping pattern is generated at 10 Hz pumping frequency to bring the cells slowly back into the detection region to be detected once more. If there is no detection of any desired cell, the flow will reverse until the end of the reverse pattern and then generate the default pattern again. However, if the desired cell is detected again, the recovery pattern will be generated. This pattern will first close all the valves to stop any fluid flow. Then with the waste valve remains closed, the collection valve is opened and the pump sends the detected cell slowly into the opened collection channel, pumping at 10 Hz for a selected number of cycles. Following this pattern, the default pattern starts again until the next sorting event.

In a typical run, I separated two populations of *E. coli* cells, one expressing EGFP and the other expressing para-nitrobenzyl (pNB) esterase. The EGFP cells generate a fluorescence signal on the PMT, which triggers collection. The populations were mixed in a ratio of 1:2000 and introduced into the sorter first by nitrogen back pressure and then by peristaltic pumping when sorting began. After 3 hours, the cells at the collection and waste wells were retrieved using a pipetman into two microcentrifuge

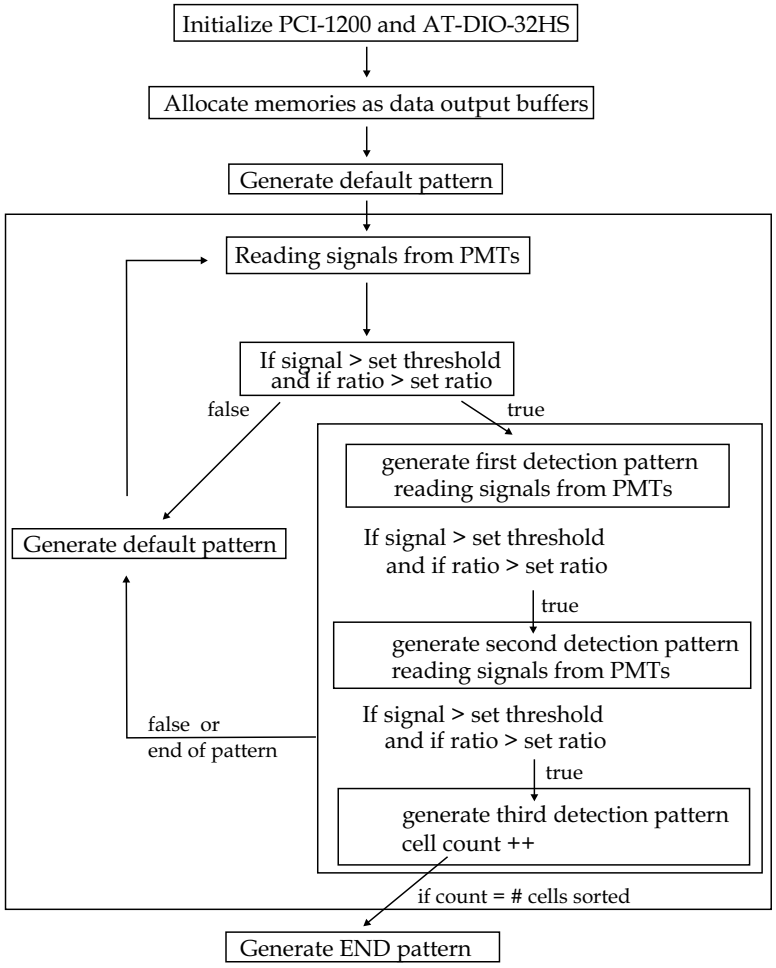

Figure 3.12: Sorting logic for reverse sorting. Reverse cell sorting scheme is as follows. With valve 4 as the collection valve, the default flow from the input to the waste was actuated by the pattern 01001, 01011, 01010, 01110, 01100, 01101 at 100 Hz. Once a target cell was detected, the reverse flow was actuated by the pattern 01101, 01100, 01110, 01101, 01011, 01001 at 10 Hz to slowly bring the cell back to the input channel. Once the cell passes the detection region again, all the valves were closed to stop the flow, 11111, and then the recovery of the cell was actuated by the pattern 10001, 10011, 10010, 10110, 10100, 10101 at 10 Hz to close the waste valve and direct the cell into the collection channel. The default flow was actuated again once the cell was in the collection channel. A pattern of 11111 was actuated at the end of the run to close all the valves for cell retrieval.

tubes. The contents of each microcentrifuge tube were then divided and spread out on two different antibiotic plates, ampicillin (amp) and tetracycline (tet). Since EGFP expressing cells grow only on amp plates and the pNB esterase expressing cells grow only on tet plates, the fraction of these two cells in each well can be easily counted on the different antibiotic plates. The plates were placed in a 37° C incubator overnight and the colonies were counted. The sorting results are shown in Table 3.5. In the longest run, about 480,000 cells were sorted in 3 hours at a rate of 44 cells/sec. The recovery yield is 40% in this run and the enrichment ratio is about 83 fold. The enrichment ratio is calculated as the ratio of the fraction of EGFP in the collection well to the fraction of EGFP in the original mixture at the input well. Results of various single runs are summarized in Table 3.5. We were able to obtain up to 50% recovery, with as high as 90-fold enrichment. A throughput rate of 100,000 cells per hour has also been achieved.

The integrated sorter can run without interruption for 5 hours or more, and can be used numerous times after proper cleaning. One device was used for 6 months continuously with tens of millions of actuations on each valve and pump. Compared with our previous electrokinetic sorter[26], this integrated sorter alleviates many issues regarding buffer compatibility, surface chemistry and cell viability. Different strains of *E. coli* cells and different types of bacteria, including magnetotactic bacteria, could be pumped in their own suspending media through the integrated cell sorter. By incorporating valves and pumps to control sorting by pneumatic actuation, the integrated sorter has a better capability of fine-tuning the flow and is less harmful to the cells than electrokinetic flow. Thus, although the throughput rate was increased only twofold, the recovery yield and the accuracy of sorting improved tremendously. Under the observation of the microscope, we were able to capture most or all of the desired cells into the collection channel even when they occurred in small numbers. Since we are only recovering most of the cells at the wells, we believe that we will be able to reach close to 100% recovery in future devices by incorporating a flushing mechanism to retrieve the remaining cells that are inside the collection channel.

The variability in the results of different runs in Table 3.5 can be attributed to

factors such as initial cell concentration, fraction of EGFP-expressing bacteria at the input, time duration of each run, retrieval using pipetmen and device fabrication. Interestingly, two of the sorting runs were done on the same device, 110300IIIRTV. Using the same sorting parameters (actuation patterns, preset threshold, time duration and retrieval) except for initial cell concentration and fraction of EGFP-expressing bacteria at the input, these two runs resulted in different enrichment ratios, throughputs and recovery yields. The latter run has obtained a throughput of 177,000 cells in two hours, which is slightly more than twice that of the former run, which had a throughput of 79,000 in two hours. The enrichment for the latter run, 80-fold, is also slightly more than twice that of the former run, 35-fold. Similar trends can also be observed with the results obtained from the two runs done on the 110300IISYL device. These results lead us to conclude that the fraction of EGFP-expressing cells at the input is a critical determining factor in using reverse sorting algorithm. When sorting with rare events, higher throughput and enrichment could be achieved if these events occur at a much lower frequency since the sorter can then be operated at a high speed most of the time. The initial cell concentration is also an important factor for increasing throughput and recovery. As shown from the results of the devices, 110300IIIRTV and 110300IISYL, the recovery yields from these devices greatly depend on the number of cells sorted to the collection well. Higher recovery can be achieved if more cells are sorted to the collection well.

The integrated cell sorter offers several advantages over the conventional FACS machines. Because the channels in the device are of micron dimensions, the volume of interrogation can be precisely controlled to reduce any background fluorescence from the media and channel materials. The planar configuration of these devices allows the use of high numerical aperture optics, increasing the sensitivity of the whole system[65, 26]. Due to easy fabrication process and inexpensive materials, these devices can be disposable to eliminate any cross-contamination from previous runs. In addition, the whole cell sorting system is self-contained, unlike the conventional aerosol droplet sorters, allowing for relatively safe sorting of biohazardous materials. Although conventional FACS machines still achieve higher throughput, recovery and

Device Number	Cells/mL	EGFP Fractions			Time	Cells/sec	Cells sorted	Recovery	Enrichment
		Input	Collection	Waste					
042800RTV	2.8×10^{7}	4.0×10^{-2}	2.8×10^{-1}	1.8×10^{-2}	2 hours	1.3	9,251	48%	6.9
110300IIIRTV	6.3×10^{7}	5.7×10^{-3}	2.0×10^{-1}	4.9×10^{-3}	2 hours	11	79,200	50%	35
110300IIIRTV	2.8×10^{7}	1.1×10^{-3}	9.5×10^{-2}	3.1×10^{-3}	2 hours	26.4	177,333	21%	89
110300IRTV	9.7×10^{7}	2.5×10^{-3}	1.1×10^{-1}	7.7×10^{-4}	3 hours	6	40,922	16%	43
110300IISYL	2.6×10^{7}	2.7×10^{-2}	3.4×10^{-1}	1.5×10^{-2}	2 hours	2.16	15,600	26%	13
110300IISYL	1.3×10^{8}	4.4×10^{-4}	3.6×10^{-2}	8.0×10^{-4}	3 hours	44	479,381	39%	83

Table 3.5: Results of sorting and recovery of *E. coli* cells using 4 different cell sorters. Device numbers that end with the characters "RTV" are made from GE RTV 615 and device numbers that end with the characters "SYL" are made from Sylgard 184. Cell concentrations at the input well are indicated. Fractions of EGFP at the input, collection and waste wells are also presented. Recovery was calculated as the percentage of the actual number of EGFP recovered at the collection well divided by the number of positive fluorescent events detected by the device. The enrichment was calculated as the ratio of the fractions of EGFP at the input to the collection wells. The reverse sorting algorithm was used for all runs. The yield can be affected by a number of factors, such as the accuracy of sorting, the number of false positives, the viability of the cells and the methods used for retrieval. The total number of cells sorted can also be calculated in two ways: 1) from the linear flow velocity of the cells, the concentration of the cells at the input well and the time duration of the run, or 2) the number of cells whose fluorescence triggered sorting and the fraction of fluorescent cells at the input well. However, due to the variability of the linear flow velocity, the second method was preferred for calculating the total number of cells sorted. The cell sorting speed can then be derived from the total number of cells sorted and the time duration of each run.

accuracy of sorting, the integrated cell sorter serves as an alternative to an inexpensive, robust and easy way for sorting or manipulating single cells. Multiplexing the cell sorting channels can increase the overall throughput and allow for simultaneous measurements of cells in different compartments. Innovative sorting schemes can be implemented on the device to perform time-course measurements on a single cell for kinetic studies, which cannot be done by any conventional FACS. Sample dispensing and other chemical or enzymatic reactions, such as cell lysis and/or polymerase chain reaction, can also be carried out downstream immediately after the cell has been sorted[21, 22]. For future work, we plan to use this sorter to accomplish high throughput screening of *E. coli* cells in directed evolution[66]. Moreover, a device of similar design has already been fabricated for sorting mammalian cells and other cell types by Fluidigm, Inc., South San Franciso, CA.

3.6 Conclusion

I have developed an integrated microfabricated cell sorter using multilayer soft lithography. This integrated cell sorter is incorporated with various microfluidic functionalities, such as peristaltic pumps, dampers, switch valves, input and output wells, to perform cell sorting in a coordinated and automated fashion. The active volume of an actuated valve on this integrated cell sorter can be as small as 1 picoliter and the volume of optical interrogation is approximately 100 femtoliters. The linear flow velocity on the sorter is 14 mm/sec, which can be tuned by altering the pumping frequency and its elasticity. Novel algorithms of cell manipulation, including reverse sorting and cell trapping, were all performed. I have also demonstrated sorting and recovery of *Escherichia coli* cells on the chip.

Unlike the conventional aerosol flow cytometers, the integrated cell sorter allows for flexibility in designing different ways of sample dispensing and methods of interrogation. This will enable single cell studies to be achieved in a more precise and automated fashion. In addition, due to the easy fabrication process and inexpensive

materials used in multilayer soft lithography, the integrated cell sorter can be disposable to avoid any cross-contamination between runs. I am presently using this sorter as a stand-alone device for molecular evolution and other biological applications. More fluidic functionalities, such as rotary pumps and incubation, can be integrated in the future. We anticipate that an integrated "lab on a chip" where cell sorting is just the first step of a complete analysis system is not far off.

Future developments of the sorter may expand into various aspects. In terms of optics, the sorter can include other optical signals such as light scatter and absorbance measurements. There are also ways for the sorter to measure magnetic and electrical signals. We have demonstrated the feasibility of the sorter to detect and sort magnetotactic bacterial cells in Chapter 6. Others also have demonstrated cytometric capacitance measurements on cells in microfluidic devices[67]. These technologies can all be incorporated into the sorter to make simultaneous measurements of multiple parameters of single cells. In the near future, with the advances of electronics and optics, these sorters could be made into hand-held machines to be readily used in clinics, hospitals, environmental field testing and biological weapon detection.

Chapter 4
High Throughput Screening of GFP Variants Using μFACS

4.1 Introduction

Directed evolution, inspired by Darwin's theory of evolution, is a laboratory technique for protein evolution[68]. The effectiveness of evolution as a powerful algorithm to explore enzyme functions and to create new functions depends on the success of two processes: 1) the ability to rapidly generate diversity at the molecular level and 2) the ability to rapidly identify the variants of desired properties (or the fittest-among-survivors). Many techniques have been well established to create genetic diversity through random mutagenesis and/or recombination methods, such as error-prone PCR[69], DNA shuffling[70, 71] and staggered extension process[72]. However, there has been a huge lag in devising tools to perform rapid, high throughput screening to select out the desired mutants.

We have previously demonstrated the capability of μFACS to efficiently sort fluorescent cells from their nonfluorescent counterparts and achieve substantial enrichment and recovery. In addition, novel sorting schemes can be implemented in μFACS to carry out kinetics measurements and other single cell manipulation. In this study, we set out to prove that μFACS is an effective high throughput screening tool for directed evolution and other synthetic combinatorial libraries. As an example, we isolated mutants of green fluorescent protein with changes in their emission spectra using μFACS.

The green fluorescent protein (GFP) from the luminescent jellyfish *Aequorea victoria* has become an excellent marker for gene expression and protein localization

in intact cells and organisms[73]. Its ability to form a highly efficient fluorophore without any cofactors makes GFP an interesting research topic as well as a versatile tool to study a variety of biological systems[74, 75]. GFP is an 11-stranded β barrel threaded by an α-helix running along the axis of the cylinder[76, 77]. The chromophore, a *p*-hydrooxybenzylideneimidazolinone formed from residues 65–68 (Ser-Tyr-Gly), is attached to the α-helix and is buried in the center of the barrel[73]. GFP absorbs light with an excitation maximum at 395 nm and a minor peak at 470 nm; it fluoresces with an emission maximum at 508 nm (Figure 4.1).

Re-engineering GFP by mutagenesis has improved several of its properties, such as increased fluorescence brightness, expression level, folding stability and the rate of chromophore formation[76, 71, 6]. New GFP variants with altered excitation and emission maxima have been extremely useful for simultaneous measurements of multiple gene expression levels and protein activities[78]. The most red-shifted GFP variant known has an emission maximum of 529 nm in the yellow-green region[73]. A more red-shifted GFP variant is thus desirable for many applications. Since most cells are translucent to far-red light, the autofluorescence of the cells would be reduced, increasing the signal-to-noise ratio. In addition, a more red-shifted variant may have less spectral overlap with other GFP variants, which is ideal for multi-color labeling.

After this work began, a red fluorescent protein, DsRed, was discovered in coral reef by Matz and his colleagues[79]. The DsRed protein is only 28% homologous to GFP and is prone to tetramerization when fully matured[80, 81]. These properties limit the use of DsRed protein in conjunction with other GFP variants in certain applications that require the same protein synthesis and decay rates[28].

Using μFACS, our goal was to screen for GFP mutants with red-shifted emission maxima through the directed evolution approach. We generated libraries of GFP mutants using error-prone PCR and screened for mutants with changes in their emission spectrum (Figure 4.2). In two hours, we screened approximately 64,000 mutants and recovered the selected ones from the device. These results demonstrated that μFACS is a powerful, robust and effective tool to perform high throughput screening in fields such as directed evolution and synthetic combinatorial libraries.

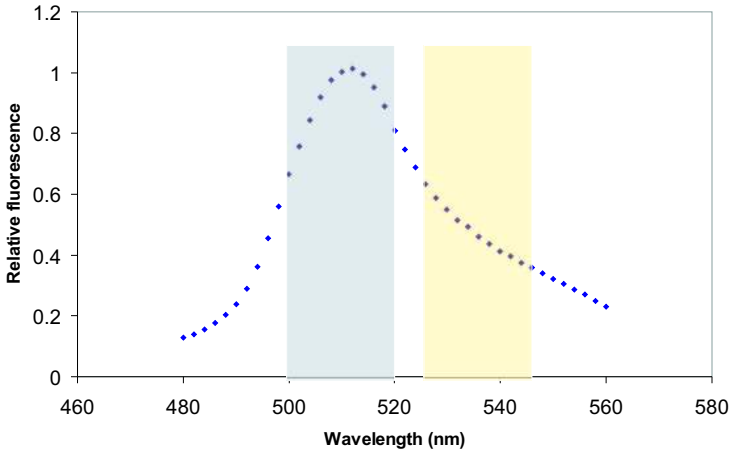

Figure 4.1: Fluorescence emission spectrum of GFP. Two PMTs were used to detect two spectral regions of wild-type GFP fluorescence, 510 nm ± 10nm and 535 nm ± 10 nm. The ratios of the signals from these regions were used as a screen to select for any red-shifted mutants.

4.2 Results and Discussion

Wild-type GFP was subjected to error-prone PCR for random mutagenesis. Two different concentrations of $MnCl_2$, 0.3 mM and 0.5 mM, were used in the PCR mixture to produce two mutant libraries of different mutation frequency (the average number of mutations per gene). GFP and its variants were expressed in plasmid pGFP (Clontech) and cloned in *E. coli*. As indicated by Figure 4.2, a hypothetical mutant with a red-shifted emission maximum is expected to have a higher ratio of 535 nm to 510 nm in the emission spectrum. A screen, using two PMTs to observe fluorescence emission in these two spectral regions, 510 nm ± 10nm and 535 nm ± 10 nm, was thus set up to search for mutants with higher ratios of 535 to 510 nm.

4.2.1 Distributions of GFP mutant libraries

We first investigated the effect of error-prone PCR on the emission spectra of the GFP mutant libraries. The change in the ratio of these two wavelengths, 510 nm to 535 nm, in the fluorescence emission could be caused by 1) a shift in the maximum wavelength of the emission spectrum, 2) a change in the emission bandwidth and/or

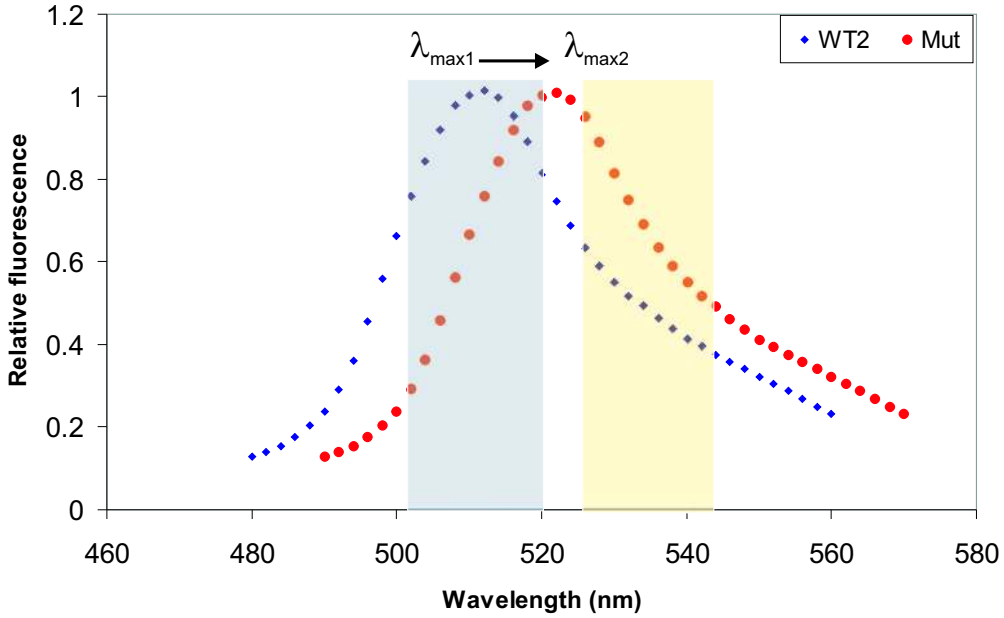

Figure 4.2: Emission spectra of wild-type GFP and a hypothetical red-shifted variant. The fluorescence emission of this variant is expected to have a higher ratio of 535/510 nm than that of wild-type GFP. A screening method was set up to search for mutants with higher 535/510 nm ratios.

3) a change in the fluorescence intensity of GFP. Mutations that can induce these kinds of changes in GFP fluorescence emission would be detected by the screen set up in μFACS. Three different populations of GFP and its variants, 0.3 $MnCl_2$ mM mutant library, 0.5 mM $MnCl_2$ mutant library and wild-type GFP, were introduced into the sorter for cytometric analysis.

Figure 4.3 shows the distributions of the ratios of 510/535 nm emission of these three different populations. The means for the ratios of all three populations were approximately equal, $\sim$1.4, although the standard deviation for each library was different (see Table 4.1). Comparing the colonies of 0.3 mM and 0.5 mM $MnCl_2$ libraries on agar plates, approximately 15% of the 0.3 mM $MnCl_2$ library population were actually fluorescent whereas only 11% of 0.5 mM $MnCl_2$ library were fluorescent.

These results indicate that higher mutation rate had resulted in more deleterious mutations that led to total loss of fluorescence for 90% of GFP mutants in the 0.5 mM $MnCl_2$ library. Thus in using error-prone PCR to carry out random mutagenesis,

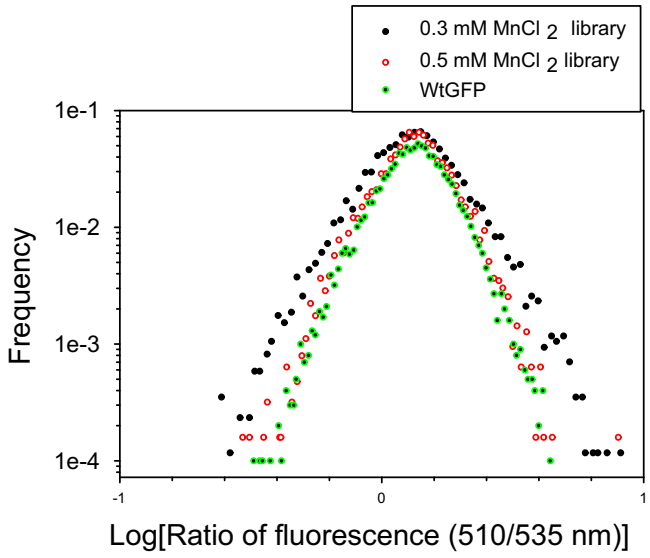

(A) Original Data

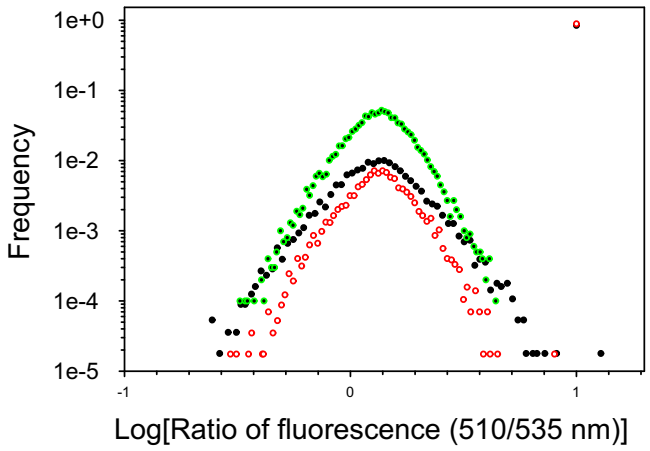

(B) Normalized Data

Figure 4.3: The distributions of the ratios of 510nm/535nm in the GFP emission spectra for wild-type and GFP mutant libraries in the log scale. (A) represents the distributions where the normalized counts of the original data do not include non-fluorescent mutants. (B) represents the corrected distributions where the normalized counts includes the nonfluorescent cells. The total numbers of cells (including the nonfluorescent cells) scanned for each were 10,000 cells for wild-type GFP and 57,000 cells for both 0.3 mM $MnCl_2$ and 0.5 mM $MnCl_2$ libraries.

Library	Ratio mean	Standard dev.	C.V.	Cells scanned
Wild-type	1.40	0.44	31%	10,000
0.3 mM $MnCl_2$	1.43	0.64	45%	8530
0.5 mM $MnCl_2$	1.40	0.47	33%	6284

Table 4.1: Data analysis of GFP libraries. These are the means and standard deviations for the ratios of 510nm/535nm in GFP emission for different GFP libraries.

the mutation rate must be precisely controlled such that beneficial mutations can be screened[82, 83]. Higher mutation rate yields more clones with total loss of fluorescence, while lower mutation results in too many parent-like clones[82]. As the graphs in Figure 4.3 show, while most of the population in 0.5 mM $MnCl_2$ library were not fluorescent, the ones that did fluoresce resembled wild-type GFP distribution. Yet, the fluorescent cells from the 0.3 mM $MnCl_2$ library have a broader ratio distribution than both the 0.5 mM $MnCl_2$ library and the wild-type library. Hence, we set out to screen for red-shift mutants from the the 0.3 mM $MnCl_2$ library. The distribution of the 0.3 mM $MnCl_2$ library suggested that approximately 0.2% of GFP variants in this population have ratios of 535/510 nm greater than 2.0 in their fluorescence emission. These ones could be mutants with their emission maxima red-shifted as shown in Figure 4.2. The 535/510 nm ratio of 2.0 was then used as one of the sort gates for screening mutants with red-shifted emission maxima.

4.2.2 Screening for Red-shifted Mutants

Using the μFACS system, the 0.3 mM $MnCl_2$ library was screened for variants with red-shifted emission maxima using a sort gate set at the ratio of 535/510 nm fluorescence emission of 2.0 and a voltage threshold of 0.2 V. The voltage threshold was used to avoid any false positives from the high frequency noise (spikes) of the PMTs that could result in very high ratio values. Hence any mutants whose fluorescence intensity read by the PMTs to be higher than 0.2 V and the ratio of 535/510 nm in their emission spectra greater 2.0 would be sorted and collected. One advantage of using ratios of wavelengths as a screen is that it normalizes the size distribution of

the bacterial cells as well as the differences in the expression level and the number of plasmids. After two hours of screening, nearly 64,500 cells were analyzed and sorted. There were 129 mutant GFP cells that triggered sorting events. Approximately 800 cells were retrieved from the collection well and regrown on an agar plate of LB with ampicillin. Using the reverse sorting algorithm, the population of target cells was enriched (as opposed to being purified). In other words, when μFACS encounters coincident events, it collects both the target and unwanted cells. Thus the number of cells retrieved from the collection well was higher than the number of actual positive events triggered.

4.2.3 Results and Analysis of Sorted Mutants

Post-sorting analysis of the 0.3 mM $MnCl_2$ mutant GFP library has some complications. Although the 800 cells were retrieved from the collection well and regrown on an agar plate, there was no accurate method to calculate for the enrichment and recovery yield. Nearly 384 colonies were picked from the 800 colonies retrieved and placed in 96-well plates with LB and ampicillin. A standard 96-well plate fluorimeter was used to observe fluorescence from the crude cell lysates. No mutant was found to have a red-shifted emission maximum. Most of the signals triggered for sorting were from cells whose fluorescence intensity were so low that there appeared to be a broad emission bandwidth. These cells were either in the early log phase such that the level of GFP expression is low or have mutations which cause a decrease in GFP fluorescence.

All the GFP red-shifted variants known are more than two or three mutations away[73]. In our experiment, we have screened ~64,000 mutants. Yet, a GFP library with double mutants (variants with two amino acid substitutions) would have approximately 8 x 10^6 mutants. Due to the fact that the distribution of mutations generated by existing random mutagenesis techniques follows a Poisson distribution[68], the number of mutants to be screened has to be at least three times the size of the library[84]. These numbers are beyond the limitations of most conventional FACS and μFACS.

It is conceivable that there could be some red-shifted variants that are only one mutation away from the wild-type sequence. However, due to the inherent biases in mutations generated by error-prone PCR and other mutagenic methods[68], we may not be able to create and screen for all the possible single and/or double mutants.

Since the vast protein space cannot be completely searched by the existing screening tools available to us, and most mutations are deleterious or neutral[68], higher mutation rates (with more than three amino acid mutations per gene) may not help us to arrive at the desired solutions. Novel, rapid and robust screening tools are thus needed. Conventional FACS, μFACS and other high throughput screening techniques[66] are just beginning to allow the exploration of the vast protein space to expand. Future developments in these tools would push directed evolution to new frontiers of protein engineering[5].

4.3 Conclusion

In this chapter, I have presented μFACS as a simple, robust and effective tool to perform high throughput screening for GFP variants. Using error-prone PCR to perform random mutagenesis, we have screened 64,000 GFP variants in just two hours. Although most of the clones that we selected were either in early log phase or weakly fluorescent, we have demonstrated that we were able to set up a sort gate and screen for mutants that meet the criteria. The present limitations in directed evolution lie not in the ability to create libraries of mutants, but in the tools that are available to us to exhaustively search for the mutants with desired properties[85]. Our μFACS system has proven to be an inexpensive and powerful tool to perform high throughput screening to meet such a demand.

4.4 Materials and Methods

4.4.1 Random Mutagenesis

Error-prone PCR was carried out to perform random mutagenesis. Primers 5'-CCGACTGGAAAGCGGGCAGTG-3' and 5'-CCGCATAGTTAAGCCAGCCCCG-3' were used. The mutagenic PCR reaction mixture contained 50 mM KCl, 10 mM Tris-HCl (pH 9.0 at 25° C), 0.1% Triton©X-100, 0.2 mM dGTP, 0.2 mM dATP, 1.2 mM dCTP, 1.2 mM dTTP, 7 mM $MgCl_2$, 2 pmol of each primer, ∼0.1 μg of pGFP, 0.3 or 0.5 mM $MnCl_2$, 1 U of *Taq* polymerase in a total volume of 100 μl. PCR reactions were carried out on a MJ Research thermal cycler (Watertown, MA) for 25 cycles: 98° C, 1 min, 48° C, 1 min, 72° C, 2 min. The PCR product was gel-purified and digested with BamH1 and EcoR1 in 1X EcoR1 buffer at 37° C for 4 hours. The digested product was cloned back into the expression vector for transformation into DH5α *E. coli* cells. After transformation, the cells were diluted 1:10 into LB media with ampicillin. After growing at 30° C for 24 hours, these cells were introduced into the sorter for screening.

4.4.2 μFACS Setup

An integrated cell sorter was mounted on an inverted Zeiss microscope. An Argon laser (488 nm) was used as an excitation source. The emitted fluorescence from the cells was collected by the objective (100X, 1.3 N.A. oil, Olympus), split by a dichroic 520LP (Chroma) into two PMTs with filters 510DF20 and 535DF20. A sort gate was set at a voltage threshold of 0.2 V and the ratios of greater than 2.0 for the wavelengths of 535 nm and 510 nm of the GFP emission spectra. Reverse sorting algorithm was used. After sorting, cells at the collection well were retrieved by a pipetman and spread onto a LB+amp agar plate.

4.4.3 Fluorescence Assay in 96-well Plates

Nearly 384 colonies were hand-picked by toothpicks from the 800 colonies retrieved into four 96-well plates. After growing at 30° C in LB+amp for 24 hours, these colonies were centrifuged at 5000 RPM and lysed with Bugbuster (Promega).

Chapter 5
Digital Genetic Circuits

5.1 Introduction

Genetic networks contain thousands of molecules interacting in various metabolic pathways in order for a cell to maintain proper metabolism. These networks consist of highly branched and interwoven "genetic circuits" that are analogous to complex, interconnected electrical circuits[86]. Recent advances have led to the design of *de novo* genetic circuits inside *E. coli* cells to function as an oscillator[87] and a toggle switch[88]. Moreover, when an autoregulatory, negative feedback loop was added to a *de novo* genetic circuit, the noise or the variability in gene expression was dramatically reduced[89]. These findings grant us not only a deeper insight into the regulatory mechanism of natural genetic networks, but a glimpse of how we can design *de novo* genetic circuits to program a cell or a group of cells to perform computational functions. Weiss *et al.* are laying down a general principle to designing genetic circuits that can implement the digital logic abstraction and thus are capable to program cell behaviors that are complex, predictable and reliable[28].

5.1.1 Digital Logic Abstraction

Digital logic, that is, physical chemical signals being translated to logical true (HIGH) or false (LOW) values, can be engineered inside living cells using simple genetic elements, such as promoters, repressors, operator regions and other DNA-binding proteins. Digital circuits would allow us to reduce the inherent stochastic noise in these circuits and maintain two distinct representations of signal values with high predictability and reliability (Figure 5.1). This also requires the presence of ade-

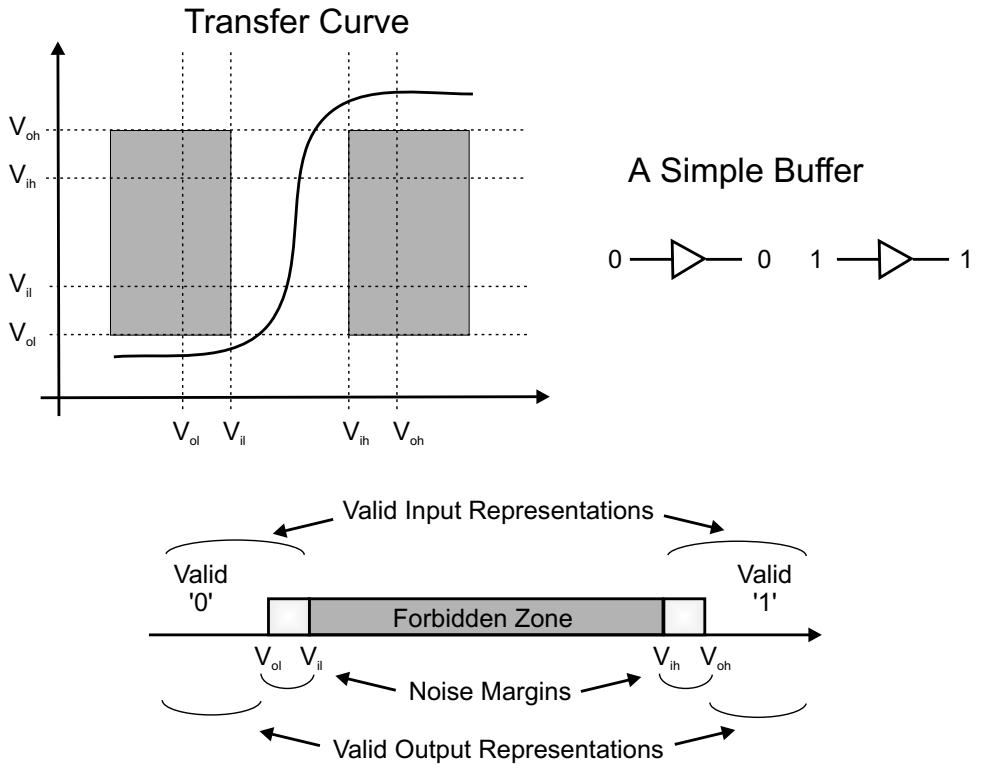

Figure 5.1: Digital logic abstraction. An electrical or chemical signal can be translated into two distinct representations of HIGH and LOW values. A transfer curve of a simple buffer is shown. The buffer outputs 0 if its input is 0 and outputs 1 if its input is 1. This buffer maintains two distinct valid output representations *if and only if* the input representations are valid. The "forbidden zone", where valid inputs result in invalid outputs, is to be avoided. The noise margins, where marginally valid inputs can still result in perfect output representations, are critical for tolerating any noise or loss of signals within the circuit. V_{ol} = LOW output, V_{il} = LOW input, V_{oh} = HIGH output, V_{ih} = HIGH input.[91]

quate noise margins, that is, the ability to produce a valid logical output signal from a physical input representation that is marginally valid or imperfect[90] — a signal restoration. These noise margins are critical for tolerating any noise or loss of signals within the circuit. By measuring the relation between the input and output signals in a steady state, that is, a transfer function, the gain and noise margins of a logic gate or a circuit can be calculated. The "forbidden zone", which corresponds to valid inputs but invalid outputs, can also be mapped. In any circuit design, the gain must be greater than one and be highly nonlinear.

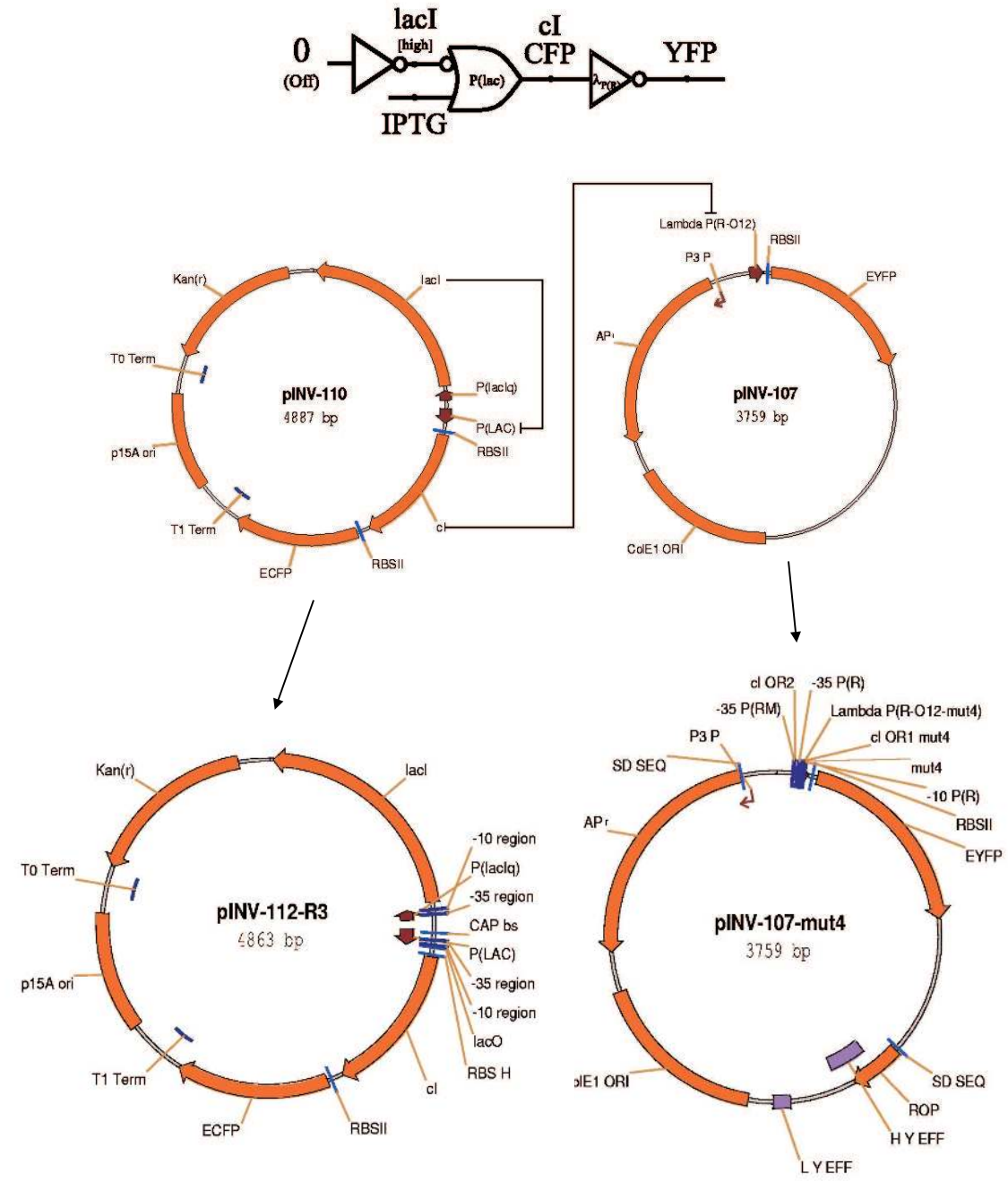

Figure 5.2: The $cI/\lambda_{P(R-O12)}$ genetic inverter designed by Weiss using genetic process engineering. The original circuit, pINV-110 and pINV-107 designed by Weiss, failed to respond to any IPTG induction. This circuit began to behave like an inverter when he engineered a weaker ribosomal binding site for pINV-112-R3 and reduced the repressor/operator affinity on the O_R1 operator region for pINV-107-mut4. (Courtesy of Dr. Ron Weiss)

5.1.2 Matching Gates

There are several differences between electronic digital circuits and genetic digital circuits. Electronic digital circuits are composed of spatially arranged, identical transistors whose HIGH and LOW signal ranges are the same for all the gates. In living cells, since the same logic gate cannot be used twice in a genetic circuit, there has to be a repertoire of various logic gates with corresponding HIGH and LOW ranges in order to design more complex circuits. However, many of these genetic logic gate components (DNA-binding proteins and operator regions) have different characteristics due to their reaction kinetics, such as the binding affinity, the cooperativity of the repressors, the rates of transcription, translation and decay, the stability of mRNA and proteins. Thus additional modification of these gates may be necessary to ensure that these gates would implement digital abstraction, and if they are coupled, the HIGH and LOW signal ranges are matched appropriately[28]. In Weiss' work, a genetic inverter had to be modified in the ribosomal binding site and the repressor operator region in order for it to behave predictably and reliably[28] (See Figure 5.2). In a more complex circuit, Elowitz *et al.* [87] also had to modify their genetic oscillator to have a stronger and tighter transcriptional control and shorter lifetimes of the repressor proteins in order to observe oscillatory behavior. Moreover, these novel genetic gates could be engineered such that they would not interfere with the host mechanism and are optimized in their time-response.

5.1.3 μFACS

Actual biological behaviors of genetic circuits display variations due to stochastic effects and other systematic fluctuations[89, 87, 28]. These circuits are best characterized using flow cytometry to capture such inherent noise on the single cell level. This chapter presents the characterization of a simple genetic inverter, the $cI/\lambda_{P(R-O12)}$ genetic inverter[28]. Using μFACS, Dr. Yohei Yokobayashi and I were able to measure its transfer function and fluctuations. A *transfer band* of the inverter, which encompasses actual biological fluctuations, was also plotted. The predicted behavior

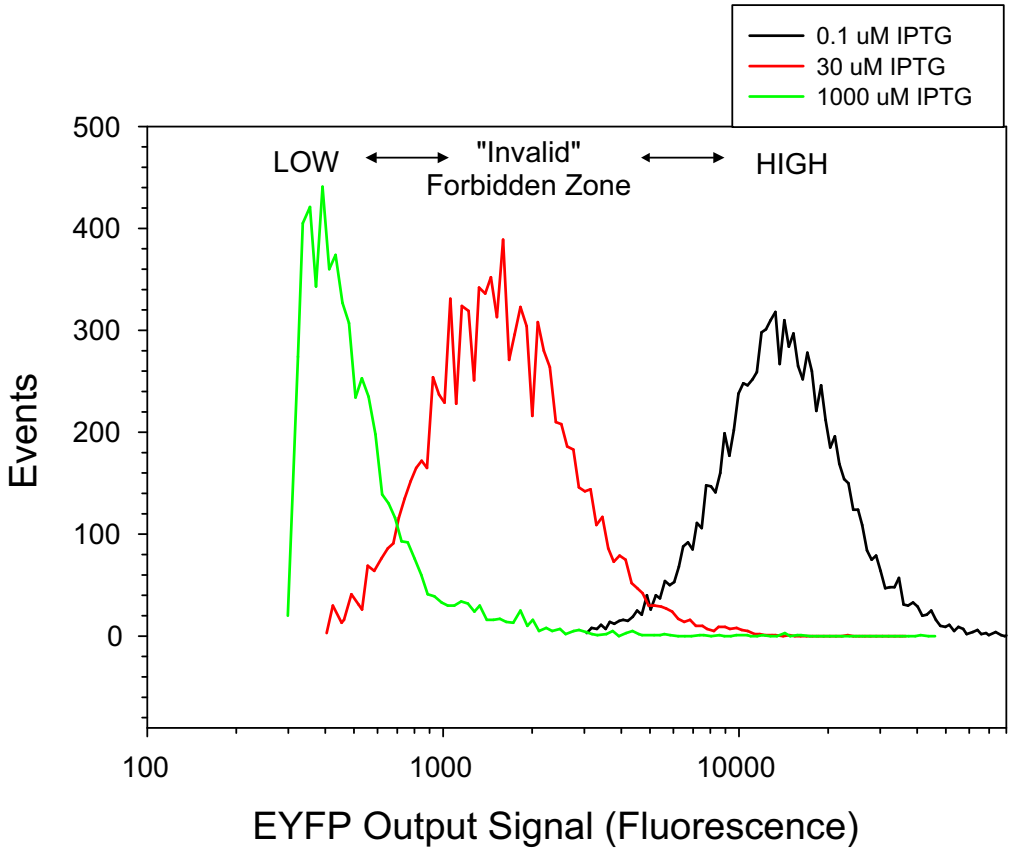

Figure 5.3: Histograms of EYFP output signals. At 1000 μM IPTG, the output of the inverter exhibited LOW EYFP fluorescence. At 0.1 μM IPTG, the output of the inverter exhibited HIGH EYFP fluorescence. At the forbidden zone of 30 μM IPTG, the EYFP output fluorescence signals were invalid.

of a hypothetical ring oscillator (three inverters connected in a series loop) is also discussed in this chapter.

5.2 Results and Discussion

5.2.1 The $cI/\lambda_{P(R-O12)}$ Genetic Inverter

A simple inverter gives LOW output for HIGH input, and HIGH input for LOW output. The design of the $cI/\lambda_{P(R-O12)}$ inverter is as previously described in the thesis

work of Dr. Ron Weiss[28] (Figure 5.2). Simply described, the $\lambda_{P(R-O12)}$ is a synthetic promoter that lacks the O_R3 operator of the wild-type λ promoter. Repressor dimers of cI, the λ repressor, bind to O_R1 and O_R2 almost simultaneously; this cooperative binding could lead to much higher gains from the drastic change of repression activity over a small range of repressor concentrations. This also would achieve a highly nonlinear behavior as required in the circuit for a good digital performance. Two plasmids were eventually designed and modified to function as a genetic inverter in *E. coli* cells, pINV-112-R3 and pINV-107mut4. In this circuit, the repressor cI controls the output signal, the enhanced yellow fluorescent protein (EYFP), while it itself is controlled by another repressor, $lacI$. Under a constitutive promotor, $lacI$ is always expressed, repressing the expression of cI. However, in the presence of an inducer, isopropyl-β-D-thiogalactoside (IPTG, which inhibits the binding of $lacI$ to its operator region), cI is expressed with enhanced cyan fluorescent protein (ECFP) under the same promoter. This genetic inverter switches from "HIGH" (high EYFP fluorescence) to "LOW" (low EYFP fluorescence) output ranges depending on the concentration of the inducer.

The transfer function of this logic gate was then estimated by measuring several points on the curve. The mRNA level of the input protein, cI, represents a input signal in this circuit[28]. By measuring the fluorescence intensities of ECFP in *E. coli* cells, the actual mRNA signal can be approximated[28]. Similarly, the mRNA level of the output protein, EYFP, represents the output signal. This output signal level can also be approximated by measuring the fluorescence intensities of EYFP in cells. Since EYFP and ECFP are nearly identical in their decay rates and can have equivalent translation rates, the relative levels of these proteins can be normalized in terms of their fluorescence and protein numbers. The relationship between the ECFP and EYFP fluorescence intensities was approximated by comparing the fluorescence values of pINV-102[1] and pINV-112-R3 cell populations induced at 1000 μM IPTG as they flowed through μFACS. The "absolute" values of their fluorescence intensities

[1]The pINV-102 plasmid was constructed by inserting a p(lacIq):lacI region and EYFP into pPRO-Tet.E132 backbone (Clonetech). The pINV-107 plasmid was derived by inserting the p(lac):EYFP region from pINV-102 into the pBR322 backbone (Clonetech) and replacing p(lac) with $\lambda_{P(R-O12)}$.[28]

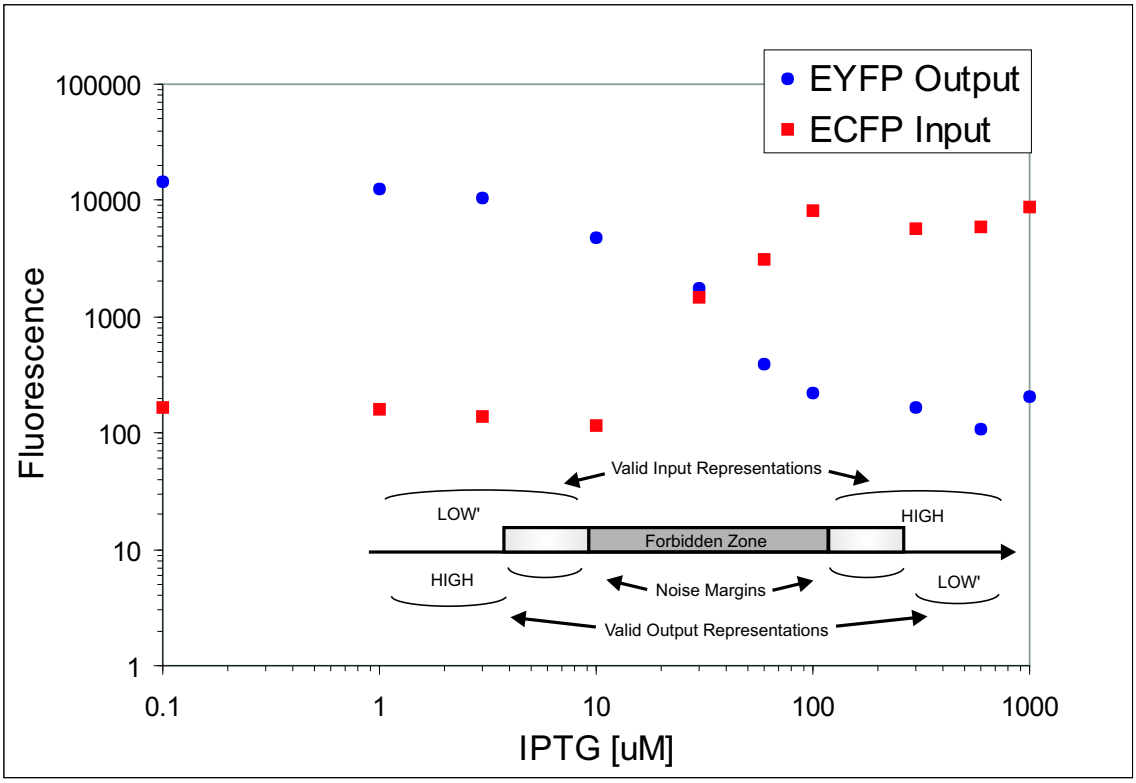

Figure 5.4: ECFP input (red squares) and EYFP output (blue dots) signals at different IPTG concentrations. The forbidden zone, or the sharp transition, is mapped out in the range of 10–100 μM IPTG. The noise margins are immediately before or after the transition, at 3 and 100 μM IPTG, respectively.

were obtained from their mean fluorescence values subtracted by the background noise and then divided by the numbers of cells scanned. The ratio of the fluorescence intensities of ECFP and EYFP can then be estimated from these two "absolute" values. All the figures shown in this chapter were normalized for the ECFP input and EYFP output signal levels.

Figure 5.3 shows the μFACS data in the form of histograms of output signals of the inverter at various concentrations of IPTG. At low concentration of 0.1 μM IPTG (LOW input signal), the output EYFP signal levels were HIGH. At high concentration of 1000 μM IPTG (HIGH input signal), the output EYFP signals were LOW. At the forbidden zone of intermediate input signals, 30 μM IPTG, the EYFP output signals varied widely among these cells and thus were invalid. As the graph of the ECFP input and EYFP output signals at various concentrations of IPTG in Figure 5.4 shows,

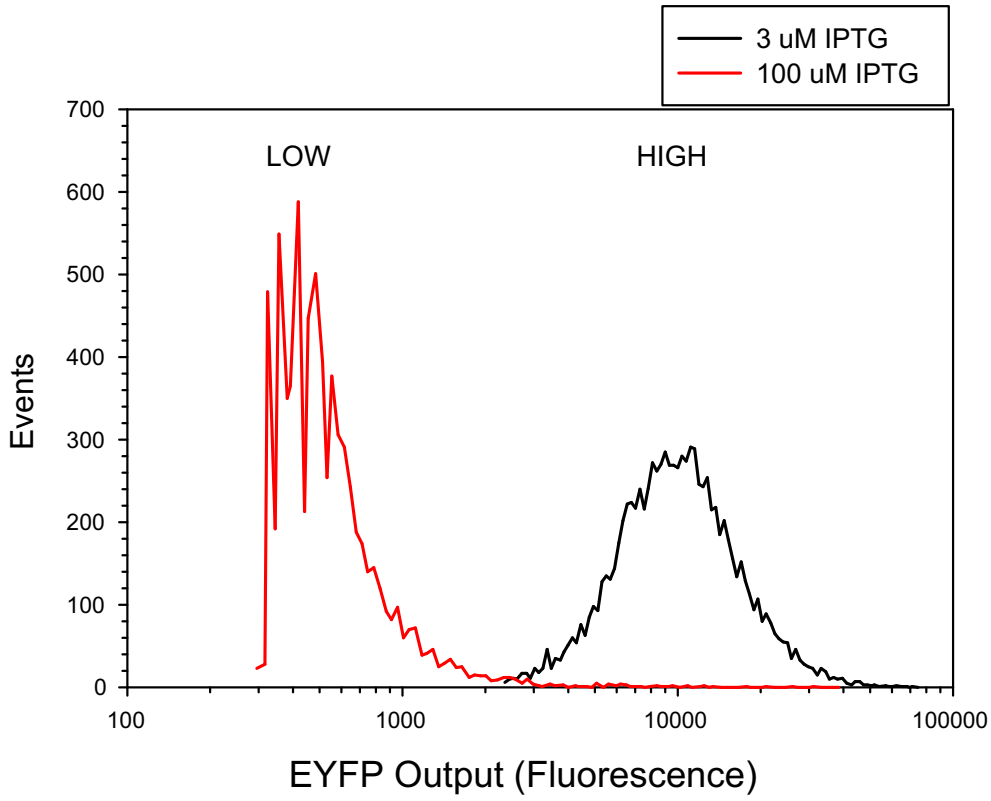

Figure 5.5: The noise margins of the $cI/\lambda_{P(R-O12)}$ inverter. Immediately before and after the transition, at 3 and 100 μM IPTG, respectively, the inverter can still output valid HIGH or LOW output signals from the marginally valid input signals.

the transition (or the forbidden zone) between HIGH and LOW states occurred in the range of 10–60 μM IPTG region. This sharp transition clearly displays the highly nonlinear behavior of the circuit due to the cooperative binding of the repressors.

There were also good noise margins between the HIGH and LOW output signals. Immediately before and after the transition, that is, at 3 and 100 μM IPTG, respectively, the output EYFP fluorescence levels did not overlap, as shown in Figure 5.5. Thus this inverter was able to restore marginally valid input signals to valid physical logic representations of HIGH or LOW output signals. This is critical for tolerating noise or loss of signals within the circuit. If some of the input signals are lost due to diffusion or interference with the host mechanism, these reduced input

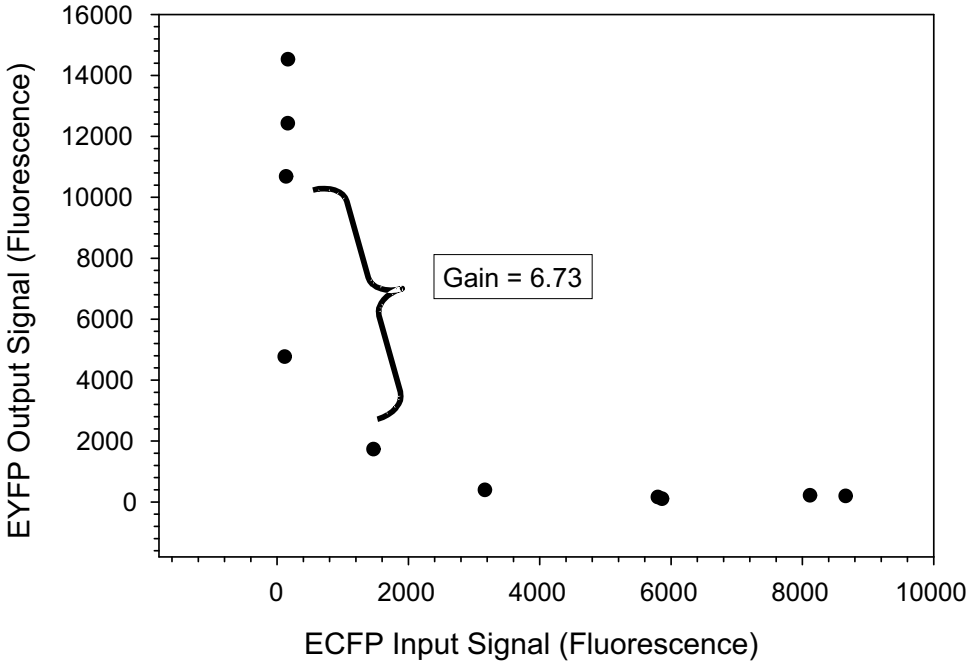

Figure 5.6: The transfer function of the $cI/\lambda_{P(R-O12)}$ inverter. The gain of the inverter was estimated from the slope of the curve.

signals can still be valid and be restored through digital abstraction. By normalizing their fluorescence intensities, a transfer curve of the ECFP input signals and EYFP output signals is plotted in Figure 5.6. These results demonstrate that this genetic inverter does exhibit fairly high gain of 6.73 and good noise margins for digital logic computation.

5.2.2 A Transfer Band

The transfer curve in Figure 5.6 is plotted using the means of the fluorescence intensities of the cell populations induced under different IPTG concentrations. This curve does not, however, describe the fluctuations that occur within biological systems. These fluctuations can be inherent due to stochastic effects, dead or damaged cells,

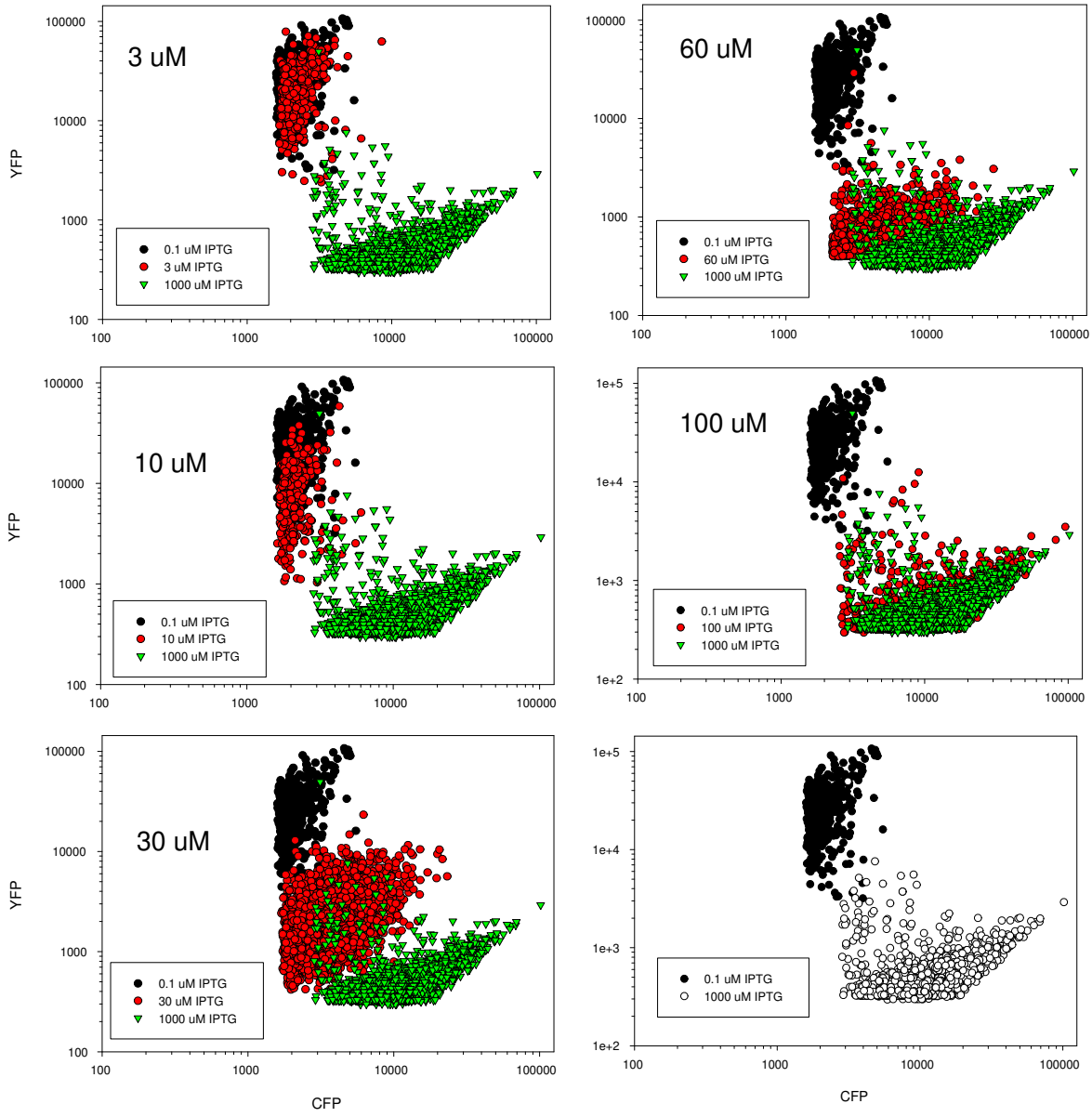

Figure 5.7: Scatter plots of cell populations at different IPTG concentrations of the $cI/\lambda_{P(R-O12)}$ inverter are shown as red dots. Approximately 10,000 cells were measured in each concentration. The populations at 0.1 (black dots) and 1000 μM (green triangles) concentrations are shown on every plot for comparison of HIGH and LOW signal ranges.

size distribution in addition to the systematic variations from μFACS. Scatter plots of cell populations at different IPTG concentrations of the $cI/\lambda_{P(R-O12)}$ inverter are shown in Figure 5.7. These plots reflect the distributions of the cells at different input levels. An alternative way introduced by Weiss[28] to describe the transfer function of a genetic logic gate, the *transfer band*, is intended to capture such noise in signal levels within biological systems. This band maps out a region, which includes the maximum and minimum values of input and output signal levels, that encompasses these fluctuations. The transfer band of the $cI/\lambda_{P(R-O12)}$ inverter, shown in Figure 5.8, is enclosed by a pair of transfer functions: one maps to the values of the mean plus one standard deviation of the input and output signals at each IPTG concentration, and the other maps to the values of the mean minus one standard deviation of the input and output signals. This band thus represents $\sim$70% of all the cell populations, since it includes all the cells that are within one standard deviation away from the mean value.

5.2.3 An Oscillator

In order to determine the efficacy of the $cI/\lambda_{P(R-O12)}$ inverter in a complex circuit, we use a hypothetical ring oscillator as an example to predict the correct behavior of the circuit. A ring oscillator consists of three inverters connected in a series loop[28]. The correct behavior of this circuit greatly depends on the steady state characteristics of its component inverters[28]. The signal ranges of the HIGH and LOW input and output, the gate thresholds, must be appropriately matched for the three inverters.

First consider two inverters, A and B, connected in series such that the output of A must be coupled to the input of B. This circuit would work *if and only if* the minimum of the HIGH output signal range of A is greater than the minimum valid value of the HIGH input signal range of B, and the maximum value of the LOW output signal range of A is less than the minimum valid value of LOW input signal range of B[28].

If three identical $cI/\lambda_{P(R-O12)}$ genetic inverters, A, B and C, are hypothetically

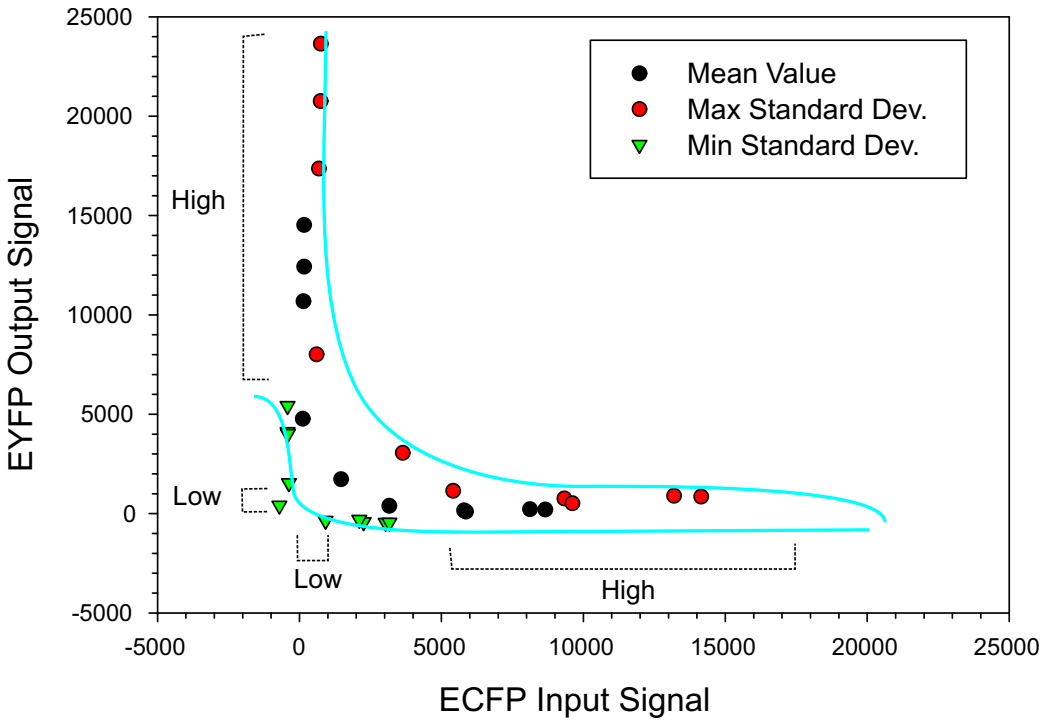

Figure 5.8: The transfer band of the $cI/\lambda_{P(R-O12)}$ inverter is plotted using two transfer functions. One transfer function (red dots) is plotted using the values of the mean plus one standard deviation of the input and output signals at each IPTG concentrations. The other transfer function (green triangles) is plotted using the values of the mean minus one standard deviation at different IPTG concentrations. Some of the minimum values are in the negative range. The mean values of the transfer function are shown (•). The ranges of the HIGH and LOW inputs and outputs are also shown. This transfer band represents ∼70% of the cells.

connected in a series loop as a ring oscillator (ignoring the fact that it will short the circuit *in vivo*), we can predict the outcome of this circuit's behavior by matching their gate thresholds according to the transfer band in Figure 5.8. If A outputs a marginally valid HIGH output signal level of 5000 (see the noise margins in Figure 5.5), this is just above the minimum value of the inverter B at the HIGH input range. Then if B outputs a marginally valid LOW output signal of ∼1000, this signal is also just below the minimum value of the LOW input signal of the inverter C, and etc. Thus we should be able to observe oscillatory behavior from this circuit. However, since the values of the inverters' HIGH and LOW output ranges are so close to the values of the noise margins of their HIGH and LOW input ranges, any loss of signals from one gate to another gate could produce an input signal that falls within the forbidden zone. Hence, we can predict that a small fraction of the cell populations would not exhibit oscillation and the fraction of the cells that do would have their oscillations be eventually dampened. In order for this oscillator to behave more predictably and reliably, higher gain and/or higher nonlinearity of the component inverters have to be achieved. Nonetheless, this example shows the feasibility of the $cI/\lambda_{P(R-O12)}$ inverter to be used for digital logic computation.

The oscillator made by Elowitz *et al.* [87] also consisted of three inverters. They found that only 40% of the cells were able to exhibit oscillations. Yet, there were significant variations in the period and amplitude of oscillator's output from cell-to-cell and from parent-to-progeny. They claimed that this phenomenon may be due to the inherent biological stochastic noise. However, it may also be due to the inappropriate matching of the gate thresholds of the three inverters such that the behavior of the oscillator was unreliable and unpredictable[28].

A critical aspect of designing complex genetic circuits is having a resource of gates with different DNA-binding proteins and their respective binding regions. Although a number of natural DNA-binding proteins and their reaction kinetics are known, modifications of these proteins and their binding regions are pivotal to correctly program cell behaviors[87, 28]. Future work in designing new circuits will inevitably be paralleled by the advances in our understanding of gene regulatory mechanisms and in our

ability to create novel DNA-binding proteins. We plan to use directed evolution[66] to fine-tune the existing genetic logic gates and to create novel genetic regulatory elements in order to construct faster and more complex circuits[90]. Moreover, the transfer curve only describes the static behaviors of the circuit, but not the dynamic behaviors. Hence, as part of our future work, we seek to use μFACS to take time-course measurements such that the dynamic behavior of the circuit could also be determined.

5.3 Conclusion

Artificial genetic networks will one day enable us to program living cells to perform computational functions and thus behave predictably and reliably. This technology could be useful in a number of applications which require decision-making logistics, such as biosensors, bioremediation, biocomputing and drug manufacturing. Using μFACS, we were able to characterize the gate thresholds and noise margins of a simple logic gate, a genetic inverter. In the near future, we plan to fine-tune these logic gates by directed evolution and perform high throughput screening using μFACS. By building up a repertoire of these genetic gates, we will be able to design more complex circuits to program the cells to perform biocomputing and behave more intelligently.

5.4 Materials and Methods

5.4.1 μFACS

The devices used for flow cytometric measurements were fabricated according to the procedures in Chapter 2. The conditions and growth of *E. coli* cells for the transfer curve experiments were as previous described in the thesis work of Dr. Ron Weiss[28]. Cells were grown in LB media with appropriate antiobiotics (ampicillin and kanamycin). Fresh cultures was inoculated at 1000:1 dilution into new tubes with fresh media at different inducer concentrations. The cultures were grown to log phase

at 37° C in an incubator at 250 RPM. These cells were then resuspended in PBS three times and lastly resuspended in PBS with BSA. The cells were filtered through a 5 μm filter immediately before cytometry.

Cells were then introduced into the chip at 1.5 psi back pressure. Approximately 10,000 events were taken for each inducer concentration in 8–10 min.

5.4.2 Optical Setup

A schematic of the optical setup for simultaneous excitation and detection of ECFP/EYFP is as follows. The 5 W Argon laser (Coherent Innova 70) was operating in multiline mode (output lines: 457.9, 465.8, 472.2, 476.5, 488.0, 496.5, 501.7, 514.5, 528.7 nm). A 495DCLP dichroic filter (Chroma, Brattleboro, VT) was placed in front of the laser to separate the beam into two paths. The lines that were longer than 495 nm passed straight through the dichroic filter into an optical filter 514±5 nm and a neutral density (ND3) filter (Edmund Scientific) and then into the microscope. The lines shorter than 495 nm were reflected at an angle into two reflecting mirrors which were used to adjust the direction of the beam path. These lines were then filtered through two identical optical filters, 458±5 nm. The 458 nm line was reflected by another dichroic filter 500DCLP into the microscope. We now could excite both ECFP and EYFP simultaneously.

The detection scheme is similar to the one previously described in Chapter 2. The emitted fluorescence was split by a dichroic filter, 520DCLP, into the two PMTs, 480±20 nm for ECFP detection and 535±20 nm for EYFP detection. The bias on the EYFP PMT was set at -800 V, while the bias on ECFP PMT was set at -999 V.

Chapter 6
Flow Cytometry of Magnetotactic Bacteria Using a Microfluidic Cell Sorter and a SQUID Microscope

6.1 Introduction

Since the discovery of magnetotactic bacteria by Blakemore in 1975[92, 93], the capability of these bacteria to produce ferromagnetic nano-crystals to perform various navigational functions has fascinated researchers from various disciplines. These nano-crystals, mainly magnetites (Fe_3O_4) and greigite (Fe_3S_4), are enclosed within membrane vesicles, called magnetosomes, which are arranged in chains or clusters fixed within the cytoplasm. When exposed to a magnetic field, these magnetosomes are able to orientate the entire bacterium to align along the magnetic field. Ferromagnetic materials have also been found in a diverse group of organisms for geomagnetic sensing, including algae, insects[94], molluscs, fish[95, 96], bird[97, 98] and even humans[99, 100, 101]. Such discoveries have prompted the developments of different magnetic separators and magnetometers to isolate these cells and study their biomagnetic properties.

Most magnetic separators divide magnetic from nonmagnetic components within a mixture. Magnetic particles can be isolated directly from their own environments without much sample preparation. Simple magnetic cell separators operate in a batch mode with a strong permanent magnet embedded in disinfectant-proof material. Samples can then be introduced inside microtubes or test tubes to be enriched. Other more sophisticated and highly selective cell separators employ a continuous flow-

through scheme. High gradient magnetic separators (HGMS) are comprised of small columns loosely packed with magnetic steel wool[102]. These columns are situated between two strong permanent magnets. Magnetic cells are injected into the columns and retained on the steel wool. When the field is removed, the magnetic cells can be eluted. In other continuous-flow sorters, as the cells pass through a magnetic field in a stream, they are deflected from the nonmagnetic cells into another outlet according to their magnetic dipole moments[103, 104, 105]. These magnetic separators are used in a variety of fields including microbiology, immunomagnetic assays using paramagnetic and ferromagnetic beads, colloidal labels, or the specific surface carbohydrate binding molecules[106]. Although they do provide relatively rapid and accurate separation, these separators operate in low resolution and thus are limited to the applications that mainly require the isolation of magnetotactic or magnetically labeled cells from their nonmagnetic counterparts.

Efforts to address the molecular biology of the magnetite formation within magnetotactic cells have been hampered by the elaborate techniques and requirements to create proper media and microaerobic conditions for these cells, the lack of a significant number of the bacterial strains and the inability for these strains to grow on agar plates in order to screen for mutants. In addition, many different species of magnetotactic bacteria can co-inhabit together in the same living environment. They are distinct from each other according to their sizes, shapes, magnetic dipole moments and the organization of the magnetosomes. However, existing magnetic separators cannot sort these species or mutants with high resolution and accuracy to isolate certain target cells and study them individually. Hence the knowledge concerning gene determination and regulation of magnetosome formation is still incomplete.

To address these demands, we have integrated the technologies of a microfluidic cell sorter and a high spatial resolution magnetometer to perform high throughput screening of magnetotactic bacteria (See Figure 6.1). The magnetometer is a high resolution low-temperature superconductivity SQUID (superconducting quantum interference device) microscope[107]. Chemla *et al.* have observed various motions of magnetotactic bacteria and even of a single living bacterium using a similar SQUID

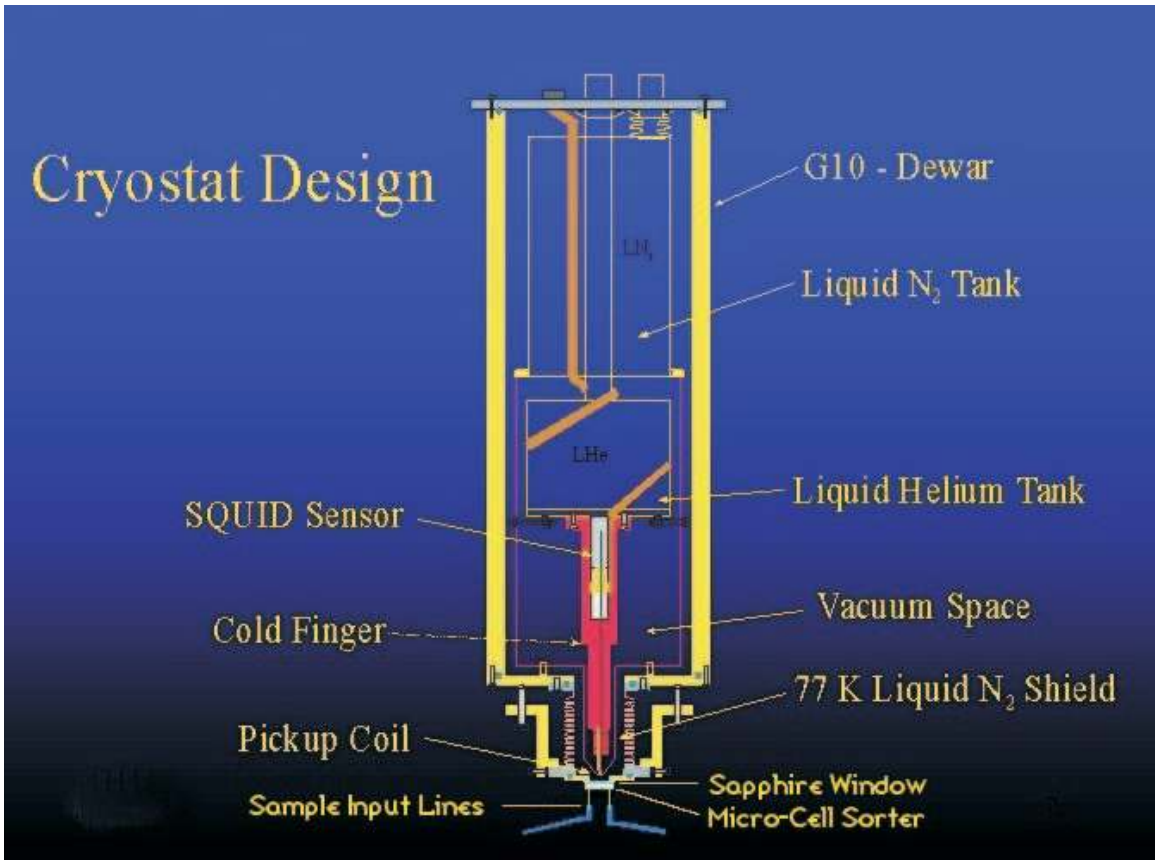

Figure 6.1: A microfluidic cell sorter is attached to the sapphire window of the SQUID microscope. This is a schematic of the design of a SQUID microscope. This SQUID microscope is designed such that measurements can be taken from samples at room temperature. The sapphire window provides an insulation from the 77 Kelvin degree temperature within the SQUID detector.

microscope[108, 109, 110]. The cell sorter was attached to the detection window of the SQUID microscope as shown in Figure 6.1. Magnetotactic bacteria were introduced into the cell sorter and detected by the SQUID microscope. The advantages of integrating these two technologies are 1) a SQUID microscope could have the sensitivity to differentiate various magnetic dipole moments from several species of magnetotactic bacteria, 2) optical and magnetic measurements could be coupled such that the use of light scattering and fluorescent tags can be used in conjunction with the magnetic tags, and 3) cells with different magnetic properties could be sorted. Here we have demonstrated the potential in using the SQUID microscope and the microfabricated cell sorter to analyze and sort biomagnetic cells and/or particles.

6.2 Results and Discussion

6.2.1 Microfluidic Cell Sorters and the SQUID Microscope

Since the magnetic field strength falls off with r^{-3}, the diameter and the number of turns (the effective sensing area) of the pickup coil and its distance away from the sample become very significant in optimizing the submillimeter spatial resolution and the field sensitivity for the SQUID microscope. Two SQUID microscopes, namely NanoSQUID I and NanoSQUID III, were used for cytometric measurements of magnetotactic bacteria. NanoSQUID III, having a 500 μm diameter pickup coil with 20 turns, has a spatial resolution of 500 μm with a magnetic field sensitivity of 330 fT/Hz$^{\frac{1}{2}}$, whereas NanoSQUID I, which has a 250 μm diameter pickup coil with 10 turns, has a spatial resolution of 250 μm with a magnetic field sensitivity of 850 fT/Hz$^{\frac{1}{2}}$ [107]. However, the field sensitivity decreases depending on the velocities of the cells flowing through the detection region.

Two important considerations when attaching the cell sorter to the SQUID microscope were the location of the T-junction with respect to the center of the pickup coil and the distance of the coil to the actual sample within the sorter. Figure 6.2 shows optical micrographs of an enclosed cell sorter attached to the sapphire window of the SQUID microscope. Figure 6.2 (A) and (B) focus on T-Channel of the microfluidic cell sorter with the pickup coil in the background. Figure 6.2 (C) and (D) focus the pickup coil of the SQUID at different angles with respect to the T-channel in the front view and vice versa in Figure 6.2 (E) and (F). As these pictures show, our detection region, as the effective sensing area of the pickup coil, was set at the region of the input arm of the T-junction and the T-junction.

Both cultured and natural magnetotactic bacteria were tested for their magnetic field strengths. AMB-1 and the natural magnetotactic bacteria, in 0.5 μL suspensions, were placed respectively on the sapphire window. Random motions of these bacteria, such as vibrational, rotational, and swimming, were detected by the SQUID microscope. Figure 6.3 shows the qualitative power spectra of these measurements in the range of 1–100 Hz. The magnitudes of signals from these two types of bacteria were

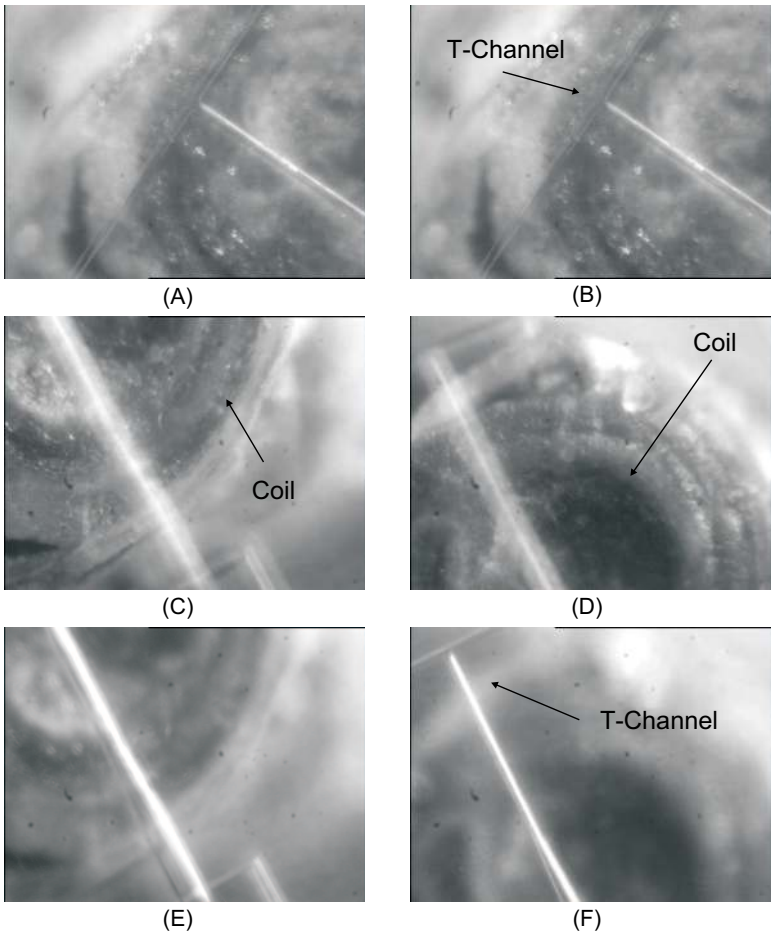

Figure 6.2: Optical micrographs of the cell sorter and the pickup coil of the SQUID microscope. See text for details.

considerably different. The natural magnetotactic bacteria exhibited much higher magnetic field strength than the cultured AMB-1. Thus the natural magnetotactic bacteria was introduced into the cell sorters for the rest of our measurements.

6.2.2 Completely Enclosed Cell Sorters

Figure 6.4 shows the initial power spectra of the magnetic field produced by bacteria flowing through an enclosed cell sorter were taken by NanoSQUID III. The distance between the pickup coil and the actual cell sample was $\sim$100 μm. A background field noise spectrum was taken before the introduction of the bacteria. Natural magnetotactic bacteria were then introduced into the sorter using nitrogen back pressure at 4.0 psi. The SQUID microscope was able to detect the magnetic fields produced

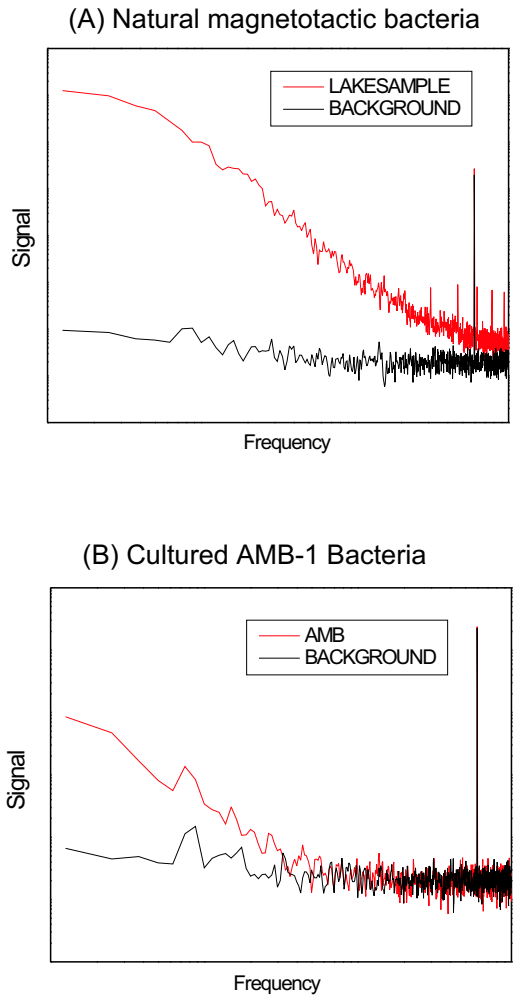

Figure 6.3: Qualitative power spectra of natural and cultured magnetotactic bacteria.

by these bacteria as they flowed through the detection area as shown in Figure 6.4. When the nitrogen pressure was turned off, the SQUID microscope was able to reproduce the background spectrum again, indicating that little or no magnetotactic bacteria were flowing through the detection area. From the optical microscope, the cell velocity near the T-junction of the sorter at 4.0 psi input pressure was more than 50 mm/sec at 10–50 cells/sec.

The peristaltic pump on the sorter was then used for sample injection instead of direct nitrogen back pressure. The bacteria were pumped through the cell sorter at 24 Hz frequency, having an estimated velocity of 10–15 mm/sec. Similar spectrum were

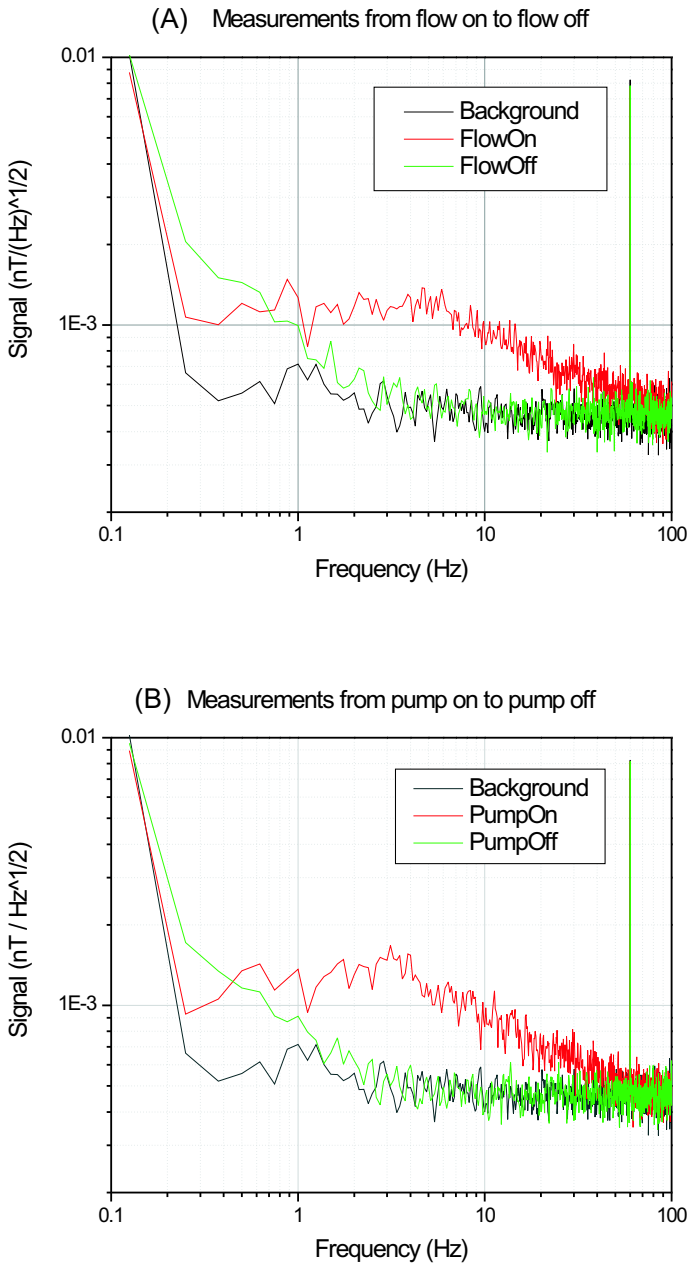

Figure 6.4: Power spectra of the magnetic field produced by the bacteria as they flowed through the PDMS enclosed sorter. (A) is the magnetic field power spectrum taken when the cells were introduced at 4 psi. (B) is the spectrum taken when the cells were peristaltically pumped at 24 Hz.

obtained as shown in Figure 6.4. Under the observation of an optical microscope, ∼20 bacteria per second were flowing through the detection area. Comparing the signal levels of frequencies below 10 Hz to the background noise level, the magnetic power spectra increased from 0.4 pT/Hz$^{\frac{1}{2}}$ to 1.0 pT/Hz$^{\frac{1}{2}}$. Thus NanoSQUID III was able to detect an ensemble of magnetotactic bacterial cells (ranging from 10–50) flowing at velocities greater than 10 mm/sec with a signal-to-noise ratio of approximately 2:1 for these parameters. The cut-off frequency of the signals from the cells flowing through the sorter was ∼60 Hz, which means that the SQUID microscope could not detect any other magnetic fluctuations above 60 Hz.

This low signal-to-noise ratio may be attributed to the velocity of the cells as they pass through the detection region and their long distance from the pickup coil. In Chelma *et al.* , the MS-1 *M. magnetotactium* bacteria were brought to within 15 μm of the SQUID. They measured the field produced by an ensemble of motile and nonmotile bacteria ($\sim 10^8$ cells) placed inside a microfabricated silicon well integrated with their detection window. In our study, we were measuring a much smaller ensemble of cells (ranging from 10–50 cells/sec) flowing through the detection region inside a microchannel either by direct pressure application or peristaltic pumping. The sensitivity of the SQUID was greatly compromised by the speed of detection. The cells were also flowed through the device at different pressures of 4 psi, 6 psi, 8 psi. But there was not any difference in the power spectra resulting from the variation in cell velocities (data not shown). Due to the mechanical design of NanoSQUID III, the pickup coil could not be moved closer (< 100 μm) to the sorter for more sensitive measurements.

6.2.3 Open-channel Cell Sorters

An open-channel cell sorter (Fluidigm, Inc.) was attached directly onto the sapphire window of the NanoSQUID I microscope in order to reduce the distance between the pickup coil and the cell sample. This distance was now reduced to 30–40 μm. The natural magnetotactic bacteria were introduced at a much lower input pressure of 0.5

psi. From Figure 6.5, natural magnetotactic bacteria were detected to have magnetic power spectrum of 5.0 pT/Hz$^{\frac{1}{2}}$ from the 2.0 pT/Hz$^{\frac{1}{2}}$ background noise. This increase in the signal levels can be attributed to the shorter distance from the cell sample to the coil.

The pickup coil was then moved closer to the sorter; so now the distance between them was 20–25 μm. Natural magnetotactic bacteria were peristaltically pumped through the sorter at a very low frequency of 7 Hz, having linear flow velocity of < 5 mm/sec. Figure 6.5 shows the power spectrum of these cytometric measurements. There was an increase in the signal level in the detection of these bacteria of 13 pT/Hz$^{\frac{1}{2}}$ from the 2.0 pT/Hz$^{\frac{1}{2}}$ background noise level. This resulted in a signal-to-noise ratio of 6:1.

Another set of measurements were taken by pumping the bacteria at 3 Hz. This time, however, the pickup coil had to be retracted from the window several times by a few μm to prevent it from contacting the detection window. Figure 6.5 shows a small reduction in the amplitude of the signal resulting from increasing the distance between the pickup coil and the bacteria to $\sim$50 μm.

The orientation of the bacteria may be randomized by the tumbling motion as they flowed through the microchannels. This would decrease their net magnetic dipole moment. An external magnetic field was used near the cell sorter to align the bacteria in order to increase their net dipole moment. However, this external field was proven to be too noisy for our experiments. Then we tried to induce some "wiggle" motion into the flowing bacteria by actuating one valve on the sorter at certain frequencies. In this way, we may be able to lock into some frequency signals. Unfortunately, there was not any increase in signal at the wiggle frequency. This may be due to the fact that the SQUID microscope was not sensitive for these signals or that the cells did not wiggle at all.

One of the objectives of this project was to screen the magnetotactic BAC library using the cell sorter and the SQUID microscope. However, this experiment was not performed since we were not able to achieve higher signal-to-noise ratio. An alternative way may be to have an array of these cells in μL volume on a glass slide.

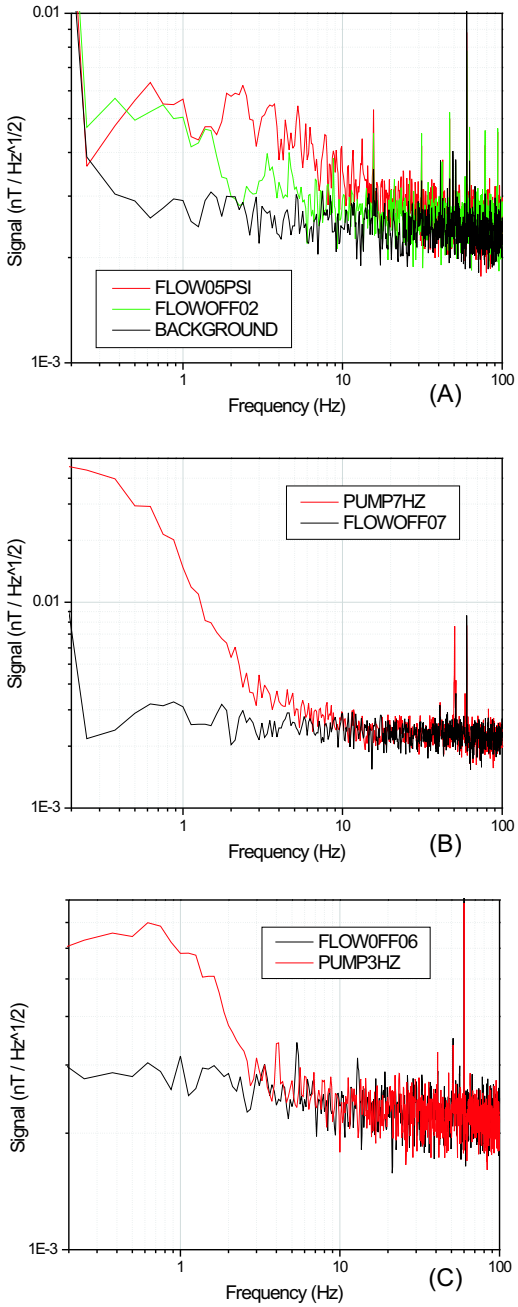

Figure 6.5: Power spectra of the magnetic field produced by the bacteria as they flowed through the Fluidigm sorter. (A) is the magnetic power spectrum taken when the cells were flowing at 0.5 psi, with the pickup coil at 40 μm away. (B) and (C) were cells being peristaltically pumped through the sorter at 7 and 3 Hz, respectively. Note that the distance between the sorter and the pickup coil is 25 μm and $\approx$ 50 μm for 7 and 3 Hz pumping frequency, respectively.

The SQUID microscope could scan the glass slide and integrate the signals over time to achieve higher sensitivity. We could then identify the spots that have any magnetic field strength and study these cells more closely.

6.3 Conclusion and Future Work

We have demonstrated the capability of the elastomeric microfluidic sorter to be integrated into a SQUID microscope. We also have taken initial cytometric measurements of magnetotactic bacteria flowing through the sorter either by direct pressure application or peristaltic pumping. The best signal-to-noise ratio for our present setup is 6:1. However, at this point, the SQUID microscope did not have the sensitivity to be able to detect a single magnetotactic bacterium flowing through the cell sorter in real time.

The technical limitations that we are presently facing could be resolved by using different designs of the microchannels and increasing the sensitivity of the SQUID microscope. If the microchannel is designed to have some kind of pattern, such as a sine wave or a triangular wave instead of a linear channel, then the SQUID may be able to pick up such frequency as the cells flow through the channels. More importantly, the SQUID microscope must have higher subpicoTesla sensitivity to compensate for the velocity of the cells. This field sensitivity can be increased by designing a new mechanism to move the pickup coil closer and by microfabricating the pickup coils to have more turns, increasing its sensitivity.

Once the SQUID microscope achieves higher field sensitivity, we could then address more interesting questions concerning the molecular biology of magnetite formation in bacteria and higher eukaryotes. Different magnetotactic bacteria could then be isolated according to their magnetic dipole moments for individual studies. The BAC libraries of MS-1 bacteria, human and drosophila could then be screened for mutants with magnetite formation. The field of biomagnetism is still in its infancy after more than a quarter of a century of research starting with magnetotactic bacteria. The integration of μFACS and the SQUID microscope could open up new

avenues to accelerate the study of these magnetotactic cells.

6.4 Materials and Methods

This project explicitly shows the unique environment for interdisciplinary collaborations that Caltech has been well known to foster. The *Magnetospirillum* AMB-1 bacteria and the magnetotactic BAC library were cultured in Prof. Bruce Hay's Lab at the Department of Biology and in Prof. Frances Arnold's lab at the Department of Chemical Engineering. The natural magnetotactic bacteria were isolated and purified by Dr. Lea Cox at the Department of Geological and Planetary Science. The microfabricated cell sorters were made at the Department of Applied Physics and at Fluidigm, Inc. (South San Francisco, California). My colleagues, Dr. Franz Baudenbacher, Luis E. Fong, Eric Chancellor, and I took the cytometric measurements on the SQUID microscope at the Department of Physics, Vanderbilt University, Nashville, Tennessee.

6.4.1 Magnetotactic Bacteria

AMB-1 Magnetotactic Bacteria

The *Magnetospirillum* strain, AMB-1, was grown in microaerobic conditions using a modified Matsunga yeast medium[111, 112]. Fresh cell cultures (courtesy of Dr. L. Elizabeth Bertani) were inoculated into the growth medium in the ratio of 1:100. The culture tubes were then sealed with parafilm and incubated at room temperature for 3–4 days. Magnetotactic bacteria were collected at the bottom of the culture tubes using magnetic stir bars and resuspended in its growth medium.

Natural Magnetotactic Bacteria

Natural magnetotactic bacteria were collected by Dr. Lea Cox near a lake at the Los Angeles Arboretum. These bacteria were concentrated by placing a magnetic stir bar at the sides of the collection bottles. These bacteria were retrieved by a glass pipet

and resuspended in filter-sterilized lake water.

Magnetotactic BAC Library

The BAC library, made from the MS-1 *Magnetospirillium magnetotactium* bacteria, was provided by Prof. Bruce Hay. The library was inoculated into LB with 15 μg/mL Chloramphenicol and 25 μmol Ferric Quinate. The bacteria were allowed to grow in a 37° C incubator for four hours and then were transferred to an incubator with 99% nitrogen and 1% oxygen at room temperature. After three days, the library was resuspended in 100 μM of sodium phosphate with 1% formaldehyde for two hours to fix the cellular membrane. To prevent contamination, the cells were resuspended again in 100 μM of sodium phosphate with 0.01% sodium azide.

6.4.2 Microfabricated Cell Sorter

We used two different designs of microfabricated sorters for the SQUID measurements. One design was made at Caltech by me and the other design was made at Fluidigm, Inc. Both sorters were fabricated using multilayer soft lithography, having integrated valves and pumps. Yet, they have slightly different designs of valves and pumps, PDMS compositions and number of layers. The Caltech sorters were made of three layers in order to have completely enclosed fluidic channels and the Fluidigm sorters have open fluidic channels made of two layers.

We adhered the Fluidigm chips directly onto the sapphire window of the SQUID microscope. This eliminated any distance between the sapphire window and the cell sample. The sorter and the sapphire window were heated at 90° C by shining a halogen lamp for 2 hours to promote stronger bonding at the interface. The bonding between the two surfaces was then able to sustain more than 6.0 psi of input nitrogen pressure. The enclosed Caltech sorters do not require any wait time for the sorter to adhere. However, it has an extra PDMS layer of 25 μm thickness for channel enclosure, leaving some distance between the sapphire window and the sample.

Pneumatic valves and the PC interface breakout board for actuating the sorters

were also provided by Fluidigm, Inc. Peristalsis patterns used were as previously described in Chapter 3.

Cells were introduced into the sorter *via* TYGON tubing (Cole-Parmer, Inc., Vernon Hills, IL) connected to a glass microcapillary (Drummond Scientific Company, Broomall, PA). The other end of the tubing was connected to a nitrogen gas regulator. The microcapillary was first inserted into the cell sorter and the cell sample was introduced by increasing the nitrogen back pressure.

6.4.3 SQUID Microscope

The designs and constructions of the two SQUID microscopes, NanoSQUID I and NanoSQUID III, were as previously described[107]. The diameters of the pickup coils (a superconducting flux transformer) for NanoSQUID I is 250 μm with a total of 10 turns and for NanoSQUID III is 500 μm with a total of 20 turns. The distance between the pickup coil and the sapphire detection window was adjusted using a bellows mechanism.

Bibliography

[1] J. V. Watson. *Introduction to Flow Cytometry.* Cambridge University Press, 1st edition, 1991.

[2] Howard M. Shapiro. *Practical Flow Cytometry.* Wiley-Liss, 3rd edition, 1995.

[3] H. Cai, P. S. White, D. Torney, A. Deshpande, Z. L. Wang, R. A. Keller, B. Marrone, and J. P. Nolan. Flow cytometry-based minisequencing: A new platform for high-throughput single-nucleotide polymorphism scoring (vol 66, pg 135, 2000). *Genomics*, 69(3):395–395, 2000.

[4] J. P. Nolan and L. A. Sklar. The emergence of flow cytometry for sensitive, real-time measurements of molecular interactions. *Nature Biotechnology*, 16(7):633–638, 1998.

[5] G. Georgiou. Analysis of large libraries of protein mutants using flow cytometry. *Advances in Protein Chemistry, Vol 55*, 55:293–315, 2001.

[6] B. P. Cormack, R. H. Valdivia, and S. Falkow. FACS-optimized mutants of the green fluorescent protein (gfp). *Gene*, 173(1):33–38, 1996.

[7] M. R. Melamed, T. Lindmo, and M. L. Mendelsohn, editors. *Flow Cytometry and Sorting.* Wiley-Liss, Inc., 1st edition, 1990.

[8] J. C. McDonald, D. C. Duffy, J. R. Anderson, D. T. Chiu, H. Wu, O. J. A. Schueller, and G. M. Whitesides. Fabrication of microfluidic systems in poly(dimethylsiloxane). *Electrophoresis*, 21(1):27–40, 2000.

[9] D. J. Harrison, K. Fluri, K. Seiler, Z. H. Fan, C. S. Effenhauser, and A. Manz. Micromachining a miniaturized capillary electrophoresis-based chemical-analysis system on a chip. *Science*, 261(5123):895–897, 1993.

[10] R. B. M. Schasfoort, S. Schlautmann, J. Hendrikse, and A. van den Berg. Field-effect flow control for microfabricated fluidic networks. *Science*, 286(5441):942–945, 1999.

[11] Y. N. Xia and G. M. Whitesides. Soft lithography. *Angewandte Chemie – Int. Ed.*, 37(5):551–575, 1998.

[12] G. M. Whitesides, E. Ostuni, S. Takayama, X. Y. Jiang, and D. E. Ingber. Soft lithography in biology and biochemistry. *Annual Review of Biomedical Engineering*, 3:335–373, 2001.

[13] Alice L. Givan. *Flow Cytometry: First Principles*. Wiley-Liss, Inc., New York, 1st edition, 1992.

[14] P. J. Crossland-Taylor. A device for counting small particles suspended in a fluid through a tube. *Nature*, 171:37–38, 1953.

[15] M. J. Fulwyer. Electronic separation of biological cells by volume. *Science*, 150:910–911, 1965.

[16] R. G. Sweet. High frequency recording with electrostatically deflected ink jets. *Rev. Sci. Inst.*, 36:131–133, 1965.

[17] H. P. Chou, C. Spence, A. Scherer, and S. Quake. A microfabricated device for sizing and sorting DNA molecules. *PNAS*, 96(1):11–13, January 1999.

[18] Marc Madou. *Fundamentals of Microfabrication*. CRC Press, 1997.

[19] D. C. Duffy, J. C. McDonald, O. J. A. Schueller, and G. M. Whitesides. Rapid prototyping of microfluidic systems in poly(dimethylsiloxane). *Anal. Chem.*, 70(23):4974–4984, 1998.

[20] T. Thorsen, R. W. Roberts, F. H. Arnold, and S. R. Quake. Dynamic pattern formation in a vesicle-generating microfluidic device. *Physical Review Letters*, 86(18):4163–4166, 2001.

[21] L. C. Waters, S. C. Jacobson, N. Kroutchinina, J. Khandurina, R. S. Foote, and J. M. Ramsey. Microchip devices for cell lysis, multiplex PCR amplification, and electrophoretic sizing. *Anal. Chem.*, 70(1):158–162, 1998.

[22] M. U. Kopp, A. J. de Mello, and A. Manz. Chemical amplification: Continuous-flow PCR on a chip. *Science*, 280(5366):1046–1048, 1998.

[23] F. Arai, A. Ichikawa, M. Ogawa, T. Fukuda, K. Horio, and K. Itoigawa. High-speed separation system of randomly suspended single living cells by laser trap and dielectrophoresis. *Electrophoresis*, 22(2):283–288, 2001.

[24] Y. C. Lin and M. Y. Huang. Electroporation microchips for *in vitro* gene transfection. *Journal of Micromechanics and Microengineering*, 11(5):542–547, 2001.

[25] J. S. Soughayer, T. Krasieva, S. C. Jacobson, J. M. Ramsey, B. J. Tromberg, and N. L. Allbritton. Characterization of cellular optoporation with distance. *Analytical Chemistry*, 72(6):1342–1347, 2000.

[26] A. Y. Fu, C. Spence, A. Scherer, F. H. Arnold, and S. R. Quake. A microfabricated fluorescence-activated cell sorter. *Nature Biotechnol.*, 17(11):1109–1111, November 1999.

[27] A. Y. Fu, H. P. Chou, C. Spence, F. H. Arnold, and S. R. Quake. An integrated microfabricated cell sorter. *Analytical Chemistry*, 2002. In press.

[28] Ron Weiss. *Cellular Computation and Communications using Engineered Genetic Regulatory Networks*. Ph.D. Thesis, Massachusetts Institute of Technology, 2001.

[29] M. Schena, D. Shalon, R. W. Davis, and P. O. Brown. Quantitative monitoring of gene-expression patterns with a complementary-DNA microarray. *Science*, 270(5235):467–470, 1995.

[30] M. Chee, R. Yang, E. Hubbell, A. Berno, X. C. Huang, D. Stern, J. Winkler, D. J. Lockhart, M. S. Morris, and S. P. A. Fodor. Accessing genetic information with high-density DNA arrays. *Science*, 274(5287):610–614, 1996.

[31] D. J. Lockhart, H. L. Dong, M. C. Byrne, M. T. Follettie, M. V. Gallo, M. S. Chee, M. Mittmann, C. W. Wang, M. Kobayashi, H. Horton, and E. L. Brown. Expression monitoring by hybridization to high-density oligonucleotide arrays. *Nature Biotechnol.*, 14(13):1675–1680, 1996.

[32] M. T. Laub, T. H. McAdams, T. Feldblyum, C. M. Fraser, and L. Shapiro. Global analysis of the genetic network controlling a bacterial cell cycle. *Science*, 290(5499):2144–2148, 2000.

[33] W. C. Nierman, T. V. Feldblyum, M. T. Laub, I. T. Paulsen, K. E. Nelson, J. Eisen, J. F. Heidelberg, M. R. K. Alley, N. Ohta, J. R. Maddock, I. Potocka, W. C. Nelson, A. Newton, C. Stephens, N. D. Phadke, B. Ely, R. T. DeBoy, R. J. Dodson, A. S. Durkin, M. L. Gwinn, D. H. Haft, J. F. Kolonay, J. Smit, M. B. Craven, H. Khouri, J. Shetty, K. Berry, T. Utterback, K. Tran, A. Wolf, J. Vamathevan, M. Ermolaeva, O. White, S. L. Salzberg, J. C. Venter, L. Shapiro, and C. M. Fraser. Complete genome sequence of *caulobacter crescentus*. *Proceedings of the National Academy of Sciences of the United States of America*, 98(7):4136–4141, 2001.

[34] O. Kuchner and F. H. Arnold. Directed evolution of enzyme catalysts. *Trends in Biotechnology*, 15(12):523–530, 1997.

[35] F. H. Arnold, P. L. Wintrode, K. Miyazaki, and A. Gershenson. How enzymes adapt: lessons from directed evolution. *Trends in Biochemical Sciences*, 26(2):100–106, 2001.

[36] R. P. Huang. Detection of multiple proteins in an antibody-based protein microarray system. *Journals of Immunological Methods*, 255(1-2):1–13, 2001.

[37] H. P. Feng. A protein microarray. *Nature Structural Biology*, 7(10):829–829, 2000.

[38] B. D. Martin, B. P. Gaber, C. H. Patterson, and D. C. Turner. Direct protein microarray fabrication using a hydrogel "stamper". *Langmuir*, 14(15):3971–3975, 1998.

[39] E. Ostuni, C. S. Chen, D. E. Ingber, and G. M. Whitesides. Selective deposition of proteins and cells in arrays of microwells. *Langmuir*, 17(9):2828–2834, 2001.

[40] J. Ziaudinn and D. M. Sabatini. Microarrays of cells expression defined cDNAs. *Nature*, 411:107–110, 2001.

[41] S. C. Jacobson, R. Hergenroder, L. B. Koutny, and J. M. Ramsey. High-speed separations on a microchip. *Anal. Chem.*, 66(7):1114–1118, 1994.

[42] R. H. Carlson, C. V. Gabel, S. S. Chan, R. H. Austin, J. P. Brody, and J. W. Winkelman. Self-sorting of white blood cells in a lattice. *Physical Review Letters*, 79(11):2149–2152, 1997.

[43] R. Pethig. Delectrophoresis: Using inhormogeneous AC electrical fields to separate and manipulate cells. *Crit. Rev. in Biochem.*, 16(4):331–348, 1996.

[44] H. Morgan, N. G. Green, M. P. Hughes, W. Monaghan, and T. C. Tan. Large-area travelling-wave dielectrophoresis particle separator. *J. Micromech. Microeng.*, 7(2):65–70, 1997.

[45] J. P. Brody and P. Yager. Low reynolds number micro-fluidic devices. In *Proc. of Solid-State Sensor and Actuator Workshop*, pages 105–108. Hilton Head, June 1996.

[46] S. Fiedler, S. G. Shirley, T. Schnelle, and G. Fuhr. Dielectrophoretic sorting of particles and cells in a microsystem. *Anal. Chem.*, 70(9):1909–1915, 1998.

[47] Hou-Pu Chou. *Microfabricated Devices for Rapid DNA Diagnostics*. Ph.D. Thesis, California Institute of Technology, 2000.

[48] J. O'M. Bockris and A. K. N. Reddy. *Modern Electrochemistry: An Introduction to an Interdisciplinary Area*. Plenum Publishing Corporation, 1977.

[49] H. Katayama, Y. Ishihama, and N. Asakawa. Stable capillary coating with successive multiple ionic polymer layers. *Analytical Chemistry*, 70(11):2254–2260, 1998.

[50] N. H. Chiem and D. J. Harrison. Monoclonal antibody binding affinity determined by microchip-based capillary electrophoresis. *Electrophoresis*, 19:3040–3044, 1998.

[51] J. J. Li, J. F. Kelly, I. Chemushevich, D. J. Harrison, and P. Thibault. Separation and identification of peptides from gel-isolated membrane proteins using a microfabricated device for combined capillary electrophoresis/nanoelectrospray mass spectrometry. *Analytical Chemistry*, 72:599–609, 2000.

[52] C. S. Effenhauser, G. J. M. Bruin, and A. Paulus. Integrated capillary electrophoresis on flexible silicone microdevices: Analysis of DNA restriction fragments and detection of single DNA molecules on microchips. *Anal. Chem.*, 69(17):3451–3457, 1997.

[53] P. H. Li and D. J. Harrison. Transport, manipulation, and reaction of biological cells on-chip using electrokinetic effect. *Anal. Chem.*, 69(8):1564–1568, 1997.

[54] A. G. Hadd, D. E. Raymond, J. W. Halliwell, S. C. Jacobson, and J. M. Ramsey. Microchip device for performing enzyme assays. *Analytical Chemistry*, 69:3407–3412, 1997.

[55] A. G. Hadd, S. C. Jacobson, and J. M. Ramsey. Microfluidic assays of acetylcholinesterase inhibitors. *Analytical Chemistry*, 71:5206–5212, 1999.

[56] N. H. Chiem and D. J. Harrison. Microchip-based capillary electrophoresis for immunoassays: analysis of monoclonal antibodies and theophylline. *Electrophoresis*, 19:3040–3044, 1998.

[57] G.D. Meredith, C.E. Sims, J.S. Soughayer, and N.L. Allbritton. Measurement of kinase activation in single mammalian cells. *Nature Biotechnology*, 18(3):309–312, 2000.

[58] C. L. Lee, J. Linton, J. S. Soughayer, C. E. Sims, and N. L. Allbritton. Localized measurement of kinase activation in oocytes of *xenopus laevis*. *Nature Biotechnology*, 17(8):759–762, 1999.

[59] M. A. Unger, H. P. Chou, T. Thorsen, A. Scherer, and S. R. Quake. Microfabricated valves and pumps using multilayer soft lithography. *Science*, 288(5463):113–116, April 2000.

[60] H. P. Chou, M. A. Unger, A. Scherer, and S.R. Quake. Integrated elastomer fluidic lab-on-a-chip — surface patterning and DNA diagnostics. In *Proc. of Solid-State Sensor and Actuator Workshop*. Hilton Head, June 2000.

[61] H. P. Chou, M. A. Unger, and S.R. Quake. A microfabricated rotary pump. *Biomedical Microdevices*, 3(4):323–330, Nov 2001.

[62] S. R. Quake and A. Scherer. From micro- to nanofabrication with soft materials. *Science*, 290(5496):1536–1540, 2000.

[63] General Electric Technical Library. Product technology for silicone heat cured elastomers. URL:<http://www.gesilicones.com/silicones/americas/business/portfolio/h%ce/workshops/paperproducttech.shtml>, Copyright 2001.

[64] D. J. Campbell, K. J. Beckman, C. E. Calderson, P. W. Doolan, R. H. Moore, A. B. Ellis, and G. C. Lisensky. Replication and compression of bulk surface structures with polydimethylsiloxane elastomer. *Journal of Chemical Education*, 76:537, 1999.

[65] H. P. Chou, C. Spence, A. Scherer, and S. R. Quake. Microfabricated devices for sizing DNA and sorting cells. *Proc. SPIE*, 3258:181–187, January 1998.

[66] H. Joo, Z. L. Lin, and F.H. Arnold. Laboratory evolution of peroxide-mediated cytochrome p450 hydroxylation. *Nature*, 399(6737):670–673, 1999.

[67] L. L. Sohn, O. A. Saleh, G. R. Facer, A. J. Beavis, R. S. Allan, and D. A. Notterman. Capacitance cytometry: Measuring biological cells one by one. *Proceedings of the National Academy of Sciences of the United States of America*, 97(20):10687–10690, 2000.

[68] Huimin Zhao. *Enzyme Design by Directed Evolution*. Ph.D. Thesis, California Institute of Technology, 1998.

[69] R. C. Cadwell and G. F. Joyce. Randomization of genes by PCR mutagenesis. *PCR Methods Appl*, 2(1):28–33, 1992.

[70] W. P. C. Stemmer. Rapid evolution of a protein *in vitro* by DNA shuffling. *Nature*, 370(6488):389–391, 1994.

[71] A. Crameri, E. A. Whitehorn, E. Tate, and W. P. C. Stemmer. Improved green fluorescent protein by molecular evolution using DNA shuffling. *Nature Biotechnology*, 14(3):315–319, 1996.

[72] H. M. Zhao, L. Giver, Z. X. Shao, J. A. Affholter, and F. H. Arnold. Molecular evolution by staggered extension process (step) in vitro recombination. *Nature Biotechnology*, 16(3):258–261, 1998.

[73] R. Y. Tsien. The green fluorescent protein. *Annual Review of Biochemistry*, 67:509–544, 1998.

[74] M. Zaccolo, F. De Giorgi, C. Y. Cho, L. X. Feng, T. Knapp, P. A. Negulescu, S. S. Taylor, R. Y. Tsien, and T. Pozzan. A genetically encoded, fluorescent indicator for cyclic AMP in living cells. *Nature Cell Biology*, 2(1):25–29, 2000.

[75] F. K. M. Chan, R. M. Siegel, D. Zacharias, R. Swofford, K. L. Holmes, R. Y. Tsien, and M. J. Lenardo. Fluorescence resonance energy transfer analysis of cell surface receptor interactions and signaling using spectral variants of the green fluorescent protein. *Cytometry*, 44(4):361–368, 2001.

[76] R. Hein and R. Y. Tsien. Engineering green fluorescent protein for improved brightness, longer wavelengths and fluorescence resonance energy transfer. *Current Biology*, 6(2):178–182, 1996.

[77] M. Ormo, A. B. Cubitt, K. Kallio, L. A. Gross, R. Y. Tsien, and S. J. Remington. Crystal structure of the *aequorea* victoria green fluorescent protein. *Science*, 273(5280):1392–1395, 1996.

[78] R. M. Wachter, B. A. King, R. Heim, K. Kallio, R. Y. Tsien, S. G. Boxer, and S. J. Remington. Crystal structure and photodynamic behavior of the blue emission variant Y66H/Y145F of green fluorescent protein. *Biochemistry*, 36(32):9759–9765, 1997.

[79] M. V. Matz, A. F. Fradkov, Y. A. Labas, A. P. Savitsky, A. G. Zaraisky, M. L. Markelov, and S. A. Lukyanov. Fluorescent proteins from nonbioluminescent *anthozoa* species. *Nature Biotechnology*, 17(10):969–973, 1999.

[80] G. S. Baird, D. A. Zacharias, and R. Y. Tsien. Biochemistry, mutagenesis, and oligomerization of DsRed, a red fluorescent protein from coral. *Proceeding of the National Academy of Sciences of the United States of America*, 97(22):11984–11989, 2000.

[81] L. A. Gross, G. S. Baird, R. C. Hoffman, K. K. Baldridge, and R. Y. Tsien. The structure of the chromophore within DsRed, a red fluorescent protein from coral. *Proceeding of the National Academy of Sciences of the United States of America*, 97(22):11990–11995, 2000.

[82] H. M. Zhao and F. H. Arnold. Functional and nonfunctional mutations distinguished by random recombination of homologous genes. *Proceeding of the National Academy of Sciences of the United States of America*, 94(15):7997–8000, 1997.

[83] H. M. Zhao and F. H. Arnold. Optimization of DNA shuffling for high fidelity recombination. *Nucleic Acids Research*, 25(6):1307–1308, 1997.

[84] P. S. Daugherty, B. L. Iverson, and G. Georgiou. Flow cytometric screening of cell-based libraries. *Journal of Immunological Methods*, 243:211–227, 2000.

[85] H. M. Zhao and F. H. Arnold. Combinatorial protein design: Strategies for screening protein libraries. *Current Opinion in Structural Biology*, 7(4):480–485, 1997.

[86] H. H. McAdams and L. Shapiro. Circuit simulation of genetic networks. *Science*, 269(5224):650–656, 1995.

[87] M. B. Elowitz and S. Leibler. A synthetic oscillatory network of transcriptional regulators. *Nature*, 403(6767):335–338, 2000.

[88] T. S. Gardner, C. R. Cantor, and J. J. Collins. Construction of a genetic toggle switch in *escherichia coli*. *Nature*, 403(6767):339–342, 2000.

[89] A. Becskei and L. Serrano. Engineering stability in gene networks by autoregulation. *Nature*, 405(6786):590–593, 2000.

[90] T. F. Knight and G. J. Sussman. Cellular gate technology. *Unconventional Models of Computation*, pages 257–272, 1997.

[91] Srinivas Devadas. The digital abstraction. URL:<`http://www.caa.lcs.mit.edu/~devadas/6.004/Lectures/lect1/sld016.ht%m`>, March 2002.

[92] R. Blakemore. Magnetotactic bacteria. *Science*, 190(4212):377–379, 1975.

[93] R. B. Frankel, R. Blakemore, F. F. Torres De Araujo, D. M. S. Esquivel, and J. Danon. Magnetotactic bacteria. *Science*, 190(4212):377–379, 1975.

[94] J. L. Kirschvink, S. Padmanabha, C. K. Boyce, and J. Oglesby. Measurement of the threshold sensitivity of honeybees to weak, extremely low-frequency magnetic fields. *Journal of Experimental Biology*, 200(9):1363–1368, 1997.

[95] C. V. Haugh and M. M. Walker. Magnetic discrimination learning in rainbow trout (*Oncorhynchus mykiss). Journal of Navigation*, 51(1):35–45, 1998.

[96] C. E. Diebel, R. Proksch, C. R. Green, P. Neilson, and M. M. Walker. Magnetite defines a vertebrate magnetoreceptor. *Nature*, 406(6793):299–302, 2000.

[97] M. M. Walker, C. E. Diebel, C. V. Haugh, P. M. Pankhurst, J. C. Montgomery, and C. R. Green. Structure and function of the vertebrate magnetic sense. *Nature*, 390(6658):371–376, 1997.

[98] M. M. Walker. Magnetic position determination by homing pigeons. *Journal of Theoretical Biology*, 197(2):271–276, 1999.

[99] J. L. Kirschvink, A. Kobayshi-Kirschvink, and B. J. Woodford. Magnetite biomineralization in the human brain. *Proceedings of the National Academy of Sciences of the United States of America*, 89(16):7683–7687, 1992.

[100] M. M. Walker, C. E. Diebel, and C. R. Green. Structure, function, and use of the magnetic sense in animals (invited). *Journal of Applied Physics*, 87(9):4653–4658, 2000.

[101] D. Schuler and R. B. Frankel. Bacterial magnetosomes: microbiology, biomineralization and biotechnological applications. *Applied Microbiology and Biotechnology*, 52(4):464–473, 1999.

[102] Y. Haik, V. Pai, and C. J. Chen. Development of magnetic device for cell separation. *Journal of Magnetism and Magnetic Materials*, 194(1-3):254–261, 1999.

[103] J. J. Chalmers, M. Zborowski, L. P. Sun, and L. Moore. Flow through, immunomagnetic cell separation. *Biotechnology Progress*, 14(1):141–148, 1998.

[104] L. P. Sun, M. Zborowski, L. R. Moore, and J. J. Chalmers. Continuous, flow-through immunomagnetic cell sorting in a quadrupole field. *Cytometry*, 33(4):469–475, 1998.

[105] P. S. Williams, M. Zborowski, and J. J. Chalmers. Flow rate optimization for the quadrupole magnetic cell sorter. *Analytical Chemistry*, 71(17):3799–3807, 1999.

[106] I. Safarik and M. Safarikova. Use of magnetic techniques for the isolation of cells. *Journal of Chromatography B*, 722(1-2):33–53, 1999.

[107] F. Baudenbacher, N. T. Peters, and J. P. Wikswo. High resolution low-temperature superconductivity superconducting quantum interference device microscope for imaging magnetic fields of samples at room temperatures. *Review of Scientific Instruments*, 73(3):1247–1254, 2002.

[108] T. S. Lee, E. Dantsker, and J. Clarke. High-transition temperature superconducting quantum interference device microscope. *Review of Scientific Instruments*, 67(12):4208–4215, 1996.

[109] T. S. Lee, Y. R. Chemla, E. Dantsker, and J. Clarke. High-T-c SQUID microscope for room temperature samples. *IEEE Transactions on Applied Superconductivity*, 7(2):3147–3150, 1997.

[110] Y. R. Chemla, H. L. Grossman, T. S. Lee, J. Clarke, M. Adamkiewicz, and B. B. Buchanan. A new study of bacterial motion: Superconducting quantum interference device microscopy of magnetotactic bacteria. *Biophysical Journal*, 76(6):3323–3330, 1999.

[111] T. Matsunaga, T. Sakaguchi, and F. Tadokoro. Magnetite formation by a magnetic bacterium capable of growing aerobically. *Applied Microbiology and Biotechnology*, 35(5):651–655, 1991.

[112] E. A. Wolin, M. J. Wolin, and R. S. Wolfe. Formation of methane by bacterial extracts. *Journal of Biological Chemistry*, 238(8):2882–2885, 1963.